KU LEUVEN

ARENBERG DOCTORAL SCHOOL
Faculty of Science

Deposition, diffusion and convection: BLUES approximants and some exact results

Jonas Berx

Supervisor:
Prof. dr. Joseph O. Indekeu

Dissertation presented in partial fulfillment of the requirements for the degree of Doctor of Science (PhD): Physics

August 2, 2021

Deposition, diffusion and convection: BLUES approximants and some exact results

Jonas BERX

Examination committee:
Prof. dr. Koen Van Den Abeele, chair
Prof. dr. Joseph O. Indekeu, supervisor
Prof. dr. Wojciech De Roeck
Prof. dr. Johan Quaegebeur
Prof. dr. Jens Eggers
(University of Bristol, UK)
Prof. dr. Mehran Kardar
(Massachusetts Institute of Technology, USA)
Prof. dr. Wim Magnus
(UAntwerpen and imec)
Prof. dr. Laurence Rongy
(Université Libre de Bruxelles)

Dissertation presented in partial fulfillment of the requirements for the degree of Doctor of Science (PhD): Physics

August 2, 2021

Uitgegeven in eigen beheer, Jonas Berx, Celestijnenlaan 200D box 2415, B-3001 Leuven (Belgium)

Acknowledgements

Doing a Ph.D. is not a road one walks alone. Along the way I have had help from so many people, in big ways and in small ways. So, in order of importance, I would like to thank the following people.

First and foremost is my promotor, Joseph Indekeu. There are no words that can fully describe the extent of my gratitude, so I will just say: thank you. Thank you for guiding me from being a mediocre student to a (somewhat) decent researcher and pushing me out of my comfort zone. Thank you for taking me with you on your travels around the world and introducing me to new people. Thank you for just being my supervisor and above all my friend.

Second in the list are my colleagues from the ITF and the department. It is only when you sit in an empty (home) office that you truly appreciate the value of having nice colleagues. I would like to thank in particular Florian, Rob and Vincent, who started their Ph.D. together with me and with whom I could laugh, argue or talk about practically anything.

Third, I would like to thank my parents, my girlfriend Annelien and my friends. My parents for raising me with a scientific mindset (kudos to you especially, dad); my girlfriend for trying to remember what my research is about, and my friends for convincing me not to take everything so seriously.

Finally, I would like to thank Carlo Vanderzande, who sadly passed away on 02/09/2019. He supervised my master's thesis and introduced me to Joseph, who was looking for a new Ph.D. student at the time. This adventure would not even have begun without you, Carlo. Thank you.

Abstract

An analytic procedure for solving nonlinear differential equations, the BLUES function method, is studied. It is first implemented for differential equations that can be reduced to ordinary differential equations (ODEs) with one independent variable. When an inhomogeneous source (or sink) is present in the equation, the BLUES function method provides a natural way to obtain approximate solutions. In this setup, different systems from nonlinear physics and other sciences are investigated, particularly in the context of nonlinear travelling waves within fluid dynamics and biophysics. The BLUES method is applied to a fractional ordinary differential equation (FDE) in the context of heat flow within a semi-infinite rod. An initial comparison with another iterative method is carried out, showing that the BLUES method possesses a larger region of convergence.

Next, the method is extended to the realms of partial differential equations (PDEs) and systems of coupled nonlinear differential equations (CDEs). In both of these areas, the method is reformulated slightly to accommodate the particulars of that area, and is consequently studied first by means of simple examples and finally by means of a model for interface growth under the influence of shear flow. Within the field of (coupled) PDEs, the role of the external source is now fulfilled by the initial condition through multiplication with a point source at $t = 0$. A comprehensive comparison with preexisting methods is performed and it is shown that in many cases the BLUES function method is an ideal candidate when choosing between iterative methods. When studying systems of coupled ordinary differential equations, the linear operator can often be sensibly chosen in such a way that it includes the fixed points of the nonlinear system, greatly increasing the BLUES function method's region and speed of convergence.

Lastly, the hierarchical random deposition model (HRDM) is studied. This deposition process takes place in a viscous medium so that the particles hit the surface in order of size. The size follows a hyperbolic distribution, allowing the

larger particles to hit the substrate first. Additionally, square "holes" following the same distribution can be excavated. In particular, the connection between the (non)-proliferation of coastal points (level sets) and lateral percolation is investigated by analytical means and numerical simulations. It is found that exactly at the percolation threshold P_c, the number of coastal points (or coastlines in two dimensions) exhibits logarithmic fractal behaviour, increasing linearly with increasing generation. Next, the dynamics of the deposition are adjusted to allow particles to stick sideways to preexisting material, transforming the hierarchical *random* deposition model into a hierarchical *ballistic* deposition model (HBDM). The latter is clearly still a random model but the sideways growth introduces lateral correlations between different columns. The surface length increment, the fraction of closed-off voids and the associated porosity are studied by means of numerical simulations and analytical approximations. Numerical results concerning percolation and roughness exponents in the HBDM are given and briefly discussed in the associated appendix.

Samenvatting

Een analytische methode om niet-lineaire differentiaalvergelijkingen op te lossen wordt bestudeerd. De nieuwe methode wordt de BLUES functie methode genoemd. Deze wordt eerst geïmplementeerd voor gewone differentiaalvergelijkingen (ODEs) waarbij er maar één onafhankelijke variabele aanwezig is. Wanneer een inhomogene bron voorkomt in deze differentiaalvergelijking vormt de BLUES functie methode een natuurlijke keuze om benaderende oplossingen te bekomen. Binnen deze context worden verschillende systemen uit niet-lineaire fysica en andere wetenschappen bestudeerd, met name het fenomeen van lopende golven binnen vloeistofdynamica en biofysica. De BLUES methode wordt nadien ook toegepast op een fractionele differentiaalvergelijking (FDE) die warmtegeleiding binnen een halfoneindige staaf beschrijft. Een initiële onderlinge vergelijking met een andere iteratieve methode wordt uitgevoerd, waaruit blijkt dat de BLUES methode een grotere convergentiestraal bezit.

Vervolgens wordt de methode uitgebreid naar partiële differentiaalvergelijkingen (PDEs) en gekoppelde differentiaalvergelijkingen (CDEs). Binnen het kader van deze uitbreidingen wordt de BLUES methode telkens licht aangepast om specifieke kenmerken in de methode op te nemen. Zo zal binnen het domein van de (gekoppelde) PDEs de beginvoorwaarde de rol van de externe bron of put overnemen en zal er bij gekoppelde vergelijkingen de mogelijkheid bestaan om de lineaire operator oordeelkundig te bepalen zodat de dekpunten reeds in het lineaire systeem aanwezig zijn. Dit bevordert zowel de convergentiesnelheid als de regio. Een uitgebreide vergelijking met andere methodes wordt uitgevoerd. Hieruit komt naar voren dat de BLUES functie methode een uitstekende kandidaat is wanneer men moet kiezen tussen verschillende iteratieve methodes.

Tot slot wordt het hiërarchisch random depositiemodel (HRDM) bestudeerd. In dit model vindt de depositie plaats in een viskeus medium zodat de deeltjes het oppervlak raken in volgorde van grootte. Deze grootte volgt een hyperbolische verdeling waarbij dat de grootste deeltjes eerst op het substraat landen. Bovendien kunnen ook vierkante “gaten” gegraven worden

die dezelfde verdeling volgen. De connectie tussen de toe- of afname van kustpunten (of niveaukrommen) en laterale percolatie wordt onderzocht door middel van analytische berekeningen en numerieke simulaties. Hieruit kan worden vastgesteld dat exact op de percolatie grenswaarde P_c, het aantal kustpunten (of kustlijnen in twee dimensies) logaritmisch fractaal gedrag vertoont en bijgevolg lineair toeneemt met toenemende generatie. Vervolgens worden de spelregels van het *random* depositieproces aangepast om toe te laten dat deeltjes zich zijdelings kunnen vasthechten aan het bestaande materiaal, wat resulteert in een zogenaamd hiërarchich *ballistisch* depositieproces (HBDM). Deze dynamica induceert sterke laterale correlaties tussen verschillende kolommen. De lengtetoename van het oppervlak gevormd door dit ballistisch depositieproces, het aantal afgesloten reservoirs en bijgevolg ook de porositeit van het materiaal worden numeriek bepaald en ondersteund met benaderende analytische uitdrukkingen. Aanvullende numerieke resultaten voor percolatie en de ruwheidsexponent van het oppervlak worden gebundeld in de bijbehorende appendix.

List of Abbreviations

ADM	Adomian Decomposition Method
BLUES	Beyond Linear Use of Equation Superposition
DE	Differential Equation
CDE	Coupled Differential Equations
FDE	Fractional Differential Equation
ODE	Ordinary Differential Equation
PDE	Partial Differential Equation
SDE	Stochastic Differential Equation
HAM	Homotopy Analysis Method
HBDM	Hierarchical Ballistic Deposition Model
HPM	Homotopy Perturbation Method
HRDM	Hierarchical Random Deposition Model
MOL	Method Of Lines
PT	Perturbation Theory
VIM	Variational Iteration Method
GVIM	Variational Iteration Method with Green function

Contents

Chapter 1

Introduction and overview

1.1 Differential equations

The history of differential equations (DEs) is still somewhat of a murky topic, originating in the scientific "war" between on one hand Isaac Newton and on the other hand Gottfried Leibniz. All we can say with certainty is that in the last three decades of the 17th century, the study of differential equations arose as a distinct field within mathematics. Nowadays these equations arise in almost every subject one can imagine: from wireless communication to the modelling of animal migration or chemical reactions.

Differential equations are equations wherein the derivatives of the unknown function occur, possibly with the argument of the function itself and any external influences, which we call *sources* or *sinks*. When, in every term of the differential equation, the sum of the powers of the unknown function and/or its derivatives is 0 or 1, the equation is called a *linear* DE. The example almost everyone is familiar with is Newton's second law

$$F(t) = m\frac{\mathrm{d}^2x(t)}{\mathrm{d}t^2}\,, \tag{1.1}$$

where m is the mass of an object, F is the force, $x(t)$ is the time-dependent position and t is the time. When the force F depends linearly on time, space or velocity, the solution of equation (1.1) can easily be found by direct integration, substitution or a whole plethora of methods that are known to every undergraduate science student. However, when the force is a nonlinear function of $x(t)$ (e.g. Duffing oscillator), these methods often fail.

In general, one can not expect one analytical method to exist that can solve every differential equation imaginable. Even for relatively simple cases such as Abel's equation of the first kind, $u'(t) = u^3(t) + t$, where derivatives with respect to t are indicated with a prime, no solution in terms of elementary functions (exponentials, polynomials, trigonometric functions,etc.) is possible, nor in terms of special functions (Bessel, Airy, Kummer, etc.) [1].

A way of trying to find some semblance of a "solution" is by using power series. One can then spend tedious hours of spitting out terms in the series (or by forcing a computer to do it), only to achieve results that are often unsatisfactory. More often, nonlinear differential equations are analysed by making use of solution techniques such as the inverse scattering transform that rely on symmetry arguments, or by trying to find a coordinate transform that maps the problem onto a related problem that is easier to solve.

Luckily, numerical methods may provide some relief. The sheer amount of the methods that are available is almost overwhelming and one can be reasonably sure to find a numerical package that gets the job done. However, all of these methods have their limitations and underlying assumptions. It is only through careful theoretical analysis of the equations under consideration that one can know whether the results received from numerical solvers are actually useful. The best-known methods such as Euler's method or the Runge–Kutta methods are bound to be found in every introductory textbook on numerical analysis so we will defer to those when needed. A brief discussion on the methods used in this thesis is given in section 2.6.

1.2 Deposition models

The study of surface growth and deposition is one of the paradigms in statistical physics. By understanding the processes underlying growth phenomena, one can control the precise physical properties of materials that are used in e.g. nanotechnology, biophysics or medicine. The models that generate such surfaces generally possess a simple set of "rules" describing the process. Nevertheless, the morphology of the interfaces can quickly become nontrivial by adding more and more realistic assumptions. Generally, deposition models and interfaces are described with a set of quantities such as scaling exponents, fractal dimensions, porosity or surface length increments.

In practice, we differentiate between *discrete* and *continuous* models for surface growth. In the discrete case, a (finite) set of sites can be identified for particles to be deposited at. This deposition happens at discrete time intervals. The most well-known discrete deposition models are the random deposition model and the

ballistic deposition model. The former possesses an exact solution and assumes that each particle column grows independently of the others and no surface relaxation, i.e., diffusion to other sites, is possible. If relaxation is included, a deposited particle migrates to a neighbouring site with lower height. This variation does not possess an analytical solution but it is possible to find the scaling exponents by studying the symmetries of the associated linear stochastic Edwards-Wilkinson equation [2],

$$h_t(\boldsymbol{x},t) = D\nabla^2 h(\boldsymbol{x},t) + \eta(\boldsymbol{x},t)\,, \tag{1.2}$$

where $h(\boldsymbol{x},t)$ is the height of the resulting surface at a position $\boldsymbol{x}$ and time t, with Gaussian white noise $\eta(\boldsymbol{x},t)$, which is invariant under self-affine scaling. The constant D is the surface tension. The usual scaling exponents α and z are found by considering the surface width

$$W^2(t,L) = aL^{2\alpha}G\left(\frac{t}{bL^z}\right) \tag{1.3}$$

where a, b are constants that vary with the system under consideration. The exponent z characterises the scaling of the roughness in time while α describes the spatial scaling of the roughness for $t \to \infty$. The roughening exponent β can be found by considering the scaling $G(x) \sim x^{2\beta}$ for $x \to 0$. Also, $G(x) \to \textit{constant}$ for $x \gg 1$. For the Edwards-Wilkinson equation in $d = 1$, the exponents are $\alpha = 1/2$, $\beta = 1/4$ and $z = 2$, with the following relations: $\alpha = \beta z$ and $z - 2\alpha = 1$.

Note that the random deposition model is not able to create porous structures as a result of the independent growth of columns and the diffusion to lower sites. A nontrivial extension that does allow pores to form is the ballistic deposition model, whereby particles can attach laterally to the side of a neighbouring column. Allowing for this kind of dynamics, the surface can grow tangentially as well as vertically. Due to overhangs being created, the ballistic deposition model possesses a nonlocal character, obstructing lower sites from receiving any new particle flux. The stochastic differential equation that corresponds to this process is the Kardar-Parisi-Zhang equation [3]

$$h_t(\boldsymbol{x},t) = D\nabla^2 h(\boldsymbol{x},t) + \frac{\lambda}{2}\left(\nabla h(\boldsymbol{x},t)\right)^2 + \eta(\boldsymbol{x},t)\,, \tag{1.4}$$

where the gradient-squared term indicates slope-dependent growth. In one dimension, the scaling exponents can be determined by a renormalisation procedure, yielding the exact values $\alpha = 1/2$, $\beta = 1/3$ and $z = 3/2$, with $\alpha + z = 2$. One classical assumption in these models is that all of the deposited particles are of the same size, being deposited *sequentially* (one-by-one) on a substrate. Relatively little research has investigated *synchronous* deposition

where multiple particles are deposited simultaneously, or particles of different sizes that may exhibit scaling themselves. The former models reduce to the sequential processes in the "dilute" limit [4] in which the deposition probability $P \to 0$. In this thesis we will study both effects first in a random deposition setting and later in a ballistic deposition model.

Continuous models move away from the assumptions of discrete time and space, instead allowing for deposition on a real space whereby the deposition time is usually extracted from an exponential distribution. We will not discuss these models any further.

With the advent of experimental techniques such as vapor deposition [5] or electron beam evaporation [6], thin-film surfaces (often metallic in nature) can be created in a laboratory, permitting a fine measure of control. This provides an invaluable source of data that can be used for comparison with both analytical results and numerical simulation.

1.3 Structure of the thesis

The setup of this thesis is as follows. In chapter 2, a birds-eye view is given of the most widely used methods to solve nonlinear differential equations, their advantages and disadvantages are discussed, and the BLUES function method is situated in this framework. A brief comment on other iterative procedures is given.

Each of the chapters 3, 4, 5, 6 and 7 can be read as standalone works (with the possible exception of chapter 4), since they are based on (published) articles and are therefore mostly self-contained.

In chapter 3, the original formulation of the BLUES function method is applied to four ODEs that are derived from partial differential equations (PDEs) with external comoving sources by making a travelling-wave Ansatz, and the feasibility to calculate higher-order approximants for the soliton or travelling-wave solution is investigated. Chapter 4 treats a fractional differential equation (FDE) in one coordinate, effectively connecting this chapter to the previous chapter 3. In this chapter, a first comparison is made between the BLUES function method and the Adomian decomposition method (ADM).

The next step is to move away from the realm of ODEs and study PDEs, which is done in chapter 5 for PDEs with a first-order time derivative. The BLUES function method is modified slightly to accommodate the inclusion of initial conditions and the newly minted formulation is once again tested out on three simple PDEs. For each of these equations the exact solution is known. The

method is then compared to an arsenal of other methods: the ADM, VIM, GVIM and HPM. Knowing the exact solution, the performance of the BLUES function method can be weighed against the other methods. While these basic examples are instructive, they are rather simplistic and are only suited for testing. Hence, I consequently study a heuristic model for interface evolution under the combined influence of deposition and lateral shear for Gaussian and spatially periodic initial conditions.

In chapter 6, the different parts of the BLUES function method come together to study systems of coupled differential equations. First, the SIRS compartmental model for the propagation of infectious diseases is studied by combining the BLUES function method with a matrix formalism. Subsequently, this new formulation of the method is combined with the previously developed extension to PDEs with initial conditions to study a second-order-derivative-in-time nonlinear telegrapher's equation.

Chapter 7 first treats some aspects of random hierarchical deposition, in particular the connection between coastal point (non-)proliferation and percolation, and briefly discusses surface roughness properties. Next, a nontrivial extension is studied where deposited matter can "stick" to the substrate sideways, creating protrusions and introducing lateral correlations between different columns. For the latter model, the surface length increment and the porosity are studied analytically and by means of numerical simulations.

The appendices A, B and C elucidate some of the result of the thesis. This is either done in the form of extra or in-depth calculations of results mentioned in the text of the regular chapters, or in the form of numerical results that are yet unsupported by analytical calculations.

Chapter 2

Iterative methods for differential equations

In this precursory chapter I will first develop the BLUES function method for nonlinear ordinary differential equations and subsequently introduce the other methods that are used for comparison in the other chapters. In the last part of this chapter, I briefly discuss other iterative procedures that can be implemented into most of the methods, including the BLUES function method.

2.1 Beyond Linear Use of Equation Superposition

The theory of BLUES functions and the associated iteration sequence have been developed in [7] for ODEs. Hence, we will recall some of the main results here and develop the method further into a practical tool. Let us start from the original formulation of the method with a nonlinear ODE that can be written as an operator $\mathcal{N}_z$ and assume a piecewise analytic function $B(z)$ which solves

$$\mathcal{N}_z B(z) = \delta(z) \tag{2.1}$$

with suitable boundary conditions. The Dirac delta source is added to compensate a possible discontinuity of the derivative of order $(n-1)$ at $z=0$ in the case of an n-th order DE. The (bio-)physical relevance of adding a source or sink has been discussed in [8] in the context of reaction-diffusion-convection equations and can e.g. indicate the injection of a nutrient or poison, respectively for a source or sink. The form of equation (2.1) is reminiscent of the Green

function approach used for linear DEs, and we assume we can construct an associated linear operator $\mathcal{L}_z$ in such a way that $B(z)$ also solves

$$\mathcal{L}_z B(z) = \delta(z), \tag{2.2}$$

with the same boundary conditions, which makes $B(z)$ a Green function for the linear operator $\mathcal{L}_z$. We can now consider the nonlinear DE with an arbitrary source $\psi(z)$ and ask whether the solution to this DE can be found using the convolution product $B * \psi$, knowing that this product is a solution of the linear DE with the same source $\psi(z)$. A function $B(z)$ which solves both (2.1) and (2.2) was called a BLUES (Beyond Linear Use of Equation Superposition) function in [7] because we are using the convolution with the source beyond the domain of the linear DE. The construction of the general solution $U(z)$ to the nonlinear DE with a source $\psi(z)$

$$\mathcal{N}_z U(z) = \psi(z) \tag{2.3}$$

starts by defining a residual operator $\mathcal{R}_z \equiv \mathcal{L}_z - \mathcal{N}_z$ and by calculating the solution to the nonlinear problem in the form $U(z) = (B * \phi)(z)$, i.e.,

$$\mathcal{N}_z(B * \phi)(z) = \psi(z), \tag{2.4}$$

which is also in the form of a convolution product $B * \phi$, where the associated source $\phi(z)$ can be calculated by considering the action of the residual operator on $(B * \phi)(z)$, i.e.,

$$\begin{aligned} \mathcal{R}_z(B * \phi)(z) &= \mathcal{L}_z(B * \phi)(z) - \mathcal{N}_z(B * \phi)(z) \\ &= \phi(z) - \psi(z)\,. \end{aligned} \tag{2.5}$$

Rearranging this equation, we can find an implicit equation for $\phi(z)$,

$$\phi(z) = \psi(z) + \mathcal{R}_z(B * \phi)(z). \tag{2.6}$$

To obtain the solution to the nonlinear DE (2.3), equation (2.6) can be iterated in order to calculate an approximation in the form of a sequence in powers of the residual $\mathcal{R}_z$. This was expected to be especially useful when the source $\psi(z)$ is sharply localized. Because $\mathcal{R}_z B(z) = 0$, one can expand meaningfully in powers of $\mathcal{R}_z$ when the source does not differ much from the delta source. The small parameter in this expansion is the width of the source $\psi(z)$ divided by the characteristic length of $B(z)$. However, our investigation has shown that the method may also work well when the source is not sharp and when there is no small parameter. Our study has also revealed that it is not necessary for $B(z)$ to be a solution of (2.1). The property (2.2) is sufficient.

To zeroth order, the sources $\phi^{(0)}(z)$ and $\psi(z)$ are identical and the approximation is the convolution product

$$U_{\psi}^{(0)}(z) = (B * \phi^{(0)})(z) = (B * \psi)(z). \tag{2.7}$$

To nth order ($n \geq 1$), the approximate solution can be found [9] by iterating (2.6) and taking the convolution product with $B(z)$, i.e.,

$$\begin{aligned} U_{\psi}^{(n)}(z) = (B * \phi^{(n)})(z) &= (B * \psi)(z) + \left(B * \mathcal{R}_z U_{\psi}^{(n-1)}\right)(z) \\ &= U_{\psi}^{(0)}(z) + \left(B * \mathcal{R}_z U_{\psi}^{(n-1)}\right)(z). \end{aligned} \tag{2.8}$$

Testing the usefulness of the iteration sequence (6.53) for different nonlinear systems and providing more detail of the method and its applications are the main goals of this thesis.

The BLUES function method can be naturally extended to FDEs, PDEs or to systems of coupled DEs. This often entails some minor but important modifications of the procedure outlined above. These variations on the BLUES function method will be elaborated upon in the corresponding chapters 4, 5 and 6, for FDEs, PDEs and systems of DEs, respectively.

Before studying the method in all of the aforementioned areas, we briefly elucidate other related methods that will often be used to gauge the accuracy of the BLUES function method.

2.2 Adomian decomposition method

The Adomian decomposition method (ADM) [10, 11] was first introduced by G. Adomian at the end of the previous century and was originally developed for nonlinear stochastic operator equations [12]. It was later modified to solve different kinds of ODEs, PDEs and systems of coupled equations. The method assumes that the solution u to a given differential equation can be written as the series

$$u = \sum_{n=0}^{\infty} u_n \,, \tag{2.9}$$

where now the component functions u_n, $n \in \mathbb{N}$ need to be determined. Consider a general differential equation

$$Lu + Ru + Nu = f \,, \tag{2.10}$$

where L is the highest-order derivative, R is the remaining linear operator, N is a nonlinear operator and f is an inhomogeneous source. When the DE (2.10) is a PDE, the linear operator L is often chosen to be the highest-order time derivative, instead of a higher-order spatial derivative. The method permits a certain measure of flexibility in choosing the linear operator. The only requirement is that it is easily invertible, i.e., L^{-1} should exist. As this linear operator is generally a derivative, the inverse operator will be a (multiple) integral.

Now apply the inverted linear operator L^{-1} to both sides of the equation (2.10) and rearrange. The solution u is now given by

$$u = g - L^{-1}(Ru) - L^{-1}(Nu)\,, \tag{2.11}$$

with the function g being the integrated source f and any extra terms originating from either initial or boundary conditions. The $L^{-1}(Ru)$ term should in principle present no problems as it is linear. The $L^{-1}(Nu)$ term, however, does present a problem. The ADM now proposes to decompose the nonlinear term as an infinite series of the so-called Adomian polynomials A_n, i.e.,

$$Nu = \sum_{n=0}^{\infty} A_n\,. \tag{2.12}$$

Inserting equations (2.9) and (2.12) into equation (2.11), i.e.,

$$\sum_{n=0}^{\infty} u_n = g - L^{-1}\left(R\sum_{n=0}^{\infty} u_n\right) - L^{-1}\left(\sum_{n=0}^{\infty} A_n\right) \tag{2.13}$$

admits the following decomposition of the solution into the component functions u_n,

$$\begin{aligned} u_0 &= g \\ u_1 &= -L^{-1}\left(Ru_0 + A_0\right) \\ u_2 &= -L^{-1}\left(Ru_1 + A_1\right) \\ &\vdots \\ u_n &= -L^{-1}\left(Ru_{n-1} + A_{n-1}\right)\,. \end{aligned} \tag{2.14}$$

The final piece of the puzzle is the calculation of the Adomian polynomials A_n. The series (2.12) is a Taylor series of the nonlinear function Nu about u_0, i.e.,

$$Nu = Nu_0 + \frac{\mathrm{d}N}{\mathrm{d}u}(u-u_0) + \frac{1}{2!}\frac{\mathrm{d}^2N}{\mathrm{d}u^2}(u-u_0)^2 + \ldots \tag{2.15}$$

Rearranging this equation by noticing that $u - u_0 = u_1 + u_2 + u_3 + \dots$ results in

$$Nu = Nu_0 + \frac{\mathrm{d}N}{\mathrm{d}u}(u_1 + u_2 + \dots) + \frac{1}{2!}\frac{\mathrm{d}^2N}{\mathrm{d}u^2}(u_1 + u_2 + \dots)^2 + \dots \tag{2.16}$$

By equating (2.16) and (2.12), the expressions for the Adomian polynomials can be calculated recursively [13]

$$\begin{aligned} A_0 &= Nu_0 \\ A_1 &= u_1\frac{\mathrm{d}N}{\mathrm{d}u}(u_0) \\ A_2 &= u_2\frac{\mathrm{d}N}{\mathrm{d}u}(u_0) + \frac{1}{2!}u_1^2\frac{\mathrm{d}^2N}{\mathrm{d}u^2}(u_0) \\ &\vdots \\ A_n &= \frac{1}{n!}\frac{\mathrm{d}^n}{\mathrm{d}\lambda^n}\left[N\left(\sum_{i=0}^{n} u_i\lambda^i\right)\right]\Bigg|_{\lambda=0}. \end{aligned} \tag{2.17}$$

Note that the compact expression for A_n is nothing more than Faà di Bruno's formula [14] for the chain rule for higher-order derivatives, applied to the functional composition of N and $\sum_{i=0}^{n} u_i\lambda^i$.

Now that all the pieces of the puzzle are in place, the solution to equation (2.10) can be found by iteratively solving (2.14) and substituting the component functions into the general solution (2.9).

However, one must take into account both the advantages and disadvantages of the ADM [15]. While the recurrence is easy to set up and implement numerically, the drawback is that in general the method is only useful for small values of the independent variables. Furthermore, the convergence is slow because of the exponentially increasing difficulty to calculate new Adomian polynomials. There have been countless modifications [16, 12, 17] of the method to (partially) solve the problem of either the slow convergence speed or the small region of convergence.

2.3 Variational iteration method

While the ADM assumed the solution to be of the form of an infinite series of component functions, the variational iteration method (VIM) calculates the

solution as a sequence of approximants. It was developed by Ji-Huan He [18, 19] and is one of the most widely used approximation methods for analytically solving (nonlinear) differential equations.

Consider the general nonlinear differential equation (2.10) introduced in the previous section 2.2,

$$Lu + Nu = f\,, \tag{2.18}$$

where we have combined Lu and Ru into one linear operator, which we will again call Lu. No confusion should arise from this substitution, as the meaning of Lu will be clear from the context. The VIM introduces the following *ad hoc* correction functional

$$u_{n+1}(t) = u_n(t) + \int_{t_0}^{t} \mathrm{d}s\, \lambda(s,t)\left(Lu_n(s) + N\tilde{u}_n(s) - f(s)\right)\,, \tag{2.19}$$

where $\lambda(s,t)$ is a Lagrange multiplier and $\tilde{u}_n$ is a restricted variation, which means that $\delta\tilde{u}_n = 0$. Also, assume that $\delta f = 0$. The Lagrange multiplier can be calculated by considering the following variation

$$\begin{aligned}\delta u_{n+1}(t) &= \delta u_n(t) + \delta \int_{t_0}^{t} \mathrm{d}s\, \lambda(s,t)\left(Lu_n(s) + N\tilde{u}_n(s) - f(s)\right)\\ &= \delta u_n(t) + \delta \int_{t_0}^{t} \mathrm{d}s\, \lambda(s,t)\left(Lu_n(s)\right)\end{aligned} \tag{2.20}$$

Once this Lagrange multiplier is determined, the successive approximations can be calculated through (2.19), i.e.,

$$\begin{aligned}u_1(t) &= u_0(t) + \int_{t_0}^{t} \mathrm{d}s\, \lambda(s,t)\left(Lu_0(s) + Nu_0(s) - f(s)\right)\\ u_2(t) &= u_1(t) + \int_{t_0}^{t} \mathrm{d}s\, \lambda(s,t)\left(Lu_1(s) + Nu_1(s) - f(s)\right)\\ &\vdots\end{aligned} \tag{2.21}$$

The VIM also suffers from some drawbacks. The main disadvantage the VIM has with respect to the ADM is the calculation of an exponentially increasing number

of useless terms, drastically slowing down the convergence and often introducing large divergences for higher values of the independent variables. Once again, modifications of the method have been proposed, which mostly included either cutting off higher-order terms before integration [20], or introducing nonphysical convergence-control parameters [21]. Nevertheless, the VIM remains one of the most widely-used iterative methods, partly because of the intuitive "plug-and-play" setup and the often larger region of convergence than the ADM for the same number of iterations needed.

A nontrivial extension to the VIM we will often use is the so-called VIM with Green function or GVIM [22]. In this method, the Lagrange multiplier is replaced by the Green function for the chosen linear operator. For initial-value problems, this amounts to choosing the optimal value for the Lagrange multiplier.

2.4 Homotopy perturbation method

The homotopy perturbation method (HPM) is the final iterative method we will use in this thesis. It was also developed by Ji-Huan He [23] as an alternative to the VIM. It is based on a Taylor series expansion of the solution around an embedding parameter p. First, consider again the most general differential equation (2.18) on the domain Ω, i.e.,

$$Lu + Nu - f(\boldsymbol{r}) = 0\,, \qquad \boldsymbol{r} \in \Omega \tag{2.22}$$

and construct a homotopy $v(\boldsymbol{r}, p) : \Omega \times [0,1] \to \mathbb{R}$ that satisfies

$$H(v,p) = (1-p)\,(Lv - Lu_0) + p\,(Lv + Nv - f(\boldsymbol{r})) = 0\,, \tag{2.23}$$

where we call $p \in [0,1]$ the embedding parameter. It is easy to see that the homotopy (2.23) continuously deforms the linear equation ($p = 0$)

$$H(v,0) = Lv - Lu_0 = 0 \tag{2.24}$$

into the nonlinear equation

$$H(v,1) = Lv + Nv - f(\boldsymbol{r}) = 0 \tag{2.25}$$

or, equivalently, u_0 into u. Now assume that the solution $v(\boldsymbol{r}, p)$ can be represented as a power series in p, i.e.,

$$v = \sum_{i=0}^{\infty} v_i p^i\,. \tag{2.26}$$

Eventually setting $p = 1$ results in the solution of equation (2.22).

The first step in this procedure is choosing an initial approximation u_0 and substituting (2.26) into the homotopy (2.23). One can then collect terms with the same powers of p, which need to be identically zero in order for the homotopy to be zero. This amounts to decomposing the problem into a set of linear differential equations that are easier to solve.

There is, however, one major drawback in choosing to use the HPM instead of the ADM or VIM. The second derivative of $N(v)$ with respect to v should be small, because the embedding parameter can become quite large, i.e., $p \to 1$. Aside from this, the computational complexity to solve the associated hierarchy of linear differential equations increases fast, requiring more computational power in each iteration. Additionally, sometimes the the solutions are not continuous in p, invalidating the extension of u_0 to v through the homotopy.

2.5 A note on iterative processes

All of the above methods (except the HPM) use versions of so-called *Picard* iteration. Consider a sequence $\{u_n\}$ and a (nonlinear) mapping $T : C \to C$, with C a nonempty convex subset of some normed space E. The Picard iterative process is the following

$$\begin{aligned} u_0 &= u \in C \\ u_{n+1} &= Tu_n\,. \qquad n \in \mathbb{N} \end{aligned} \tag{2.27}$$

For the BLUES function method, the ADM and the VIM, the action of the operator T on u_n is, respectively

$$\begin{aligned} Tu_n &= u_0 + B * \mathcal{R}u_n \\ Tu_n &= -L^{-1}\left(u_n + A_n\right) \\ Tu_n &= u_n + \int \mathrm{d}s\, \lambda(s)(Lu_n + Nu_n - f)\,. \end{aligned} \tag{2.28}$$

One can devise other iterative schemes, each of which offers some advantage over the others in a certain situation. While I will briefly touch upon some other procedures in this section, they will not be used in this thesis.

2.5.1 Mann's iterative procedure

Consider the following single-step procedure:

$$\begin{aligned} u_0 &= u \in C \\ u_{n+1} &= (1-\alpha_n)u_n + \alpha_n T u_n\,, \qquad n \in \mathbb{N} \end{aligned} \tag{2.29}$$

where $\{\alpha_n\}$ is a sequence of real numbers. This process is called Mann's iterative procedure [24]. This is sometimes used to increase the convergence of the ADM or VIM by considering the α_n's as convergence-control parameters [25, 26]. These can be optimally determined by minimising the residual square error of the approximants with respect to the α_n in each iteration. This is numerically expensive but can result in needing less approximants to achieve a desired accuracy. When $\alpha_n = \alpha\,, \forall n \in \mathbb{N}$, the procedure is called Krasnoselskii's iterative procedure.

2.5.2 Ishikawa iterative procedure

Consider the following two-step procedure:

$$\begin{aligned} u_0 &= u \in C \\ u_{n+1} &= (1-\alpha_n)u_n + \alpha_n T v_n \\ v_n &= (1-\beta_n)u_n + \beta_n T u_n\,, \qquad n \in \mathbb{N} \end{aligned} \tag{2.30}$$

where $\{\alpha_n\}$ and $\{\beta_n\}$ are sequences of real numbers. This process is called the Ishikawa iterative procedure [27]. As was the case for Mann's procedure, the parameters α_n and β_n can be used as convergence-control parameters.

2.5.3 Hybrid procedures

A final procedure can be created by combining Picard's and Krasnoselskii's method. This so-called hybrid Picard-Krasnoselskii's procedure can be described as follows,

$$\begin{aligned} u_0 &= u \in C \\ u_{n+1} &= T v_n \\ v_n &= (1-\lambda)u_n + \lambda T u_n\,. \qquad n \in \mathbb{N} \end{aligned} \tag{2.31}$$

Again, the parameter λ can be used to control the convergence.

The procedures outlined above are especially useful for *numerical* applications. Since in this thesis we are interested in purely analytical approximants, we will not use the other procedures but will defer to the literature on the topic.

2.6 Numerical solution methods

As a result of the fact that many of the equations I will study in this thesis have no (known) exact solution, the approximants generated by the different methods in this chapter need to be compared with a numerical solution of the differential equation at hand. For the chapters on ODEs, PDEs and CDEs I will use *Wolfram Mathematica*'s NDSolve function [28]. The NDSolve function is a generic numerical differential equation solver that can solve both ODEs and PDEs, either coupled or not. Generally, NDSolve discretizes the domain of the independent variable, say, a time t, and solves the equation for a sequence of steps of t, starting from a particular value. It uses an adaptive procedure to determine the size of the steps, reducing the step size when it detects that the solutions starts to vary rapidly within a region. Since NDSolve generates a numerical solution, all initial and boundary conditions must be specified completely.

For PDEs, the NDSolve function uses the method of lines (MOL) [29] to discretize all dimensions but one. This allows the techniques that are used for solving ODEs to be used in the context of PDEs. The true power of the NDSolve function lies in its adaptivity. When it is allowed to process the differential equation freely, it selects the method that is most appropriate for the equation. For example, in "stiff" problems most methods are unstable and generate rapidly varying solutions. NDSolve can detect this and automatically uses implicit methods to overcome the stiffness problem.

Given the flexibility and power of the NDSolve command when allowed to automatically select the best method, I will use this functionality in all of the previously mentioned chapters to generate the numerical solutions. However, Mathematica is not capable of solving FDEs. Hence, to generate the solutions shown in chapter 4, I use *Matlab* with the *fde12* package [30, 31] that uses the predictor-corrector method of Adams-Bashforth-Moulton [32].

Chapter 3

Ordinary differential equations

We study the application of the BLUES function method in the setting of ordinary differential equations (ODEs). Since the construction of the method for ODEs has been introduced in the previous chapter 2, we will not repeat it here. We apply the iterative procedure to four examples from theoretical physics that posses solitonic or travelling wave solutions and calculate approximants to the (unknown) exact solutions. We analyse numerically the convergence of the BLUES function method to the exact solution and show that in some cases the method is able to accurately capture the asymptotic behaviour, hence converging *globally*.

This chapter is based on the Letter *"Analytic iteration procedure for solitons and traveling wavefronts with sources"* [9] and the article *"BLUES iteration applied to nonlinear ordinary differential equations for wave propagation and heat transfer"* [33], both of which appeared in *Journal of Physics A: Mathematical and Theoretical*. It is supplemented with additional calculations and figures.

3.1 Dispersionless Camassa-Holm equation

The dimensionless Camassa-Holm (CH) equation with dispersion parameter $\kappa \geq 0$

$$u_t + 2\kappa u_x - u_{xxt} + 3uu_x = 2u_x u_{xx} + uu_{xxx}, \tag{3.1}$$

was introduced by Camassa and Holm in 1993 [34] as a model for the surface height $u(x,t)$ of shallow water waves above a flat bottom. We have implicitly written partial derivatives with a subscript, i.e. $u_t = \partial u/\partial t$. For positive κ, equation (3.1) results in smooth soliton solutions. However, here we will consider the limit $\kappa \to 0$ for which the dispersion vanishes, which is known to have piecewise analytic solitary wave solutions with a sharp peak where the first derivative is discontinuous. These peaked solitons were aptly named "peakons" by Camassa and Holm. The partial DE (3.1) can be converted to an ordinary DE by adopting a travelling-wave Ansatz $U(z) \equiv u(x,t)$ with co-moving coordinate $z = x - ct$, where c is the wave propagation velocity

$$-cU_z + cU_{zzz} + 3UU_z - 2U_zU_{zz} - UU_{zzz} = 0, \tag{3.2}$$

and boundary conditions $U(|z| \to \infty) = 0$. We can reduce this third-order DE to a second-order one by integrating over z,

$$-c(U - U_{zz}) + \frac{3}{2}U^2 - \frac{1}{2}U_z^2 - UU_{zz} = \alpha, \tag{3.3}$$

where α is an integration constant. Now $\alpha = 0$ in order to satisfy the boundary conditions. Introducing a co-moving Dirac-delta point source $\delta(z)$ at $z = 0$ with amplitude s, the integrated CH equation becomes

$$\mathcal{N}_z U(z) = \frac{1}{s}\left(-c(U(z) - U_{zz}(z)) + \frac{3}{2}U^2(z) - \frac{1}{2}U_z^2(z) - U(z)U_{zz}(z)\right) = \delta(z). \tag{3.4}$$

It can easily be seen that this equation admits a peakon solution of the form

$$U(z) = B(z) \equiv A\mathrm{e}^{-|z|}, \tag{3.5}$$

whenever the amplitude s of the source, the wave speed c, and the peakon amplitude A solve the constraint

$$s = 2A(A - c). \tag{3.6}$$

From this it immediately follows that $s = 0$ has two solutions: the trivial case $A = 0$ or the case $A = c$. The latter recovers the peakon solution of the dispersionless Camassa-Holm equation without point source.

We now derive heuristically a related linear DE which is also solved by (3.5) when the constraint (3.6) is satisfied. Setting $U = A$ while keeping the derivatives and neglecting the difference $U^2 - U_z^2$, results in the linear DE

$$\mathcal{L}_z U(z) = \frac{1}{s}(A - c)(U(z) - U_{zz}(z)) = \delta(z), \tag{3.7}$$

where $\mathcal{L}_z$ is a linear operator. The peakon solution (3.5) is a Green function for the linear DE and it can be used to construct an exact solution to the linear DE with arbitrary source ψ through the convolution $B * \psi$. Because the peakon solution solves both the nonlinear DE with a Dirac delta source and an associated linear DE with the same Dirac delta source, it is a BLUES function according to the narrow definition given in Chapter 2.

We construct a residual operator $\mathcal{R}_z U \equiv \mathcal{L}_z U - \mathcal{N}_z U$, which is defined through its action on U

$$\mathcal{R}_z U = \frac{1}{s}\left(A(U - U_{zz}) - \frac{3}{2}U^2 + \frac{1}{2}U_z^2 + UU_{zz}\right). \tag{3.8}$$

Note that the residual vanishes when applied to the BLUES function (3.5), $\mathcal{R}_z B = 0$.

We now consider the CH equation (3.4) with an arbitrary source ψ,

$$\mathcal{N}_z U(z) = \frac{1}{s}\left(-c(U(z) - U_{zz}(z)) + \frac{3}{2}U^2(z) - \frac{1}{2}U_z^2(z) - U(z)U_{zz}(z)\right) = \psi(z) \tag{3.9}$$

and the associated linear equation (3.7) with the same source $\psi(z)$,

$$\mathcal{L}_z U(z) = \frac{1}{s}(A - c)(U(z) - U_{zz}(z)) = \psi(z). \tag{3.10}$$

For the source $\psi(z)$ we can, e.g., choose an exponential corner source which resembles the peakon solution (3.5) but possesses a tuneable dimensionless decay length K,

$$\psi(z) = \frac{\mathrm{e}^{-|z|/K}}{2K}, \tag{3.11}$$

and which tends to a Dirac delta function in the limit $K \to 0$. The zeroth-order approximation (convolution) can be easily calculated for $K \neq 1$

$$\begin{aligned} U_\psi^{(0)}(z) = (B * \psi)(z) &= \frac{A}{2K}\int_{-\infty}^{\infty} \mathrm{d}z_0\, \mathrm{e}^{-|z-z_0|}\mathrm{e}^{-|z_0|/K} \\ &= \frac{A}{K^2-1}\left(K\mathrm{e}^{-|z|/K} - \mathrm{e}^{-|z|}\right). \end{aligned} \tag{3.12}$$

The calculation for $K = 1$ can be done in a similar way and results in the following simple expression

$$U_\psi^{(0)}(z) = \frac{A}{2}\mathrm{e}^{-|z|}(1 + |z|). \tag{3.13}$$

To calculate the first-order correction we use the residual operator (3.8) applied to the zeroth-order approximation, (3.12)

$$\mathcal{R}_z U_\psi^{(0)}(z) = \frac{A^2\left(-3(K+1)\mathrm{e}^{-2|z|/K} + (1+2K+3K^2)\mathrm{e}^{-|z|(1+1/K)}\right)}{2s(K-1)(K+1)^2}, \quad (3.14)$$

followed by convoluting this result with the BLUES function (3.5). The correction, $\Delta U_\psi^{(1,0)}(z) = U_\psi^{(1)}(z) - U_\psi^{(0)}(z)$, becomes for $K \neq 1, 2$

$$\begin{aligned}\Delta U_\psi^{(1,0)}(z) = -\frac{2A^3}{s(K^2-1)}\Bigg[&\frac{3K}{2(K^2-4)}\left(K\mathrm{e}^{-2|z|/K} - 2\mathrm{e}^{-|z|}\right) \\ &+ \frac{K}{K+1}\mathrm{e}^{-|z|(1+1/K)} - K\mathrm{e}^{-|z|/K}\Bigg],\end{aligned} \quad (3.15)$$

while for $K = 1$ and $K = 2$ the corrections are given respectively by

$$\Delta U_\psi^{(1,0)}(z) = U_\psi^{(1)}(z) - U_\psi^{(0)}(z) = \frac{A^3}{12s}\left[(13+6|z|)\mathrm{e}^{-2|z|} - (8-12|z|)\mathrm{e}^{-|z|}\right] \quad (3.16)$$

and

$$\Delta U_\psi^{(1,0)}(z) = U_\psi^{(1)}(z) - U_\psi^{(0)}(z) = \frac{A^3}{18s}\left[24\mathrm{e}^{-|z|/2} - 8\mathrm{e}^{-3|z|/2} - 9(|z|+1)\mathrm{e}^{-|z|}\right]. \quad (3.17)$$

Higher-order approximants can be calculated in the same way but require the use of symbolic mathematical software, since they are hard to compute manually. Using the approximate analytical solutions obtained, we can now compare the analytical and numerical solution of the equation (3.9). For the source ψ we choose the previously used normalised exponential corner source (3.11), with, in this example, a long decay length ($K = 10$). In Fig. 3.1a, we compare plots of the zeroth approximant (convolution) $U_\psi^{(0)}(z)$ and the first approximant $U_\psi^{(1)}(z)$ with the numerical solution $U_{\mathrm{num}}(z)$. Note that there is no need for the source to be sharp. For values of K in the range $10^{-3} \leq K < 10^3$, the convolution accurately follows the numerical solution and successive higher approximants improve upon this solution. A zoom about the maximum at $z = 0$ is show in Fig. 3.1b.

Note that the iteration sequence converges to the BLUES function (3.5) for a sharply localized source, i.e., in the limit $K \to 0$ for the corner source. In this limit, the zeroth approximant converges to the BLUES function and all higher corrections vanish.

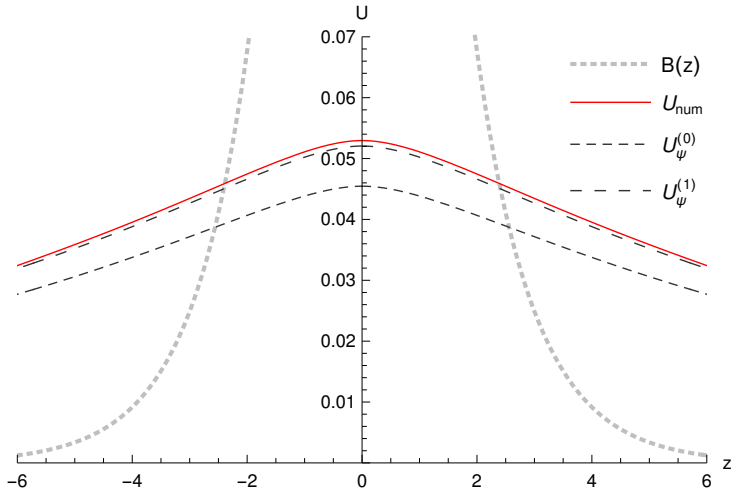

(a)

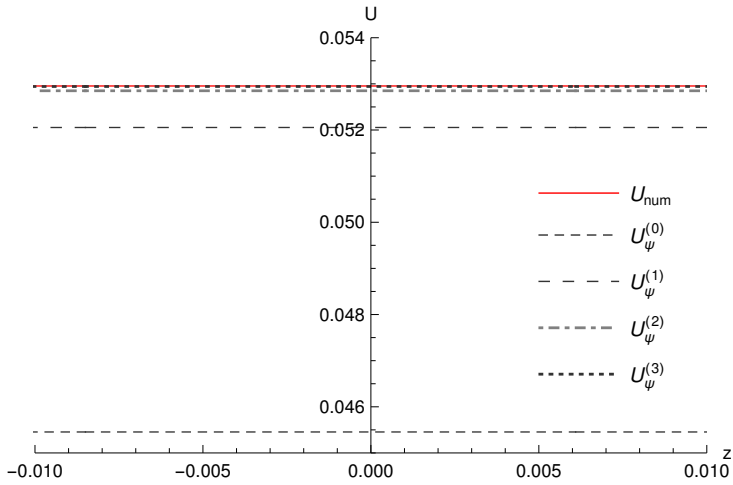

(b)

Figure 3.1: **(a)** Soliton solution to the nonlinear Camassa-Holm DE (3.9) with the exponential corner source (3.11). The numerical solution $U_{\text{num}}(z)$ (red, full line), the zeroth approximant $U_\psi^{(0)}(z)$ (black, dashed line) and the first approximant $U_\psi^{(1)}(z)$ (black, wider spaced dashed line) are compared. Also shown is the BLUES function $B(z)$ (grey, dotted line). Parameter values are $c = -5/2$, $A = 1/2$, and $K = 10$ (broad source). **(b)** A zoomed-in view around the maximum of $U(z)$. The approximations are shown up to and including 3rd iteration. On this scale $U_\psi^{(3)}(z)$ is on top of the numerical solution.

The residual function $\mathcal{R}_z U_\psi^{(n)}(z)$ for arbitrary iteration n can be computed as was done in equation (3.14) for $n = 0$. These functions for different iterations are compared in Fig. 3.2, where the residual operator applied to the numerically exact solution $U_{\text{num}}(z)$ is also shown. Note that for the CH equation, the higher residuals are all localised and vanish at positive and negative infinity, ensuring the boundedness of the general solution.

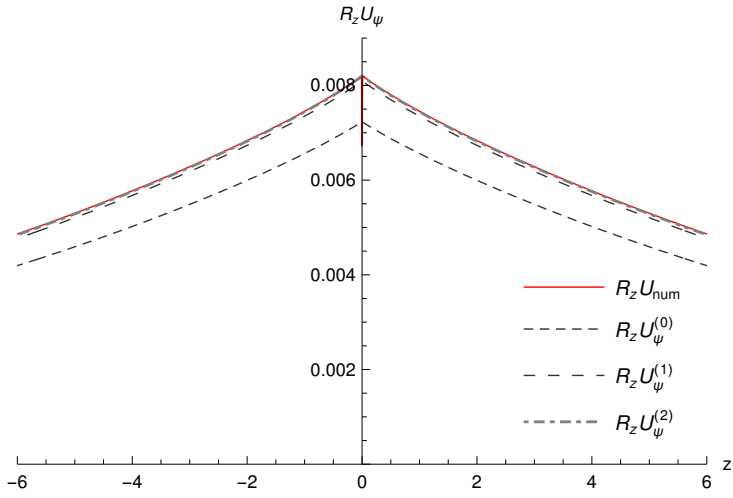

Figure 3.2: Residual functions $\mathcal{R}_z U_\psi^{(n)}(z)$ of the n-th order approximants $U_\psi^{(n)}(z)$ for the nonlinear Camassa-Holm DE with exponential corner source (3.11) for $n = 0, 1$ and 2. Also shown is the residual in the numerically exact solution $U_{\text{num}}(z)$ (red, full line). Parameter values are $c = -5/2$, $A = 1/2$, and $K = 10$.

By numerically inspecting the values of the terms in the iteration sequence at the maximum in $z = 0$ for increasing order n, we can gain some insight into the convergence of the sequence. By inspecting Figs 3.1b and 3.3, we observe that the maximum of the different approximants converges to the numerically determined maximum. When the difference of subsequent approximants $|\Delta U_\psi^{(n,n-1)}(0)| \equiv |U_\psi^{(n)}(0) - U_\psi^{(n-1)}(0)|$ is studied, we see that this difference decays exponentially to zero, numerically indicating that the sequence converges exponentially fast. Note that this is also the case when studying the convergence of the residual function $\mathcal{R}_z U_\psi^{(n)}(z)$ to the numerically exact solution $\mathcal{R}_z U_{\text{num}}(z)$.

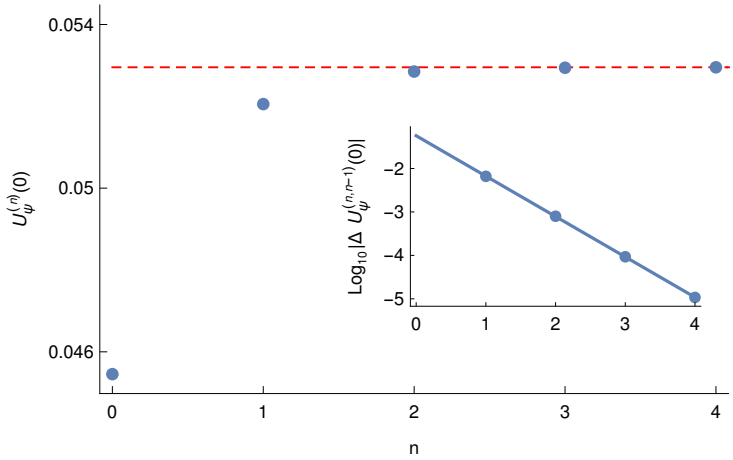

Figure 3.3: Peak value of the approximants $U_\psi^{(n)}(0)$ versus order n for the nonlinear Camassa-Holm DE. The numerically exact peak value (red, dashed line) is also shown. **Inset:** A $\log_{10}$ semi-log plot of the increments $|\Delta U_\psi^{(n,n-1)}(0)|$ of the approximants versus n, and a linear fit. Parameter values are $c = -5/2$, $A = 1/2$, and $K = 10$.

3.2 The Burgers equation

As a starting point for our second example, consider the diffusion equation which describes the propagation of a density $u(x,t)$

$$u_t - \nu u_{xx} = 0, \tag{3.18}$$

with ν the diffusion coefficient. After scaling the variables and adopting a travelling-wave Ansatz $z = x - ct$, the diffusion equation becomes a linear ordinary DE. Adding a co-moving Dirac delta source, the equation becomes

$$\mathcal{L}_z U(z) \equiv -U_z(z) - kU_{zz}(z) = \delta(z), \tag{3.19}$$

where k is a dimensionless constant. We consider the wavefront boundary conditions $U_z(z \to -\infty) = 0$ (and $U(z \to -\infty) > 0$) and $U(z \to \infty) = 0$. The exact solution (in every point including $z = 0$) is the piecewise analytic exponential tail,

$$B(z) = \begin{cases} 1, & z < 0 \\ \mathrm{e}^{-z/k}, & z \geq 0 \end{cases} \tag{3.20}$$

and the wavefront velocity is $c(k) = 1/k$. We can now include an arbitrary kind of nonlinearity to the equation, say, a nonlinear convective term uu_x, which

turns the diffusion equation into the well-known viscous Burgers equation [35]

$$u_t + u\,u_x - \nu\,u_{xx} = 0, \tag{3.21}$$

which is widely used in, e.g., fluid mechanics [36], nonlinear acoustics, traffic flow modelling, etc. By again transforming to the co-moving frame and adding a source $\psi(z)$, equation (3.21) can be rewritten as

$$\mathcal{N}_z U(z) \equiv -U_z(z) + kU(z)U_z(z) - kU_{zz}(z) = \psi(z), \tag{3.22}$$

which is compatible with our boundary conditions provided $0 < k < 1/2$, as can be seen by applying a sum rule (see further). Once again, we can try to solve this equation by making use of superposition based on $B(z)$. However, the main difference with the previous problem (CH soliton) is that now the piecewise analytic solution (3.20) does not solve (3.22) for a point source because the nonlinear term does not vanish at $z > 0$ and is not compensated at $z = 0$. Surprisingly, this does not spoil the method because it turns out that the condition (2.1) is not necessary. Therefore we can still use the $B(z)$ defined in equation (3.20) as a BLUES function and investigate the iteration sequence even though this $B(z)$ is not a BLUES function according to the narrow definition of Chapter 2. The residual of the diffusion equation with respect to the Burgers equation is

$$\mathcal{R}_z U = -kUU_z \tag{3.23}$$

and now the residual is nonzero when applied to the BLUES function, $\mathcal{R}_z B(z) \neq 0$. Consequently, when the source in the nonlinear DE is taken to be a Dirac delta source, the sequence converges to a new function which is different from the BLUES function and which can be calculated as follows, to arbitrary order,

$$B * \phi \;\sim\; B + B * \mathcal{R}_z(B + B * \mathcal{R}_z(B + B * \mathcal{R}_z(B + ...))). \tag{3.24}$$

For an arbitrary source ψ, the zeroth approximant is $B * \psi$. Choosing again the exponential corner source (3.11), we obtain for $K \neq k$

$$U_\psi^{(0)}(z) \equiv (B * \psi)(z) = \frac{1}{2}\begin{cases} 2 - \frac{K}{K+k}\mathrm{e}^{z/K}, & z < 0 \\ \frac{K}{K-k}\mathrm{e}^{-z/K} - \frac{2k^2}{K^2-k^2}\mathrm{e}^{-z/k} & z \geq 0, \end{cases} \tag{3.25}$$

while for $K = k$ the convolution product results in

$$U_\psi^{(0)}(z) \equiv (B * \psi)(z) = \begin{cases} 1 - \frac{\mathrm{e}^{z/k}}{4}, & z < 0 \\ \left(\frac{3}{4} + \frac{z}{2k}\right)\mathrm{e}^{-z/k} & z \geq 0. \end{cases} \tag{3.26}$$

The method for finding higher solutions is straightforward but tedious. A calculation for the first approximant (A.3) is performed in the appendix A.

This time we illustrate our results for the choice of a sharp source with $K/k = 1/5$. We compare the approximate solutions calculated using the sequence with the numerically exact solution. In Fig. 3.4a, the zeroth (short dashed line) and the first approximant (long dashed line) are compared with the numerical solution (red full line). Note that the zeroth solution (the simple convolution) approaches unity for $z \to -\infty$ but that the numerical solution approaches a different constant value. This value can easily be found through a sum rule, obtained by integrating the full Burgers equation (3.22) with source ψ over the real line and solving for $U_\psi(-\infty)$, resulting in the quadratic equation

$$\frac{k}{2}U_\psi^2(-\infty) - U_\psi(-\infty) + \alpha = 0, \tag{3.27}$$

with solutions $U_\psi(-\infty)_\pm = (1 \pm \sqrt{1-2k\alpha})/k$ and where α is the integral of the source over the real line, called the 1-norm of the source. For $k = 1/3$ and the source normalised to unity $\alpha = 1$, the asymptotic constant for our solution is $U_\psi(-\infty)_- = 1.268...$ Higher iterations are shown in Fig. 3.4b, where a zoomed-in view around $z = 0$ reveals the convergence of the sequence. This is numerically confirmed in Fig. 3.6 where once again the convergence is exponentially fast. We can also study the higher residual functions $\mathcal{R}_z U_\psi^{(n)}$ and confirm that the convergence to $\mathcal{R}_z U_{\text{num}}$ is exponentially fast. Again, in every iteration the residuals are localised and vanish at positive and negative infinity, ensuring the boundedness of the general solution.

Note that the source need not be normalised to unity. The method also works for sources whose 1-norm is another real number, for instance zero. In Fig. 3.7a the solution to equation (3.22) is shown for a source ψ, which is an odd function of z

$$\psi(z) = A \sin\left(\frac{z}{K}\right)\frac{\mathrm{e}^{-|z|/K}}{2K}, \tag{3.28}$$

with $A > 0$. This choice of $\psi(z)$ has the interpretation of a sink for negative values of z, smoothly connected to a source for positive values of z. Since the source is odd, the 1-norm is zero and the solution at negative infinity, predicted by the sum rule (3.27), is $U_\psi(-\infty) = 0$, which is confirmed by the numerical solution shown in Fig. 3.7a, for $A = 10$.

The zeroth solution of Burgers' equation (3.22) with the smooth sink/source combination (3.28) is given by

$$U_\psi^{(0)}(z) = \frac{AK}{4}\begin{cases} \left(\frac{(2k+K)\cos\frac{z}{K} - K\sin\frac{z}{K}}{2k^2+2kK+K^2}\right)\mathrm{e}^{z/K}, & z < 0 \\ \left(\frac{(K-2k)\cos\frac{z}{K} + K\sin\frac{z}{K}}{2k^2-2kK+K^2}\right)\mathrm{e}^{-z/K} + \frac{8k^3}{4k^4+K^4}\mathrm{e}^{-z/k}, & z \geq 0, \end{cases} \tag{3.29}$$

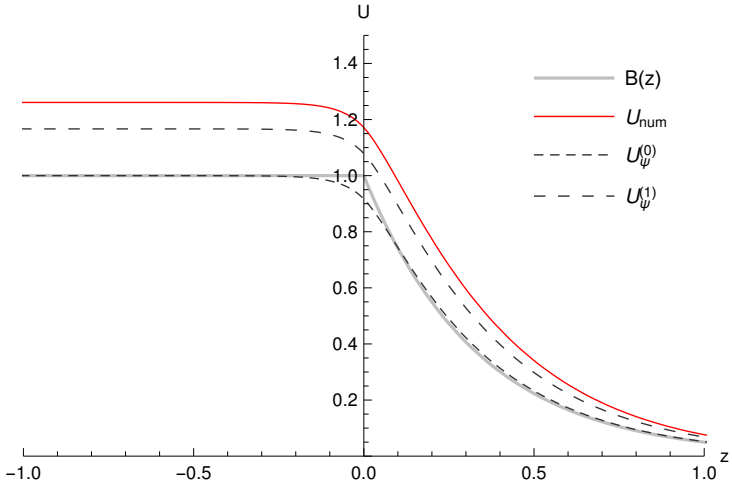

(a)

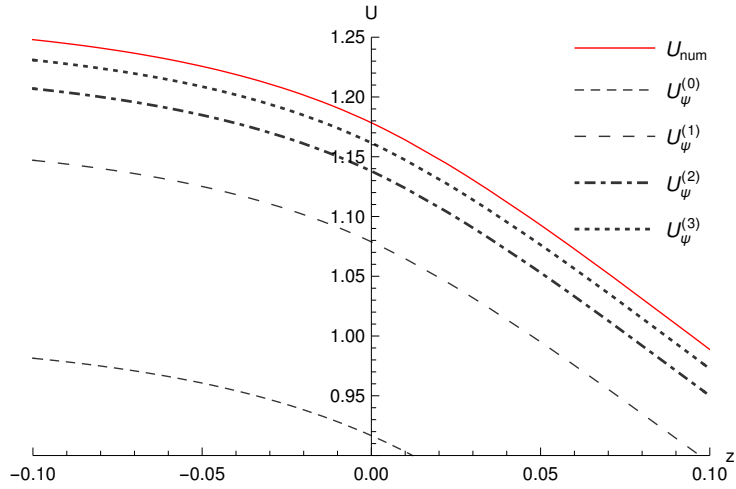

(b)

Figure 3.4: **(a)** Travelling wavefront solution to the nonlinear Burgers DE (3.22) with an exponential corner source (3.11). The numerical solution $U_{\text{num}}(z)$ (red, full line), the zeroth approximant $U_\psi^{(0)}(z)$ (black, dashed line) and the first approximant $U_\psi^{(1)}(z)$ (black, wider spaced dashed line) are compared. The BLUES function (grey) is also shown. **(b)** A zoomed-in view around the shoulder of the wavefront. The approximants are shown up to and including 3rd iteration. Parameter values are $k = 1/3$ and $K/k = 1/5$ (sharp source).

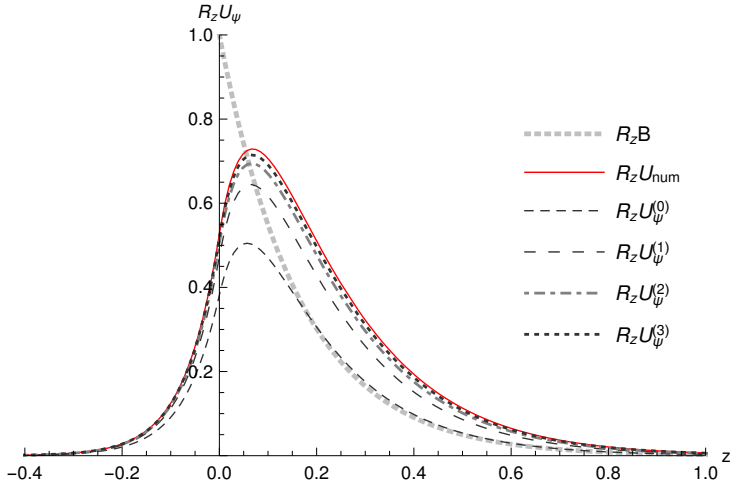

Figure 3.5: Residual function $\mathcal{R}_z U_\psi^{(n)}(z)$ of the approximants $n = 0, 1, 2, 3$ for the nonlinear Burgers DE (3.22) with exponential corner source (3.11). The residual operator applied to the numerical solution (red, full line) and to the BLUES function (grey, dotted line) are also shown. The latter is zero for $z < 0$. Parameter values are $k = 1/3$ and $K/k = 1/5$.

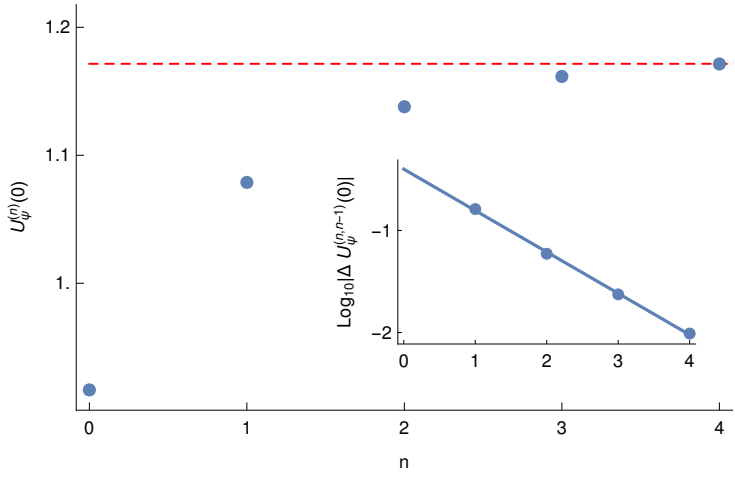

Figure 3.6: Wavefront values $U_\psi^{(n)}(0)$ versus iteration n for the nonlinear Burgers DE. The numerically exact value (red, dashed line) is also shown. **Inset:** A $\log_{10}$ semi-log plot of the increments $|\Delta U_\psi^{(n,n-1)}(0)|$ of the approximants versus n, and a linear fit. Parameter values are $k = 1/3$ and $K/k = 1/5$.

which decays to zero at negative infinity. Note that the solution now has the shape of a travelling pulse or soliton, in contrast with the kink solution of the model with the exponential corner source (3.11). By changing the functional form of the source, one can control the shape of the solution. Note that the BLUES function is independent of the choice of the source, and is the same as for the travelling wave solution studied earlier. The convergence to the numerically exact solution is again exponentially fast, as is shown in detail in the zoom of the region around the maximum, see Fig. 3.7b. This can also be inferred by inspection of the residual functions $\mathcal{R}_z U_\psi^{(n)}(z)$ shown in Fig. 3.8. The exponential convergence is illustrated quantitatively in Fig. 3.9.

3.3 The damped nonlinear oscillator

We now start from a general linear wave equation in one dimension with a co-moving Dirac delta source with amplitude s

$$u_{tt} - u_{xx} + \gamma u_x + u = s\,\delta(x - ct) \tag{3.30}$$

and look for travelling wave solutions by once more transforming to the coordinate $z = x - ct$

$$\alpha U_{zz}(z) + \gamma U_z(z) + U(z) = s\,\delta(z), \tag{3.31}$$

where $\alpha = c^2 - 1$. It can easily be seen that this DE is solved by the Green function

$$B(z) \equiv \begin{cases} 0 & z < 0 \\ \sin\left(\frac{\lambda z}{2\alpha}\right) \mathrm{e}^{-\frac{\gamma z}{2\alpha}} & z \geq 0, \end{cases} \tag{3.32}$$

with $\lambda = \sqrt{4\alpha - \gamma^2}$ and source amplitude $s = \lambda/2$. Now an arbitrary nonlinear term can be added, which we choose to be the cubic-quintic function $\beta U^3 + \xi U^5$, where β and ξ are tuneable parameters. Altogether the nonlinear wave equation with an arbitrary source is

$$\alpha U_{zz}(z) + \gamma U_z(z) + U(z) + \beta U^3(z) + \xi U^5(z) = s\psi(z), \tag{3.33}$$

where again the amplitude is $s = \lambda/2$ and the 1-norm of the source $\psi(z)$ is unity. This DE is a basic model for a myriad of physical systems. When β and ξ are chosen to be $-1/3!$ and $1/5!$ respectively, the terms $U + \beta U^3 + \xi U^5$ can be interpreted as the first three nonzero terms in the sine Taylor series. Including higher-order terms in the series, one can construct the nonlinear DE

$$\alpha U_{zz}(z) + \gamma U_z(z) + \sin U(z) = s\psi(z), \tag{3.34}$$

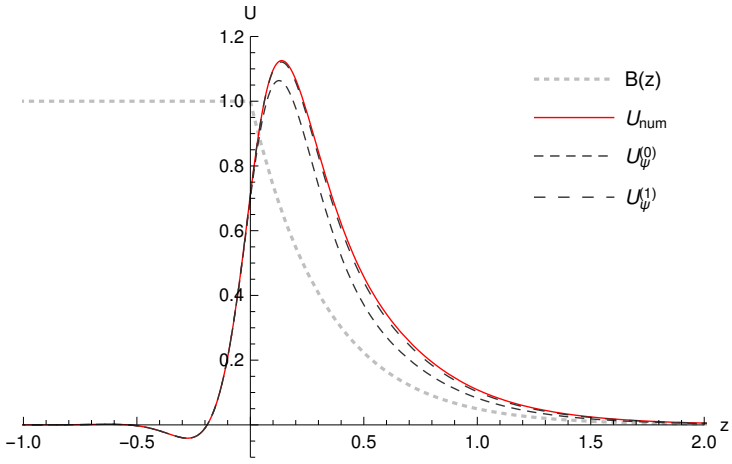

(a)

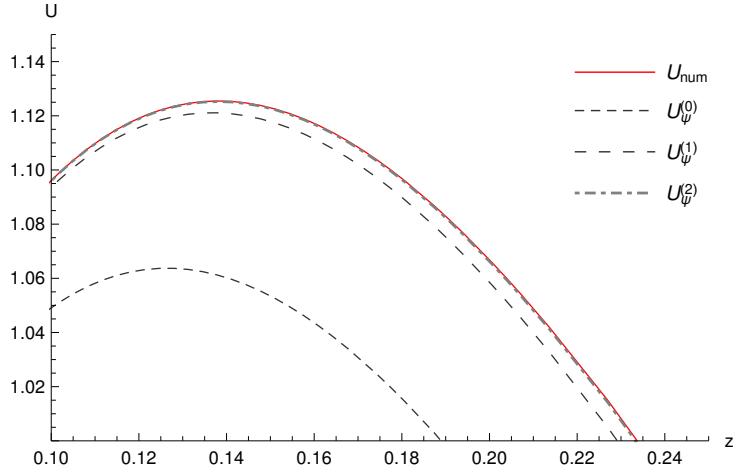

(b)

Figure 3.7: **(a)** Travelling pulse solution to the nonlinear Burgers DE (3.22) with source (3.28). The numerical solution U_{num} (red, full line), the zeroth $U_\psi^{(0)}$ (black, dashed line) and the first approximants $U_\psi^{(1)}$ (black, wider spaced dashed line) are compared. The BLUES function $B(z)$ is also shown (grey, dotted line).**(b)** A zoomed-in view around the maximum of the pulse. The approximants are shown up to and including 2nd iteration. Parameter values are $k = 1/3$, $K/k = 1/3$ and $A = 10$.

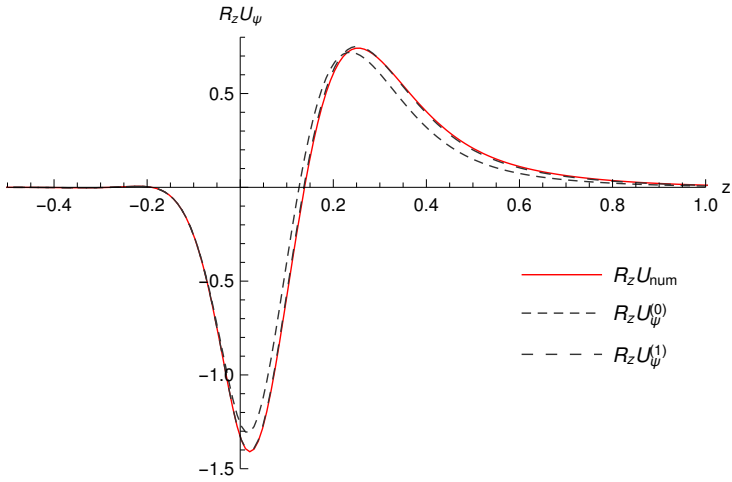

Figure 3.8: Residual function $\mathcal{R}_z U_\psi^{(n)}$ of the approximants for the nonlinear Burgers DE (3.22) with source (3.28). The residual operator applied to the numerical solution (red, full line) is also shown. Only $\mathcal{R}_z U_\psi^{(0)}$ and $\mathcal{R}_z U_\psi^{(1)}$ are shown, higher residual functions coincide with the numerical solution on this scale. Parameter values are $k = 1/3$, $K/k = 1/3$ and $A = 10$.

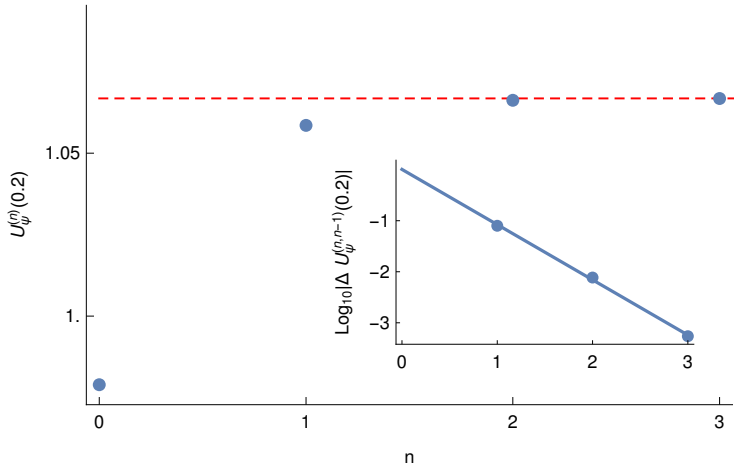

Figure 3.9: Pulse values $U_\psi^{(n)}(0.2)$ versus iteration n for (3.22). The numerically exact value (red, dashed line) is also shown. **Inset:** A $\log_{10}$ semi-log plot of the increments $|\Delta U_\psi^{(n,n-1)}(0.2)|$ of the approximants versus n, and a linear fit. Parameter values are $k = 1/3$, $K/k = 1/3$ and $A = 10$.

which is an equation for the damped and driven Sine-Gordon model [37], often used to describe the dynamics of Josephson junctions in superconductors [38, 39]. Another important application of equation (3.33) is the cubic-quintic Duffing oscillator, which is used to describe damped harmonic motion in a nontrivial potential and has become a paradigm for the study of chaos. For computational purposes we will only include the terms in the sine Taylor series up to and including third order, so we will choose $\xi = 0$.

Once more following the procedure outlined in Section 2.1, we construct the residual operator $\mathcal{R}_z U$ as (with $\xi = 0$)

$$\mathcal{R}_z U \equiv -\frac{\beta}{s} U^3 \tag{3.35}$$

and use this to calculate higher approximants using the Green function $B(z)$ given in (3.32) as BLUES function in the iteration sequence (6.53). The zeroth approximant can be calculated by performing the convolution integral (6.54) with BLUES function (3.32) and normalised exponential corner source (3.11), resulting in

$$(B * \psi)(z) = \begin{cases} \frac{K\lambda}{4C_+} \mathrm{e}^{z/K} & z < 0 \\ \left[A \sin\left(\frac{\lambda z}{2\alpha}\right) - B\lambda \cos\left(\frac{\lambda z}{2\alpha}\right)\right] \frac{\mathrm{e}^{-\frac{\gamma z}{2\alpha}}}{2} + \frac{K\lambda}{4C_-} \mathrm{e}^{-z/K} & z \geq 0, \end{cases} \tag{3.36}$$

where the constants $A, B, C_\pm$ are introduced to simplify notation. They are given by combinations of α, γ and K:

$$\begin{aligned} A &= \frac{2\alpha^2 - K^2\gamma^2 + 2\alpha K^2}{\alpha^2 - K^2\gamma^2 + 2\alpha K^2 + K^4} \\ B &= \frac{K^2\gamma}{\alpha^2 - K^2\gamma^2 + 2\alpha K^2 + K^4} \\ C_\pm &= \alpha \pm K\gamma + K^2. \end{aligned} \tag{3.37}$$

Higher iterations can in principle be calculated using equation (6.53) but in practice this is not feasible without the aid of mathematical software.

In Fig. 3.10a, a comparison between the numerically exact solution and both the zeroth approximant and the first approximant is made. On this scale the first approximant is globally better. While the first approximant is already useful, the second is shown to be a significantly better approximation. In Fig. 3.10b a zoomed-in view around the first minimum of the wave shows that the zeroth and first approximants intersect at some point, indicating that locally

the zeroth approximant is a better approximation. On this scale the second approximant is on top of the numerically exact solution. Once more we analyse the convergence of the iteration sequence to the exact solution. In Fig. 3.12 the value of the approximants at $z = 2$ for iterations $n = 0, 1$ and 2 are shown. The inset shows that the convergence to the exact solution is again exponentially fast. The higher residual functions are shown in Fig. 3.11 together with the residual operator (3.35) applied to the numerically exact solution (red, full line). Note that the residual functions are negative in the domain around the global maximum of the exact solution $U(z)$, where $U > 0$, that they are zero (with a cubic dependence on z) where the curves of Fig. 3.11 change sign, and that they are positive in the domain around their first minimum, where $U < 0$, indicating that higher corrections have respectively negative and positive sign relative to the zeroth approximant. This is obvious in view of the simple form of the residual (3.35).

In the limit $K \to 0$, the chosen source converges to the Dirac delta source used to calculate the BLUES function (3.32). Because the BLUES function does not solve (3.33), the sequence converges (exponentially fast) to a nontrivial function. One can calculate the first terms in this expansion by setting $\psi(z) = \delta(z)$ in equations (6.54) and (6.53). To zeroth iteration, the convolution is identical to the BLUES function. To first iteration, the solution with a delta function source is given by

$$U_\delta^{(1)}(z) = B(z) - \frac{\beta}{s} \int_{-\infty}^{\infty} B(z - z_0) B(z_0)^3 \mathrm{d}z_0. \tag{3.38}$$

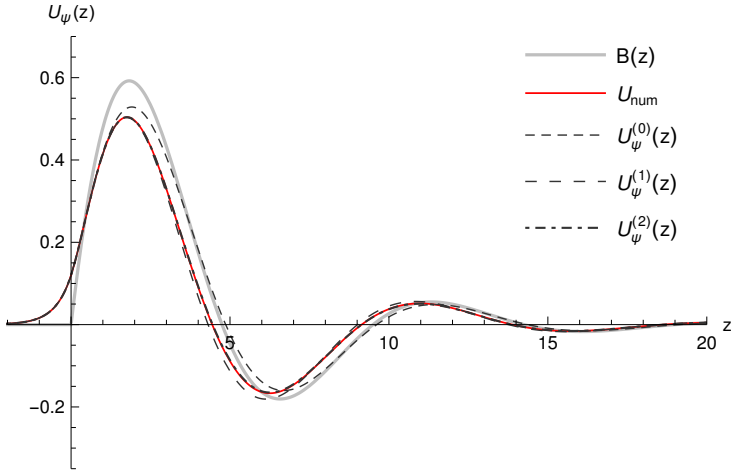

(a)

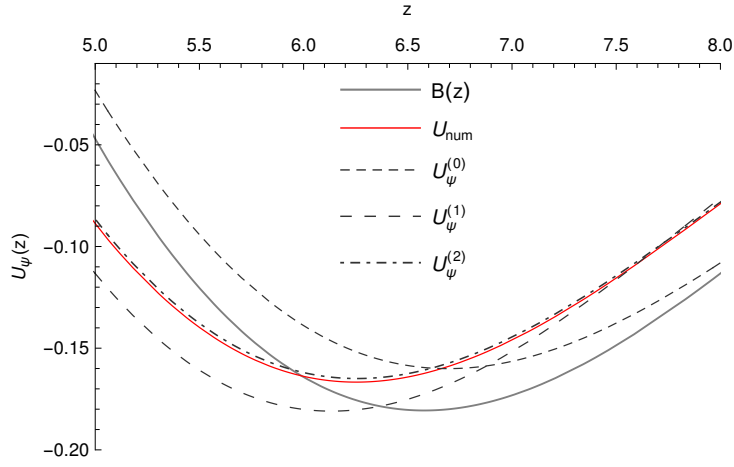

(b)

Figure 3.10: **(a)** Travelling wave solution to the nonlinear wave equation (3.33) with an exponential corner source (3.11). The numerical solution $U_{\rm num}(z)$ (red, full line), the zeroth $U_\psi^{(0)}(z)$ (black, dashed line), first $U_\psi^{(1)}(z)$ (black, wider spaced dashed line) and the second $U_\psi^{(2)}(z)$ (black, dot-dashed line) approximants are compared. The BLUES function (grey, solid line) is also shown. **(b)** A zoomed-in view around the global minimum of the wave. The approximants are shown up to and including 2nd iteration. Parameter values are $\alpha = 2$, $\gamma = 1$, $\beta = 1$, $\xi = 0$ and $K = 1/2$.

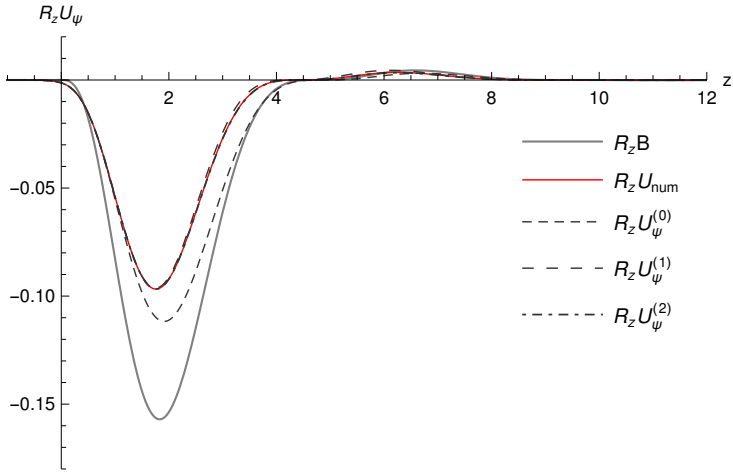

Figure 3.11: Residual function $\mathcal{R}_z U_\psi^{(n)}(z)$ of the approximants for the nonlinear wave equation (3.33) with exponential corner source (3.11). The residual operator applied to the numerical solution (red, full line) is also shown. Parameter values are $\alpha = 2$, $\gamma = 1$, $\beta = 1$, $\xi = 0$ and $K = 1/2$.

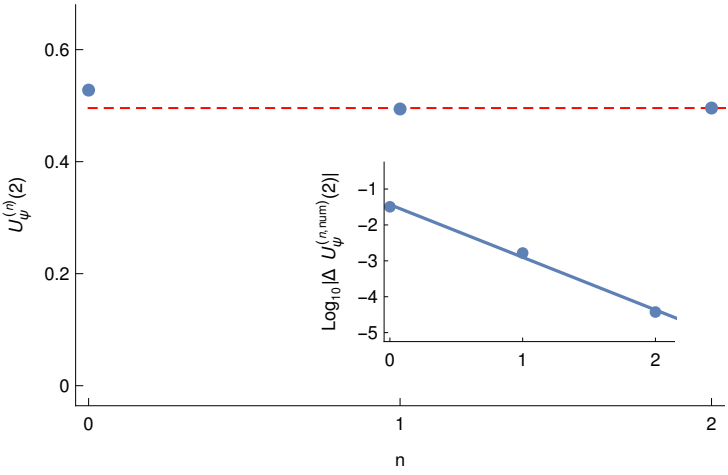

Figure 3.12: Wavefront values $U_\psi^{(n)}(2)$ at $z = 2$ versus iteration n for the nonlinear wave equation (3.33). The numerically exact value (red, dashed line) is also shown. **Inset:** A $\log_{10}$ semi-log plot of the increments $|\Delta U_\psi^{(n,n-1)}(2)|$ of the approximants versus n, and a linear fit. Parameter values are $\alpha = 2$, $\gamma = 1$, $\beta = 1$, $\xi = 0$ and $K = 1/2$.

3.4 The Fisher equation

For this final example, we choose once more the diffusion equation (3.19) to be the linear operator and add a reaction-type nonlinearity and a source $\psi(z)$ to obtain the forced Fisher equation [40] in co-moving coordinates, i.e.,

$$\mathcal{N}_z U(z) = -U_z(z) - kU_{zz}(z) - kU(z)(1-U(z)) = \psi(z)\,, \tag{3.39}$$

with boundary conditions $U(z\to\infty)\to 0$ and $U(z\to-\infty)\to 1$. Equation (3.39) governs the dimensionless density of some chemical or species experiencing diffusion and growth. The limit at negative infinity signifies the saturation of the density at the normalised value 1. The residual operator is now

$$\mathcal{R}_z U = kU(1-U) \tag{3.40}$$

From the linear operator (3.19), the BLUES function is once again the exponential tail function (3.20). If we now choose the source $\psi(z)$ to be the exponential corner source (3.11), the zeroth approximant to the nonlinear DE (3.39) is again either equation (3.25) or (3.26), which we will repeat here for $K \neq k$

$$U^{(0)}_{\psi}(z) \equiv (B*\psi)(z) = \frac{1}{2}\begin{cases} 2 - \frac{K}{K+k}\mathrm{e}^{z/K}, & z<0 \\ \frac{K}{K-k}\mathrm{e}^{-z/K} - \frac{2k^2}{K^2-k^2}\mathrm{e}^{-z/k} & z\geq 0, \end{cases} \tag{3.41}$$

while for $K=k$ the convolution product results in

$$U^{(0)}_{\psi}(z) \equiv (B*\psi)(z) = \begin{cases} 1 - \frac{\mathrm{e}^{z/k}}{4}, & z<0 \\ \left(\frac{3}{4} + \frac{z}{2k}\right)\mathrm{e}^{-z/k} & z\geq 0. \end{cases} \tag{3.42}$$

Higher approximants can easily be calculated by iteration but will not be given here. We will, however, calculate the first approximant for $k \neq K$ in the appendix A.2. Note that the first approximant approaches a constant which is not unity at negative infinity and consequently does not obey the boundary condition. One can calculate the non-trivial constant by considering the limit of the first approximant at negative infinity, i.e.,

$$\begin{aligned} U_c \equiv \lim_{z\to-\infty} U^{(1)}(z) &= 1 + \lim_{z\to-\infty}\int_{-\infty}^{\infty} B(z-z')\mathcal{R}_{z'}U^{(0)}_{\psi}(z')\mathrm{d}z' \\ &= 1 + \int_{-\infty}^{\infty} \mathcal{R}_{z'}U^{(0)}_{\psi}(z')\mathrm{d}z' \\ &= 1 + \frac{k\left(2k^3 + 4k^2K + 6kK^2 + 3K^3\right)}{4(k+K)^2}\,. \end{aligned} \tag{3.43}$$

In Fig. 3.13a, the zeroth and first approximants are shown together with the numerically exact solution and the BLUES function (3.20). In Fig. 3.13b, a zoomed-in representation of the shoulder of the wavefront is shown. The numerical solution is compared with approximants up to fourth iteration. Note that while all approximants obey the boundary condition $U(z \to \infty) \to 0$, only the zeroth approximant approaches unity for $z \to -\infty$. This is a consequence of the lack of localization of the residual for higher iterations. This is shown in Fig. 3.14. The numerical residual function $\mathcal{R}_z U_{num}(z)$ and the zeroth residual function are localized, but higher residual functions are not anymore. This corresponds to a divergence of the approximants of higher iterations.

The local convergence of the approximants can once more be assessed by studying the value of the approximants for a fixed value of z. However, because of the divergence of the approximants for $z \to -\infty$, one has to be careful in choosing the value of z. In this case, we have chosen for $z = -1$, which can be seen to lie within a reasonable region of convergence. The results are shown in Fig. 3.15. Note that within the region of convergence, the approximants converge exponentially fast to the numerically exact solution.

In this chapter we have shown that the BLUES function method can be used to calculate accurate approximations for various nonlinear ODEs, particularly for travelling-wave solutions to one-dimensional problems within fluid dynamics and mathematical biology, where the source is co-moving. We will now study the application of the BLUES function method for fractional differential equations in one variable.

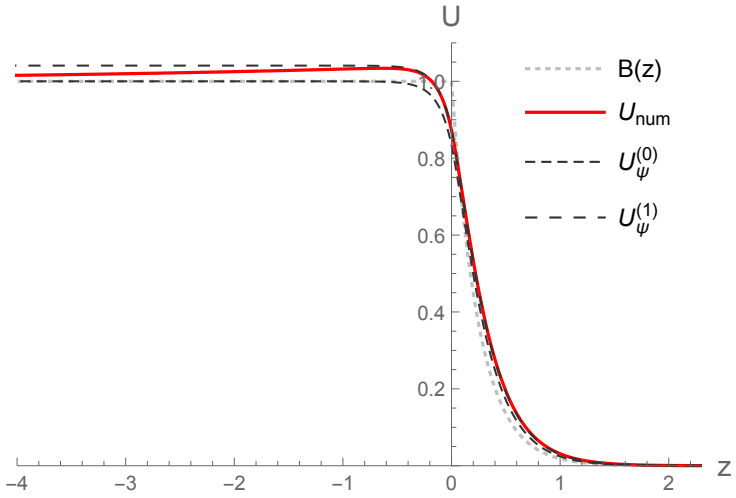

(a)

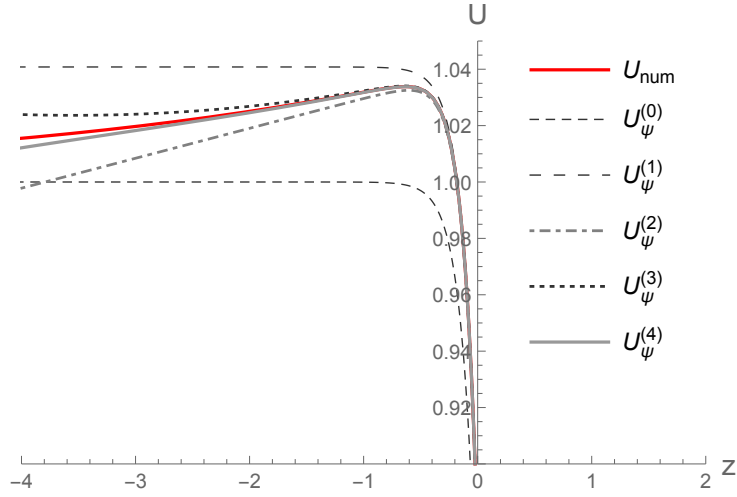

(b)

Figure 3.13: **(a)** Travelling wavefront solution to the nonlinear Fisher DE (3.22) with an exponential corner source (3.11). The numerical solution $U_{\text{num}}(z)$ (red, full line), the zeroth $U_\psi^{(0)}(z)$ (black, dashed line) and the first $U_\psi^{(1)}(z)$ (black, wider spaced dashed line) approximants are compared. The BLUES function (grey) is also shown. **(b)** A zoomed-in view around the shoulder of the wavefront. The approximants are shown up to and including 4th iteration. Parameter values are $k = 1/4$ and $K/k = 1/2$.

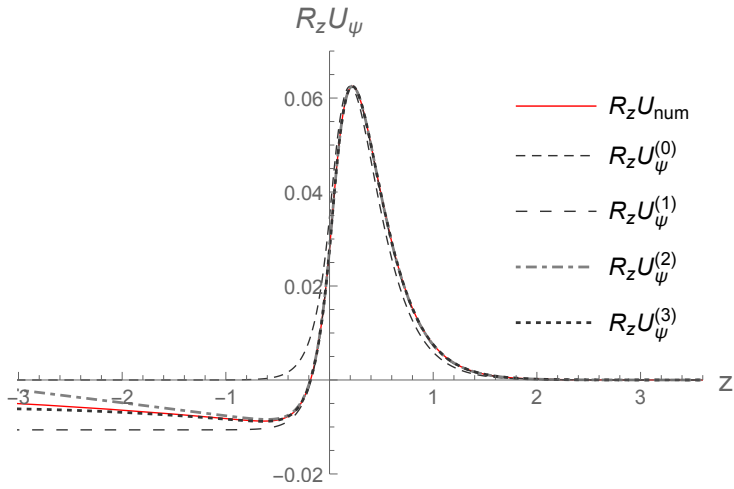

Figure 3.14: Residual function $\mathcal{R}_z U_\psi^{(n)}(z)$ of the approximants $n = 0, 1, 2, 3$ for the nonlinear Fisher DE with exponential corner source (3.11). The residual operator applied to the numerical solution (red, full line) is also shown. Parameter values are $k = 1/4$ and $K/k = 1/2$.

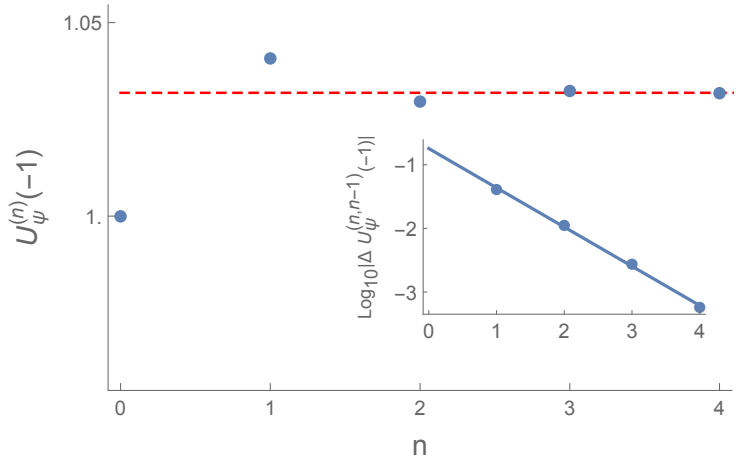

Figure 3.15: Wavefront values $U_\psi^{(n)}(-1)$ at $z = -1$ versus n for the Fisher equation (3.39). The numerically exact value (red, dashed line) is also shown. **Inset:** A $\log_{10}$ semi-log plot of the increments $|\Delta U_\psi^{(n,n-1)}(-1)|$ of the approximants versus n, and a linear fit. Parameter values are $k = 1/4$ and $K/k = 1/2$.

Chapter 4

Fractional differential equations

We briefly elucidate the BLUES function method for the case in which the order of the derivatives can take any value in the set of real numbers. This is called a fractional differential equation (FDE). We study a particular FDE originating in the study of the heat transfer of a semi-infinite rod with Stefan-Boltzmann cooling and perform a comparison with the ADM.

This chapter is based on the article *"BLUES iteration applied to nonlinear ordinary differential equations for wave propagation and heat transfer"* [33], which appeared in *Journal of Physics A: Mathematical and Theoretical*.

4.1 Fractional heat transfer equation

In this section we consider the following nonlinear fractional differential equation (FDE) defined on the semi-infinite real line $t \in (0, \infty)$ with differential order $0 < \alpha \leq 1$ and exponent $n \geq 1$ and with initial condition $U(0) = C_0$, where $C_0 \geq 0$,

$$\mathcal{N}_t U(t) = D_t^\alpha U(t) + U^n(t) = \psi(t)\,, \tag{4.1}$$

where D_t^α is the Riemann- Liouville fractional derivative defined as follows, for $\alpha > 0$ and $t > 0$

$$D_t^\alpha f(t) \equiv \begin{cases} \dfrac{1}{\Gamma(m-\alpha)} \dfrac{d^m}{dt^m} \displaystyle\int_0^t \frac{f(\tau)}{(t-\tau)^{\alpha+1-m}} \mathrm{d}\tau & m-1 < \alpha < m \in \mathbb{N} \\ \dfrac{d^m}{dt^m} f(t) & \alpha = m \in \mathbb{N} \end{cases} \tag{4.2}$$

where $\Gamma(.)$ is the gamma function. This equation has previously been studied in the context of nonlinear heat transfer for the case $\alpha = 1/2$, $C_0 = 0$ and $n = 4$ (Stefan-Boltzmann cooling) [41, 42]. The calculations that follow are valid for all values of $0 < \alpha \leq 1$ and $n \geq 1$. It has been shown that if $\psi(t)$ is a piecewise continuous bounded function, equation (4.1) is guaranteed to have a unique solution. If $\psi(t)$ is nondecreasing in an interval $0 < t < s$, $s \in (0, \infty)$ then the solution is also nondecreasing in that interval [43, 44]. Note that the differential order can in principle be higher than $\alpha = 1$. One can then separate the order $\alpha = m + \beta$ in an integer part $m \in \mathbb{N}$ corresponding to a regular integer-order differential operator, and a fractional part $0 < \beta \leq 1$ which again corresponds to a fractional differential operator. The FDE (4.1) should consequently be supplemented with additional boundary conditions up to a number $m + 1$. In the remainder of this chapter, we will assume $0 < \alpha \leq 1$.

Following the steps in the BLUES procedure outlined in Section 2.1, we now choose the associated linear differential equation by simply dropping the nonlinear $U^n(t)$ term. Once again we write the resulting FDE in operator form

$$\mathcal{L}_t U(t) = D_t^\alpha U(t) = \psi(t)\,, \tag{4.3}$$

with the initial condition chosen to be $U(0) = 0$. The Green function for equation (4.3) can now be calculated by considering a Dirac delta function source instead of $\psi(t)$

$$D_t^\alpha G(t, t') = \delta(t - t')\,, \tag{4.4}$$

where $t - t' > 0$ because the problem is formulated on the semi-infinite real line. This Green function is readily calculated to be

$$G(t, t') = \frac{(t-t')^{\alpha-1}}{\Gamma(\alpha)} \tag{4.5}$$

Consequently the solution of the linear FDE (4.3) is the convolution integral of the Green function (4.5) and the source $\psi(t)$, which we will choose from now on to be the constant function $\psi(t) = 1$ for $t \geq 0$, as was done in references [42, 41]

$$U^{(0)}(t) = \int_0^t G(t, t')\psi(t')\mathrm{d}t' = \frac{1}{\Gamma(\alpha)} \int_0^t (t-t')^{\alpha-1} \mathrm{d}t' = \frac{t^\alpha}{\alpha\Gamma(\alpha)} \tag{4.6}$$

It is worth emphasising that this application to heat transfer is fundamentally different from the previously considered ones in that the source is not assumed to be originating from a disturbance that is "co-moving" with the solution. The variable here is time and not a co-moving coordinate, and the source arises as a natural physical ingredient of the problem. Therefore this example constitutes a non-trivial extension of the domain of applicability of the method not only in the type of DE (from DE to FDE) but also in the character and interpretation of the source term in the DE.

The residual operator is the difference between the linear FDE (4.3) and the nonlinear FDE (4.1) and is defined by the action on $U(t)$, i.e.,

$$\mathcal{R}_t U = \mathcal{L}_t U - \mathcal{N}_t U = -U^n \tag{4.7}$$

Now the $p-$th approximant to equation (4.1) can be calculated by using the BLUES iteration sequence (6.53)

$$U^{(p)}(t) = U^{(0)}(t) + \int_0^t G(t,t')\mathcal{R}_{t'}U^{(p-1)}(t')\mathrm{d}t' \tag{4.8}$$

The first approximant to the nonlinear problem can easily be calculated using (4.5), (4.6) and the iteration sequence definition (4.8), with the choice $n = 4$,

$$\begin{aligned} U^{(1)}(t) &= U^{(0)}(t) - \int_0^t \frac{(t-t')^{\alpha-1}}{\Gamma(\alpha)} \frac{t'^{4\alpha}}{\alpha^4\Gamma^4(\alpha)}\mathrm{d}t' \\ &= \frac{1}{\alpha\Gamma(\alpha)}t^\alpha - \frac{\Gamma(1+4\alpha)}{\alpha^4\Gamma^4(\alpha)\Gamma(1+5\alpha)}t^{5\alpha} \end{aligned} \tag{4.9}$$

One can now iterate (4.8) to generate higher approximants to the solution of the nonlinear FDE (4.1). In Fig. 4.1 and Fig. 4.2, the approximants for different values of α are compared with the numerically exact solution.

For the choice $\alpha = 1/2$, equation (4.1) is associated with the heat transfer equations for a semi-infinite solid [44] with external heating $\psi(t)$ and either linear Newton cooling when $n = 1$ or nonlinear Stefan-Boltzmann cooling when $n = 4$. In [44], it was shown that if the condition

$$\int_0^\infty \psi(t')\mathrm{d}t' < \infty \tag{4.10}$$

is fulfilled, for $n \geq 3$, some of the energy entering the solid will persist, while for $n \leq 2$, all energy is eventually radiated away. For the remainder of this work,

we will use the nonlinear Stefan-Boltzmann cooling $n = 4$. The zeroth-, first-, and second approximants for $\alpha = 1/2$ and $n = 4$ are, respectively, given by

$$
\begin{aligned}
U^{(0)}(t) &= 2\left(\frac{t}{\pi}\right)^{1/2} \\
U^{(1)}(t) &= 2\left(\frac{t}{\pi}\right)^{1/2} - \frac{256}{15}\left(\frac{t}{\pi}\right)^{5/2} \\
U^{(2)}(t) &= 2\left(\frac{t}{\pi}\right)^{1/2} - \frac{256}{15}\left(\frac{t}{\pi}\right)^{5/2} + \frac{2097152}{4725}\left(\frac{t}{\pi}\right)^{9/2} \\
&\quad - \frac{1073741824}{225225}\left(\frac{t}{\pi}\right)^{13/2} + \frac{8796093022208}{369208125}\left(\frac{t}{\pi}\right)^{17/2} \\
&\quad - \frac{2251799813685248}{49104680625}\left(\frac{t}{\pi}\right)^{21/2}
\end{aligned}
\tag{4.11}
$$

The approximants obtained by the BLUES function method can be compared to those obtained with the Adomian decomposition method (ADM). This is shown in Fig. 4.3, where the 21st-order approximant for the ADM is shown versus the 5th approximant for the BLUES function method and the numerically exact solution.

The number of nonzero terms $g(i, n)$ for the approximant of iteration $i \in \mathbb{N}$ generated by the BLUES function method can be calculated exactly for a general nonlinearity exponent $n \in \mathbb{N}$, $n \geq 1$, i.e.,

$$
g(i, n) = \begin{cases} \frac{1}{n-1}\left(n - 2 + n^i\right) & n \geq 2 \\ i + 1 & n = 1 \end{cases}
\tag{4.12}
$$

so for $n = 4$, the 4th approximant contains $g(4, 4) = 86$ nonzero terms. Note that the number of terms increases exponentially with the iteration number. In comparison, the ADM generates a series with a number of terms which grows linearly with the order of approximation. Note that the ADM generates the exact coefficients in a series representation of the solution while the BLUES function method generates many more terms but the coefficients are not necessarily already saturated to their exact value. One can say that the BLUES method generates, in each iteration, a (huge) number of scout terms that probe the emerging series expansion and gradually gain precision. The coefficients in the BLUES function method saturate roughly linearly with increasing order of approximation, as can be seen when keeping track of the coefficient a_{17} of the $t^{17/2}$ term. This is first generated in the second approximant $U^{(2)}$ with

a value of $a_{17} = 1.41659$. In the third approximant the value increases to $a_{17} = 19.8026$ and eventually saturates in the fourth approximant, attaining its exact value $a_{17} = 30.8436$, which is the same coefficient as was found with the ADM. The same comparison can be applied to the coefficient a_{21} of the $t^{21/2}$ term. This term is again generated in the second approximant with a value of $a_{21} = -0.27627$ and increases in absolute value to $a_{21} = -40.9762$ in the third iteration, then to $a_{21} = -99.0372$ in the fourth iteration and eventually saturates at $a_{21} = -118.387$ in the fifth iteration, which is the exact result as found by the ADM.

The higher residual functions are shown in Fig. 4.4 together with the residual operator (4.7) applied to the numerically exact solution (red, full line). Note that for this model the residuals are not localized, in contrast to all previous examples. The approximants to the solution of equation (4.1) do not converge to the correct numerical value at $t \to \infty$ precisely because of the divergence of the residual in every iteration. While the approximants diverge for larger values of t, a radius of convergence can still be identified.

With this example we close the discussion on ODEs (regular or fractional) and continue by studying the BLUES function method for PDEs.

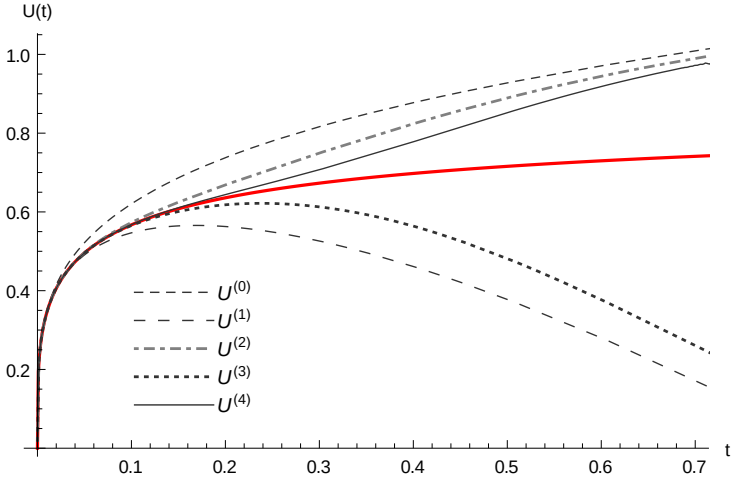

(a)

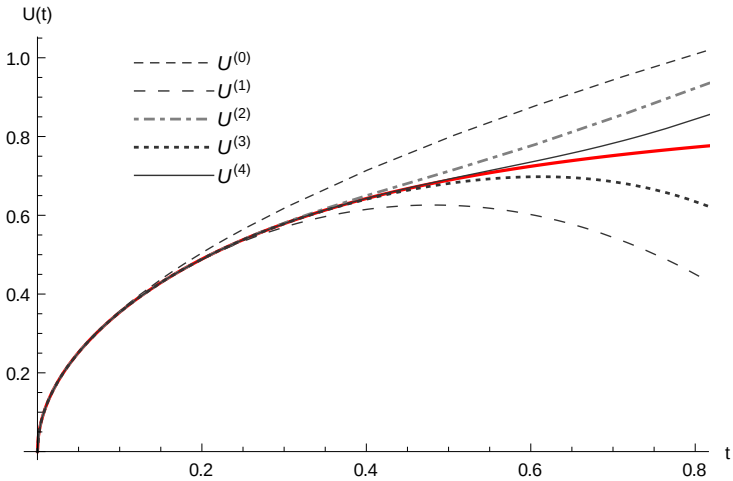

(b)

Figure 4.1: Solution to the nonlinear FDE (4.1) with constant source $\psi(t) = 1$ and fractional order **(a)** $\alpha = 1/4$ and **(b)** $\alpha = 1/2$. The numerical solution (red, full line) is compared with the approximants up to fourth iteration (black/gray lines).

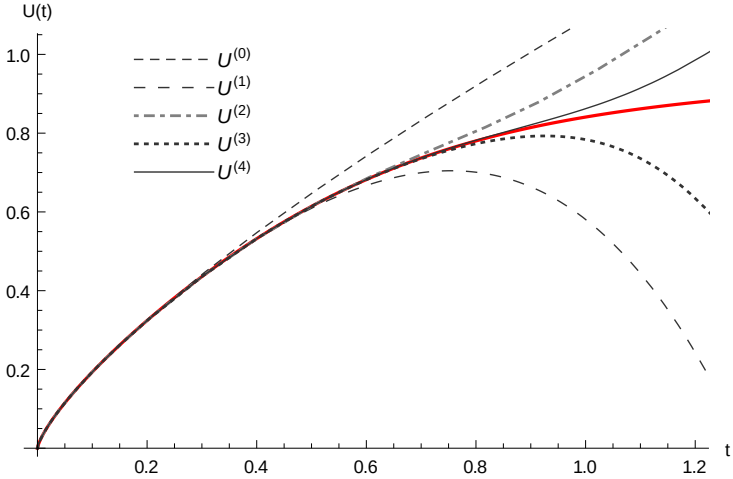

(a)

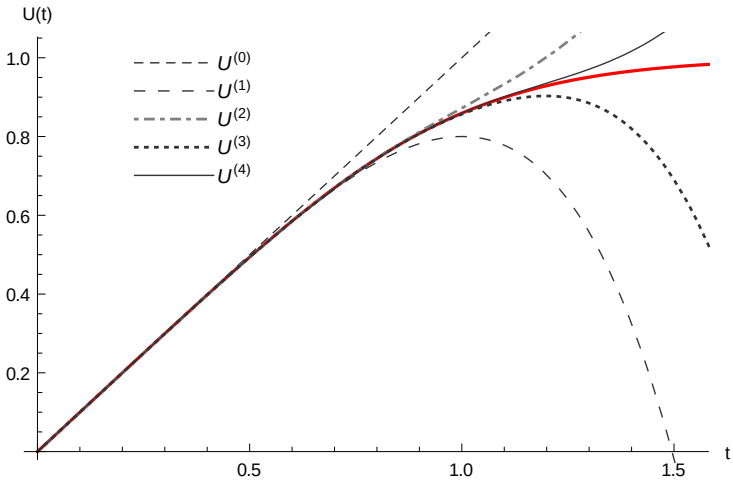

(b)

Figure 4.2: Solution to the nonlinear FDE (4.1) with constant source $\psi(t) = 1$ and fractional order **(a)** $\alpha = 3/4$ and **(b)** $\alpha = 1$. The numerical solution (red, full line) is compared with the approximants up to fourth iteration (black/gray lines).

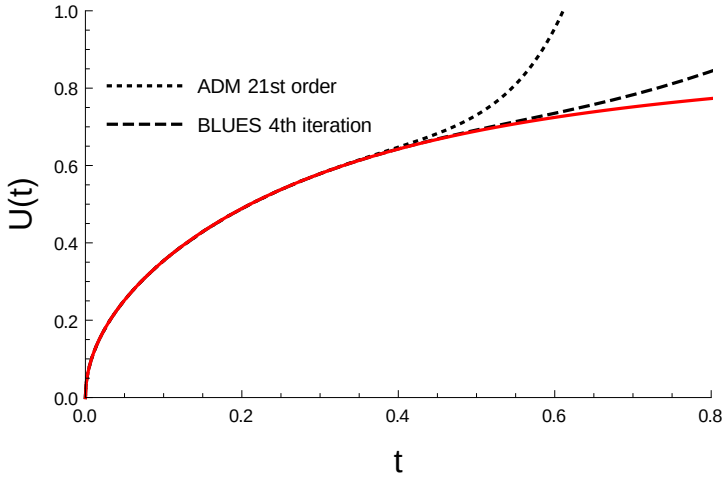

Figure 4.3: Comparison between the 21st iteration of the ADM (dotted line) and the fourth iteration of the BLUES function method (dashed line) for $\alpha = 1/2$ and $n = 4$. The numerically exact solution (red, full line) is also shown.

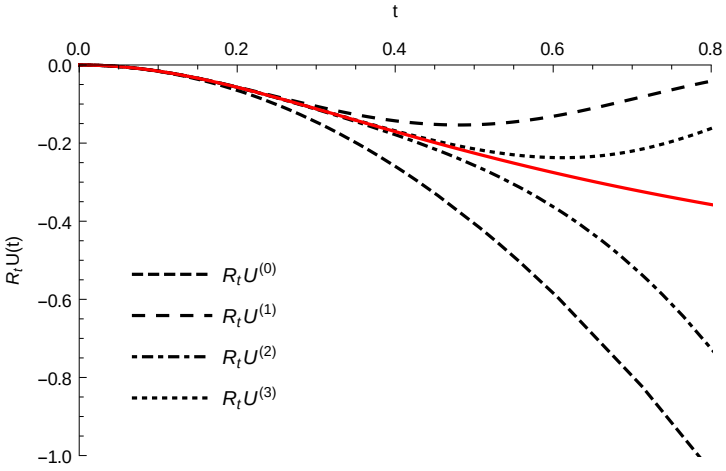

Figure 4.4: Residual $\mathcal{R}_t U(t) = -U^4(t)$ with $\alpha = 1/2$ for different iterations. The numerically exact residual $\mathcal{R}_t U_{\text{num}}$ is also shown (red, full line).

Chapter 5

Partial differential equations

The goal of this chapter is twofold. First we establish the BLUES function method for partial differential equations (PDEs). Second we show that in some cases the BLUES function method outperforms some well-established methods, while in other cases it produces a solution which converges more slowly to the exact solution than other methods. This will first be illustrated for four relatively simple test cases and then the BLUES function method is used to investigate a minimalistic model for the evolution of an interface height profile. In this work, we will compare the BLUES function method to four other established methods: the variational iteration method (VIM) [19], the VIM with Green function (GVIM) [22], the Adomian decomposition method (ADM) [10, 11] and the homotopy perturbation method (HPM) [23]. A brief outline of each of the aforementioned methods can be found in chapter 2.

The setup of this chapter is as follows. In Section 5.1 we will extend the BLUES function method initially described for ODEs in [33, 9, 7] to the arena of partial differential equations. In Sections 5.2, 5.3 and 5.4 we study three simple exactly solvable PDEs and compare the different methods. Next, in Section 5.5 we set the stage for the following section by applying the BLUES function method to a general power-law convective nonlinearity which we consequently use in Section 5.6 to study a minimalistic model for the evolution of interfaces under the combined effects of shear and growth.

This chapter is based on the article *"The BLUES function method applied to partial differential equations and analytic approximants for interface growth under shear"* [45], which was accepted for publication in Physical Review Research.

5.1 The BLUES function method for a nonlinear PDE

Here we extend the BLUES iteration method originally developed for ODEs [7, 9, 33] to PDEs in time and one space variable. The crucial role of the extrinsic *source (or sink) term* in the context of the ODE will now be taken over, simply, by the intrinsic *initial condition* of the solution of the PDE. Consequently, the extension of the method to PDEs entails a conceptual simplification rather than complication, and allows one to increase substantially the range of (physics) problems that can be tackled.

Let us start from a linear PDE which can be written as an operator $\mathcal{L}_{t,x}$ acting on a function $u(x,t)$, say a density subject to diffusion, and let us attempt to solve

$$\mathcal{L}_{t,x}\, u(x,t) = 0, \text{ for } t > 0, \tag{5.1}$$

with initial condition

$$u(x,0) = f(x). \tag{5.2}$$

Since the problem is linear the solution $u(x,t)$ can be written as the convolution $G*f$ of the initial condition $f(x)$ with the Green function $G(x,t)$, which satisfies

$$\mathcal{L}_{t,x}\, G(x,t) = 0, \text{ for } t > 0, \tag{5.3}$$

while meeting the initial condition

$$\lim_{t\to 0} G(x,t) = \delta(x)\,. \tag{5.4}$$

The solution to the linear problem is the (single-variable) convolution, which reads

$$u(x,t) = \int_{\mathbb{R}} dx'\, G(x-x',t) f(x'). \tag{5.5}$$

For simplicity we restrict our attention to PDEs that involve only the first derivative w.r.t. to time, specifically $\mathcal{L}_{t,x}\, u = u_t + \tilde{\mathcal{L}}_x u$, with $u_t \equiv \partial u/\partial t$ and $\tilde{\mathcal{L}}_x$ a time-independent linear operator. For our purposes, it is convenient to rewrite the PDE by invoking the initial condition $f(x)$ through the action of a Dirac-delta source in time. The following time and space integral, which is a two-variable convolution $u(x,t) = G * f\,\delta$, solves the rearranged inhomogeneous linear PDE, which is equivalent to the original linear PDE,

$$\mathcal{L}_{t,x}\, u(x,t) = \mathcal{L}_{t,x} \int_{0^-}^{t} dt' \int_{\mathbb{R}} dx'\, G(x-x',t-t') f(x')\delta(t') = f(x)\delta(t)\,. \tag{5.6}$$

This identity holds by virtue of the fact that $\mathcal{L}_{t,x}$ contains only a first derivative w.r.t. time t. This derivative generates two terms. The boundary term (the

value of the integrand at $t' = t$) exactly produces the right-hand-side of (5.6), in view of (5.4). The second term is contained in the action of $\mathcal{L}_{t,x}$, when it is moved inside the integral over t'. That action is a contribution that vanishes for all $t' < t$ in view of (5.3). Moreover, for all $t' > 0$, including $t' = t$, the contribution is zero in view of the vanishing of the factor $\delta(t')$ present in the integrand. It remains to be checked that the presence of $\delta(t')$ does not spoil our conclusion in the vicinity of $t' = 0$. There we pick up a finite contribution from $\int_{0^-}^{0^+} dt'\, \delta(t') = 1$ but it is multiplied by zero in view of (5.3). We conclude that $G * f\,\delta$ solves the PDE for all $t > 0$.

The initial condition is retrieved by examining carefully the limit $t \to 0$. Firstly, the solution $u(x,t)$ as given by the time and space integral $G * f\,\delta$ obviously vanishes for $t < 0^-$ by definition, so $u(x, t < 0) = 0$. However, this solution "jumps" to the initial condition function $f(x)$ at $t = 0^+$ through the action of $\delta(t')$ and by the fact that the Green function becomes a spatial Dirac-delta in view of (5.4). The space integral then produces $f(x)$. For $t > 0$ the solution evolves, in a continuous manner, from this initial condition.

Using this representation of the PDE, which naturally features an intrinsic source term expressing the initial condition, we can now generalize the BLUES iteration procedure from nonlinear ODEs to nonlinear PDEs. One may add a nonlinearity rather freely to the PDE, while preserving the simple form of the time-dependent part,

$$\mathcal{N}_{t,x}\, u = u_t + \tilde{\mathcal{N}}_x u, \tag{5.7}$$

with $\tilde{\mathcal{N}}_x$ a time-independent nonlinear operator, and arrive at the nonlinear PDE

$$\mathcal{N}_{t,x}\, u(x,t) = 0, \tag{5.8}$$

with initial condition, as before,

$$u(x,0) = f(x). \tag{5.9}$$

The BLUES function method now proposes to construct a solution $u(x,t)$ to the equivalent inhomogeneous PDE in the form of a two-variable convolution $u(x,t) = B * \phi$, so that

$$\mathcal{N}_{t,x}\, u(x,t) = \mathcal{N}_{t,x} \int_{0^-}^{t} dt' \int_{\mathbb{R}} dx'\, B(x - x', t - t')\phi(x', t') = f(x)\delta(t). \tag{5.10}$$

Clearly, this PDE coincides with the original nonlinear PDE (5.8) for $t > 0$ and we will shortly examine its behavior at $t = 0$. The function $B(x,t)$ is called BLUES function and it is taken to be the Green function of an arbitrary but conveniently chosen linear operator $\mathcal{L}_{t,x}$ related to $\mathcal{N}_{t,x}$. The challenge is to calculate the new associated source $\phi(x,t)$ knowing that $B * f\delta$ solves the linear

PDE (5.6) with initial condition $f(x)$ and source term $f\delta$. Note that $\phi(x,t)$ need not be separable and in general it is not.

The initial condition is generated correctly, since, by definition, $u(x,t<0)=0$ and subsequently $u(x,t=0^+)=f(x)$, provided three conditions are fulfilled. The first is that $\mathcal{N}_{t,x}\,u=0$, for $u=0$. The second condition is that the associated source ϕ decomposes as follows into a separable singular term and a (non-separable) smooth term ζ, which is to be calculated analytically: $\phi(x,t)=f(x)\delta(t)+\zeta(x,t)$, with $\int_{0^-}^{0^+} dt\,\zeta(x,t)=0$. The third condition is that for all finite x the function $\tilde{\mathcal{N}}_x f(x)$ be finite. For nonlinear operators these are not obvious and must be checked.

For this calculation one defines a (time-independent) residual operator $\mathcal{R}_x \equiv \mathcal{L}_{t,x}-\mathcal{N}_{t,x}$ and makes use of the implicit identity

$$\mathcal{N}_{t,x}\,(B*\phi)(x,t)=\phi(x,t)-\mathcal{R}_x\,(B*\phi)(x,t)=f(x)\delta(t), \tag{5.11}$$

which follows directly from the Green function property of B w.r.t. the chosen linear PDE.

To obtain the solution to the nonlinear PDE (5.8) with initial condition (5.9), equation (5.11) can be rewritten and iterated,

$$\phi(x,t)=f(x)\delta(t)+\mathcal{R}_x\,(B*\phi)(x,t), \tag{5.12}$$

in order to calculate an approximation in the form of a sequence in powers of the residual $\mathcal{R}_x$. In zeroth iteration,

$$\phi^{(0)}(x,t)=f(x)\delta(t), \tag{5.13}$$

and in nth iteration ($n\geq 1$),

$$\phi^{(n)}(x,t)=f(x)\delta(t)+\mathcal{R}_x\,(B*\phi^{(n-1)})(x,t). \tag{5.14}$$

Consequently, the nth analytical approximant to the solution of the nonlinear PDE is found through the two-variable convolution

$$u^{(n)}(x,t)=\left(B*\phi^{(n)}\right)(x,t)=u^{(0)}(x,t)+(B*\mathcal{R}_x\,u^{(n-1)})(x,t). \tag{5.15}$$

5.2 Reaction-diffusion-convection equation

Let us start with a simple example, in which the convolutions are all of single variable type. Unless otherwise stated the functions, variables and

parameters are reduced (dimensionless). Consider the nonlinear reaction-diffusion-convection PDE [46] which can be used to describe, e.g., the propagation of a chemical of density u through the combined mechanisms of diffusion, nonlinear convection and reaction, with $a \in \mathbb{R}$,

$$\mathcal{N}_{t,x}\, u = u_t - u_{xx} + uu_x + u(u+a) = 0\,, \tag{5.16}$$

defined on $(x,t) \in \mathbb{R} \times [0,\infty)$ with an exponential initial condition, i.e.,

$$u(x,0) = f(x) = \mathrm{e}^{-x}\,. \tag{5.17}$$

This unbounded initial condition is rather unphysical but will serve as an ideal testbed for the comparison of the different approximation methods, as in this case a simple exact solution of (5.16) can be found. We will now consider the methods mentioned in Chapter 2 and compare their results. The ADM, HPM and VIM all produce the following sequence of approximants:

$$\begin{aligned}
u^{(0)}(x,t) &= \mathrm{e}^{-x} \\
u^{(1)}(x,t) &= \mathrm{e}^{-x}\,(1-(a-1)t) \\
u^{(2)}(x,t) &= \mathrm{e}^{-x}\left(1-(a-1)t+\frac{(a-1)^2t^2}{2!}\right) \\
&\;\;\vdots \\
u^{(n)}(x,t) &= \mathrm{e}^{-x}\sum_{i=0}^{n}\frac{(-(a-1)t)^i}{i!}\,,
\end{aligned} \tag{5.18}$$

which converges slowly to the exact solution

$$u(x,t) = \lim_{n\to\infty} u^{(n)}(x,t) = \mathrm{e}^{-(x+(a-1)t)}\,. \tag{5.19}$$

Note that the sequence (5.18) is the Taylor series of the temporal part of the exact solution expanded about $t = 0$ and is therefore only useful for $t < \mathcal{O}(1)$.

The GVIM calculations result in a different sequence of approximants,

$$
\begin{aligned}
u^{(0)}(x,t) &= \mathrm{e}^{-x} \\
u^{(1)}(x,t) &= \frac{\mathrm{e}^{-x}}{a} + \frac{\mathrm{e}^{-at-x}(a-1)}{a} \\
u^{(2)}(x,t) &= \frac{\mathrm{e}^{-x}}{a^2} + \frac{\mathrm{e}^{-at-x}(a^2-1)}{a^2} + \frac{\mathrm{e}^{-at-x}(a-1)}{a}t \\
u^{(3)}(x,t) &= \frac{\mathrm{e}^{-x}}{a^3} + \frac{\mathrm{e}^{-at-x}(a^3-1)}{a^3} + \frac{\mathrm{e}^{-at-x}(a^2-1)}{a^2}t + \frac{\mathrm{e}^{-at-x}(a-1)}{2a}t^2 \\
&\vdots \\
u^{(n)}(x,t) &= \frac{\mathrm{e}^{-x}}{a^n} + \mathrm{e}^{-at-x}\sum_{i=0}^{n-1}\frac{(a^{n-i}-1)}{a^{n-i}i!}t^i\,,
\end{aligned}
\tag{5.20}
$$

which converges to the exact solution (5.19) for $n \to \infty$ as well.

We now turn to the BLUES function method, and follow the scheme outlined in Section 5.1. First, the PDE (5.16) with initial condition $f(x)$ is rewritten as follows

$$
\begin{aligned}
\mathcal{N}_{t,x}\,u(x,t) &= u_t(x,t) - u_{xx}(x,t) + u(x,t)u_x(x,t) + u(x,t)(u(x,t)+a) \\
&= f(x)\delta(t)\,,
\end{aligned}
\tag{5.21}
$$

defined on $(x,t) \in \mathbb{R} \times [0,\infty)$ and the initial condition $u(x,0) = f(x) = \mathrm{e}^{-x}$ has been converted to a source term by multiplication with a Dirac-delta function in the temporal coordinate. Choosing the linear operator simple and without spatial derivatives, one can define the associated linear PDE with source $\psi(x,t) \equiv f(x)\delta(t)$ as follows

$$
\mathcal{L}_t\,u(x,t) = u_t(x,t) + au(x,t) = \psi(x,t), \tag{5.22}
$$

which is solved by $u(x,t) = f(x)G(t)$, with $G(t)$ the Green function for $\mathcal{L}_t$. Note that we omitted the linear term u_{xx} from the linear part $\mathcal{L}_{t,x}$ of the operator $\mathcal{N}_{t,x}$. This judicious choice, which is a distinct feature of the BLUES strategy, not only simplifies the calculations but also considerably improves the convergence.

We obtain a step function with exponential tail,

$$
G(t) = \Theta(t)\mathrm{e}^{-at}, \tag{5.23}
$$

and the solution $U(t)$ for the linear problem with arbitrary source $\psi(t)$, for $t > 0$, is

$$U(t) = (G * \psi)(t) = \int_{\mathbb{R}} ds\, G(t-s)\psi(s) = \int_{0^-}^{t} ds\, G(t-s)\psi(s), \tag{5.24}$$

since $G(\tau < 0) = 0$ and $s > 0$.

We next define the residual operator $\mathcal{R}_x$ as the difference between the linear and the nonlinear operator, i.e., $\mathcal{R}_x = \mathcal{L}_t - \mathcal{N}_{t,x}$, so

$$\mathcal{R}_x\, u = u_{xx} - uu_x - u^2\,, \tag{5.25}$$

and set up the iteration sequence based on (5.14) and (5.15) for the solution to (5.21),

$$\begin{aligned} u^{(n+1)}(x,t) &= u^{(0)}(x,t) + (B * \mathcal{R}_x\, u^{(n)})(x,t) \\ &= u^{(0)}(x,t) + \int_{0^-}^{t} \mathrm{d}s\, G(t-s)\mathcal{R}_x\, u^{(n)}(x,s) \\ &= u^{(0)}(x,t) + \int_{0^-}^{t} \mathrm{d}s\, G(t-s)\left[u_{xx}^{(n)} - u^{(n)}u_x^{(n)} - (u^{(n)})^2\right](x,s), \end{aligned} \tag{5.26}$$

where the BLUES function $B(\tau)$ is the Green function $G(\tau)$ of (5.23) for the chosen linear operator $\mathcal{L}_t$, whose action is given in (5.22). The zeroth approximant is the convolution of the BLUES function with the source $\psi(x,t)$,

$$u^{(0)}(x,t) = \int_{0^-}^{t} G(t-s)\psi(x,s)\mathrm{d}s = \mathrm{e}^{-at-x}\,. \tag{5.27}$$

Iterating through the procedure (5.26), one finds the following sequence of approximants

$$\begin{aligned} u^{(0)}(x,t) &= \mathrm{e}^{-at-x} \\ u^{(1)}(x,t) &= \mathrm{e}^{-at-x}(1+t) \\ u^{(2)}(x,t) &= \mathrm{e}^{-at-x}(1+t+\frac{t^2}{2!}) \\ &\vdots \\ u^{(n)}(x,t) &= \mathrm{e}^{-at-x}\sum_{i=0}^{n}\frac{t^i}{i!}\,, \end{aligned} \tag{5.28}$$

which converges to the exact solution (5.19) for $n \to \infty$. Note that each approximant is bounded and useful for all t by virtue of the overall factor e^{-2t}.

We can now compare the results of the three different methods. Since all three methods converge to the known exact solution (5.19), one can define an error function $E^{(n)}(x,t)$ as the absolute value of the difference between the nth approximant and the exact solution $u_{ex}(x,t)$,

$$E^{(n)}(x,t) = \left|u_{ex}(x,t) - u^{(n)}(x,t)\right|. \tag{5.29}$$

In Fig. 5.1, the approximants $u^{(n)}(x,t)$ (left panel) and the errors $E^{(n)}(x,t)$ (right panel) for the different methods are shown for $a=3$, $n=3$ and fixed position $x=1$. One can observe that the error in ADM and VIM becomes very large for values of $t \gg 1$, indicating that the approximants diverge for large t, as expected. The error in the GVIM, however, saturates at a finite value which can be calculated for all values of x as

$$\lim_{t\to\infty} E^{(n)}_{\mathrm{GVIM}}(x,t) = \frac{\mathrm{e}^{-x}}{a^n}\,, \tag{5.30}$$

which for $a=3$, $n=3$ and $x=1$ results in $(27e)^{-1}$. Note that the errors for both the ADM and VIM and for the GVIM are monotonically increasing in time and hence the approximations decrease in accuracy for large values of t. In contrast, for the BLUES function method the error vanishes in the limit $t \to \infty$ and this method provides the fastest convergence for all $t > 0$. The reason for this improved performance is that the *choice of the linear operator part* in the BLUES function method is free and can be tailored so as to render all the approximants well bounded for all times.

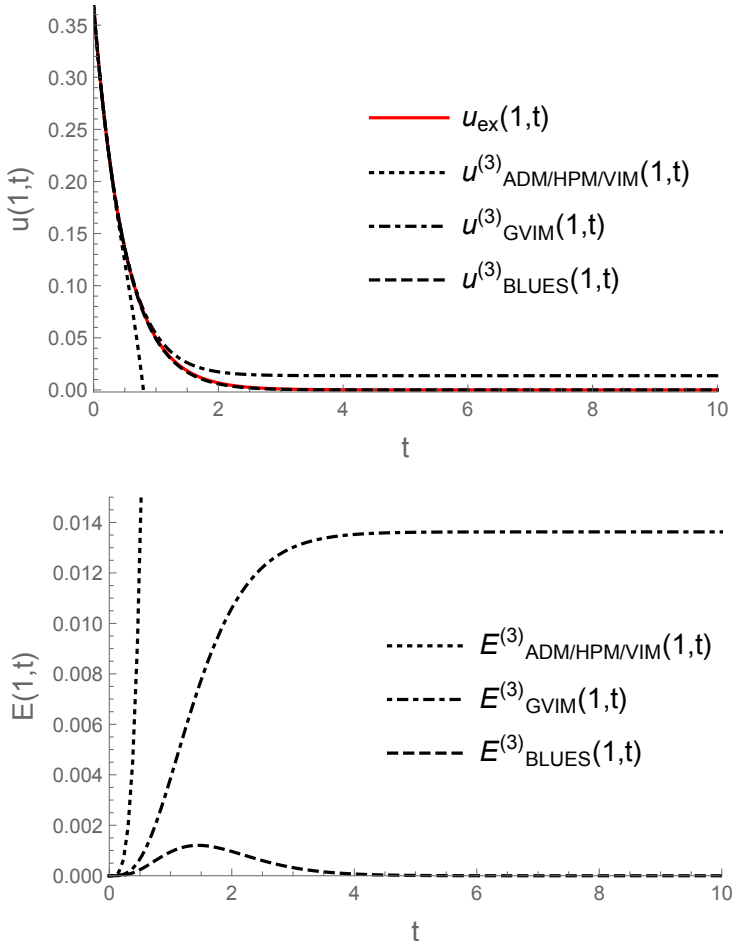

Figure 5.1: The approximants $u^{(3)}(x=1,t)$ and the exact solution (5.19) (upper panel) and the errors $E^{(3)}(x=1,t)$ (lower panel) for the different methods: ADM, HPM and VIM (5.18) (dotted line), GVIM (5.20) (dot-dashed line) and BLUES (5.28) (dashed line). The parameter is $a=3$.

5.3 Nonlinear Black-Scholes equation

For the following example, let us look at the field of economics. Unless otherwise stated the functions, variables and parameters are reduced (dimensionless). The Black-Scholes equation describes the value $V(S,\tau)$ of an option for some underlying asset price $S \in [0,\infty)$ over a period $\tau \in [0,T]$, with T the time

of maturity, that is, the last moment on which an option can be exercised. After expiration or maturity, the option contract will cease to exist and the buyer cannot exercise their right to buy or sell. The underlying asset price S is a stochastic variable and follows a geometric Brownian motion. In [47], the authors consider a nonlinear Black-Scholes PDE for $V(S,\tau)$, which assumes that the market is incomplete through the combined feedback effects of illiquid markets and large trader effects. In this PDE S is treated as a continuous variable, which we name s, and s and τ are treated as independent variables. This PDE is the following,

$$u_t + \frac{\sigma^2 s^2}{2} u_{ss}\,(1 + 2\rho\, s\, u_{ss}) + rs\, u_s - ru = 0\,, \tag{5.31}$$

with t the time until expiry, $t = T - \tau$, u the value function, $u(s,t) \equiv V(S,\tau)$, σ the volatility, r the risk-free interest rate. The constant ρ is a measure of the liquidity of the market. In order to ensure that feedback effects from hedging generate so-called *volatility smiles*, one has to choose this liquidity parameter to be negative [48, 49]. We consider the initial condition $u(s,0) = f(s) = s - \sqrt{sS_0}/\rho - S_0/(4\rho)$, where $S_0 \equiv S(\tau = 0)$ is the starting price of the asset.

In [50], the authors study the solution of (5.31) by means of the ADM. This gives the following sequence of component functions of the solution,

$$\begin{aligned}
u_0(s,t) &= s - \frac{\sqrt{sS_0}}{\rho} - \frac{S_0}{4\rho} \\
u_1(s,t) &= -\frac{(4r+\sigma^2)}{8\rho}\left(\frac{S_0}{2} + \sqrt{sS_0}\right) t \\
u_2(s,t) &= -\frac{(4r+\sigma^2)^2}{128\rho}\left(S_0 + \sqrt{sS_0}\right) t^2 \\
&\vdots
\end{aligned} \tag{5.32}$$

The solution is the sum of all the component functions $u_i(s,t)$,

$$u_{\mathrm{ADM}}(s,t) = \sum_{i=0}^{\infty} u_i(s,t)\,. \tag{5.33}$$

This claim can easily be verified by noticing that the component functions $u_i(s,t)$ are the coefficients of the Taylor series of the exact solution [47],

$$u(s,t) = s - \frac{\sqrt{S_0}}{\rho}\left(\sqrt{s}\,\mathrm{e}^{(r+\frac{\sigma^2}{4})t/2} + \frac{\sqrt{S_0}}{4}\,\mathrm{e}^{(r+\frac{\sigma^2}{4})t}\right). \tag{5.34}$$

The HPM results in exactly the same sequence of solutions as (5.32). The VIM produces the following sequence of approximants to the solution of (5.31),

$$
\begin{aligned}
u^{(0)}(s,t) &= s - \frac{\sqrt{sS_0}}{\rho} - \frac{S_0}{4\rho} \\
u^{(1)}(s,t) &= s - \frac{\sqrt{sS_0}}{\rho} - \frac{S_0}{4\rho} - \frac{(4r+\sigma^2)}{8\rho}\left(\frac{S_0}{2} + \sqrt{sS_0}\right) t \\
u^{(2)}(s,t) &= s - \frac{\sqrt{sS_0}}{\rho} - \frac{S_0}{4\rho} - \frac{(4r+\sigma^2)}{8\rho}\left(\frac{S_0}{2} + \sqrt{sS_0}\right) t \\
&\quad - \frac{(4r+\sigma^2)^2}{64\rho}\left(S_0 + \sqrt{sS_0}\right)\frac{t^2}{2!} - \frac{(4r+\sigma^2)^2}{512\rho}\left(\sigma^2 S_0\right)\frac{t^3}{3!} \\
&\vdots
\end{aligned}
\tag{5.35}
$$

which converges slowly to the exact solution (5.34).

Next, the GVIM produces the following iterates

$$
\begin{aligned}
u^{(0)}(s,t) &= s - \frac{\sqrt{sS_0}}{\rho} - \frac{S_0}{4\rho} \\
u^{(1)}(s,t) &= s - \frac{1}{8r\rho}\left(\frac{S_0}{2} + \sqrt{sS_0}\right)\left(\mathrm{e}^{-rt}(4r+\sigma^2) - \sigma^2\right) - \frac{\sqrt{sS_0}}{2\rho} \\
u^{(2)}(s,t) &= s - \frac{1}{4\rho}\left(1 - \frac{\sigma^2}{2r} + \frac{\sigma^4}{16r^2}\right)\left(\sqrt{sS_0} - \frac{S_0\sigma^2}{16r}\right) - \frac{S_0(4r+\sigma^3)^2}{1024r^3\rho}\mathrm{e}^{2rt} \\
&\quad - \frac{4r+\sigma^2}{64r^2\rho}\left((4r-\sigma^2)(S_0 + \sqrt{sS_0}) + 8r\sqrt{sS_0}\right)\mathrm{e}^{rt} \\
&\quad + \frac{16r^2-\sigma^4}{512r^2\rho}\left(8r\sqrt{sS_0} - \sigma^2 S_0\right) t\mathrm{e}^{rt} \\
&\vdots
\end{aligned}
\tag{5.36}
$$

Finally, we study the BLUES method. As usual, we first rewrite equation (5.31) with the inclusion of a source $\psi(s,t) = f(s)\delta(t)$, i.e.,

$$
u_t + \frac{\sigma^2 s^2}{2} u_{ss}\left(1 + 2\rho\, s\, u_{ss}\right) + rs\, u_s - ru = \psi\,, \tag{5.37}
$$

and consider the associated linear operator we have used in the previous examples together with the source $\psi(s,t)$, i.e.,

$$\mathcal{L}_t\, u = u_t - ru = \psi\,, \tag{5.38}$$

with Green function,

$$G(t) = \Theta(t)\mathrm{e}^{rt}\,. \tag{5.39}$$

Note that in this example, the linear operator is chosen judiciously by not only dropping the nonlinear term but some linear terms as well. Hence, the residual, whose action is defined through

$$\mathcal{R}_s\, u = -\frac{\sigma^2 s^2}{2} u_{ss}\,(1 + 2\rho\, s\, u_{ss}) - rs\, u_s, \tag{5.40}$$

still contains two linear terms. The zeroth approximant is the convolution of the BLUES function (5.39) and the source $\psi(s,t)$,

$$u^{(0)}(s,t) = \int_{0^-}^{t} \mathrm{d}t'\, G(t-t')\psi(s,t') = \left(s - \sqrt{sS_0}/\rho - S_0/(4\rho)\right)\mathrm{e}^{rt}\,. \tag{5.41}$$

The BLUES function method generates the following sequence of approximants

$$\begin{aligned}
u^{(0)}(s,t) &= \left(s - \frac{\sqrt{sS_0}}{\rho} - \frac{S_0}{4\rho}\right)\mathrm{e}^{rt}\\
u^{(1)}(s,t) &= \left(s - \frac{\sqrt{sS_0}}{\rho} - \frac{S_0(4r+\sigma^2)}{16r\rho}\right)\mathrm{e}^{rt} - \left(rs - \frac{(4r-\sigma^2)}{8\rho}\sqrt{sS_0}\right)\mathrm{e}^{rt}t\\
&\quad - \frac{\sigma^2 S_0}{16r\rho}\mathrm{e}^{2rt}\\
u^{(2)}(s,t) &= \left(s - \frac{\sqrt{sS_0}}{\rho} - \frac{S_0\left(4r-\sigma^2\right)^2(8r-\sigma^2)}{512r\rho^3}\right)\mathrm{e}^{rt}\\
&\quad - \left(rs - \frac{(4r-\sigma^2)}{8\rho}\sqrt{sS_0}\right)\mathrm{e}^{rt}t + \left(r^2 s - \frac{(4r-\sigma^2)^2}{64\rho}\sqrt{sS_0}\right)\frac{\mathrm{e}^{rt}t^2}{2}\\
&\quad - S_0\left(\frac{80r^2\sigma^2 - 16r\sigma^4 + \sigma^6}{512r^3\rho}\right)\mathrm{e}^{2rt} + S_0\left(\frac{48r^2\sigma^2 - 16r\sigma^4 + \sigma^6}{512r^2\rho}\right)\mathrm{e}^{2rt}t\\
&\quad - S_0\left(\frac{\sigma^2(4r-\sigma^2)^2}{512r\rho}\right)\frac{\mathrm{e}^{2rt}t^2}{2}\\
&\quad \vdots
\end{aligned} \tag{5.42}$$

In Fig. 5.2 we compare the results from each of the above methods and also compare their errors, at the level of the 3rd approximant or 3rd order ($n = 3$). Note that we have not chosen an explicit value for the expiration time T and

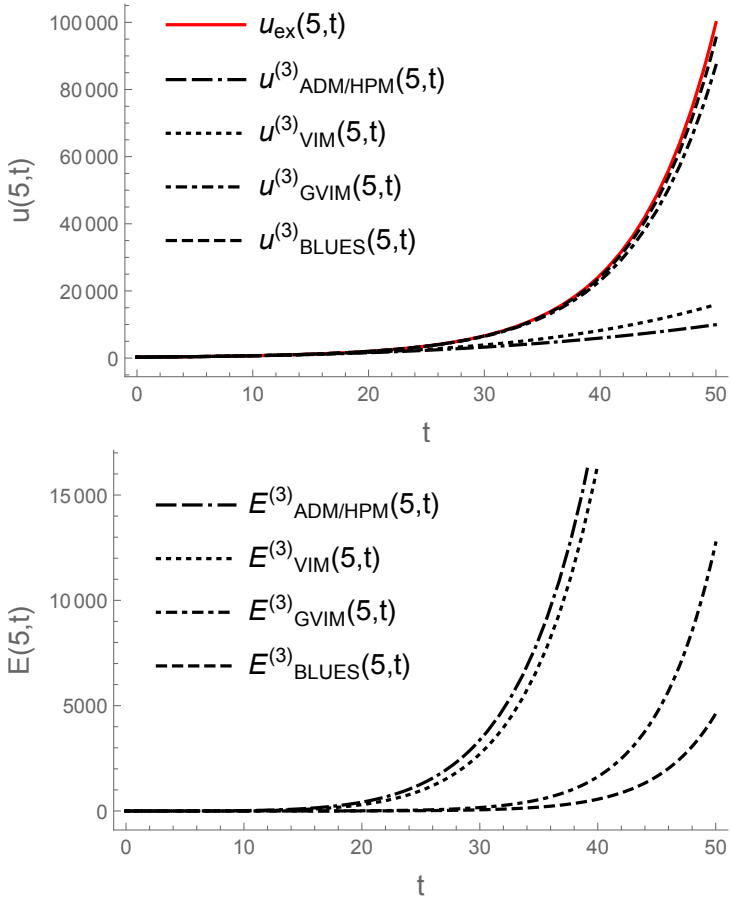

Figure 5.2: Exact solution $u_{ex}(5,t)$ and approximants $u^{(3)}(5,t)$ in third iteration or third order (upper panel). Difference $E^{(3)}(5,t)$ (lower panel) between the exact solution (5.34) and the approximant of order $n = 3$ for the different methods: ADM (5.32) and HPM (dot-dash-dashed line), VIM (5.35) (dotted line), GVIM (5.36) (dot-dashed line), BLUES (5.42) (dashed line). The asset price coordinate is fixed at $s = 5$. Reduced (dimensionless) values of the parameters are $r = 0.06$, $\sigma = 0.6$, $\rho = -0.02$ and $S_0 = 4$.

considered $t \in [0, \infty)$, i.e., $T \to \infty$. If one were to fix $T > 0$ at a finite value, it is obvious that the accuracy of the approximate solutions for all of the above

procedures decreases for $t \to T$, i.e., for increasing remaining time until end of contract.

5.4 Porous medium equation with growth or decay

The final example is in the realm of fluid mechanics: the nonlinear porous medium equation [51] with linear growth or decay,

$$w_t - \Delta(w^m) - \beta w = 0, \tag{5.43}$$

with $m > 1$ and $\beta \in \mathbb{R}$. We consider a density $w(x,t)$ in one space dimension with initial condition $w(x,0) = f(x) = x$. Unless otherwise stated the functions, variables and parameters are reduced (dimensionless). We will only consider a quadratic nonlinearity, $m = 2$, which allows us to write (5.43) as follows

$$w_t - 2ww_{xx} - 2w_x^2 - \beta w = 0\,. \tag{5.44}$$

The components of the solution generated by the ADM are

$$\begin{aligned}
w_0(x,t) &= x \\
w_1(x,t) &= 2t + \beta x t \\
w_2(x,t) &= 3\beta t^2 + \beta^2 x \frac{t^2}{2} \\
w_3(x,t) &= \frac{7\beta^2 t^3}{3} + \beta^3 x \frac{t^3}{6} \\
&\vdots \\
w_i(x,t) &= \frac{2(2^i - 1)\beta^{i-1} t^i}{i!} + x\frac{\beta^i t^i}{i!}\,,
\end{aligned} \tag{5.45}$$

for $i \geq 1$. The nth-order approximant is the partial sum of the component functions w_i, i.e.,

$$w_{\mathrm{ADM}}^{(n)}(x,t) = \sum_{i=0}^{n} w_i(x,t)\,, \tag{5.46}$$

and in the limit $n \to \infty$ this converges to the exact solution

$$w(x,t) = \lim_{n\to\infty} w^{(n)}(x,t) = (x - \frac{2}{\beta})\mathrm{e}^{\beta t} + \frac{2}{\beta}\mathrm{e}^{2\beta t}\,, \tag{5.47}$$

where the sign of β indicates whether there is growth or decay. Note that the ADM generates term by term the exact coefficients of the powers of t in the Taylor expansion in time of the solution. The HPM generates the same sequence of solutions.

The VIM produces the following sequence of approximants to the solution of (5.44),

$$\begin{aligned}
w^{(0)}(x,t) &= x \\
w^{(1)}(x,t) &= 2t + x + \beta x t \\
w^{(2)}(x,t) &= 2t + 3\beta t^2 + \frac{2\beta^2 t^3}{3} + x\left(1 + \beta t + \frac{\beta^2 t^2}{2}\right) \\
w^{(3)}(x,t) &= 2t + 3\beta t^2 + \frac{7\beta^2 t^3}{3} + \frac{2\beta^3 t^4}{3} + \frac{\beta^4 t^5}{10} + x\left(1 + \beta t + \frac{\beta^2 t^2}{2} + \frac{\beta^3 t^3}{6}\right) \\
&\vdots
\end{aligned} \tag{5.48}$$

which also converges to the exact solution (5.47). Note that VIM and ADM produce different results. The VIM does not immediately give the exact coefficients but recursively adjusts them until they saturate at the exact value.

Next, the GVIM produces the sequence

$$\begin{aligned}
w^{(0)}(x,t) &= x \\
w^{(1)}(x,t) &= xe^{\beta t} - \frac{2}{\beta} + \frac{2e^{\beta t}}{\beta} \\
w^{(2)}(x,t) &= x\mathrm{e}^{\beta t} - \frac{2}{\beta}\mathrm{e}^{\beta t} + \frac{2}{\beta}\mathrm{e}^{2\beta t} \\
&\vdots \\
w^{(n)}(x,t) &= x\mathrm{e}^{\beta t} - \frac{2}{\beta}\mathrm{e}^{\beta t} + \frac{2}{\beta}\mathrm{e}^{2\beta t}\,.
\end{aligned} \tag{5.49}$$

For $n \geq 2$, the approximants (5.49) are invariable. The GVIM in this case produces the exact solution (5.47) already in the second iteration and contributions from higher iterations are zero.

We now turn to the BLUES function method. The PDE (5.43) with initial condition $w(x,0) = f(x)$ can be rewritten as a nonlinear PDE with a source $\psi(x,t) = f(x)\delta(t)$,

$$\mathcal{N}_{t,x}\, w(x,t) = w_t(x,t) - (w^m(x,t))_{xx} - \beta w(x,t) = \psi(x,t)\,, \tag{5.50}$$

defined on $(x,t) \in \mathbb{R} \times [0,\infty)$. Choosing the linear operator to be of the same form as the successful one used in the previous section, one can define the associated linear PDE with the same source term,

$$\mathcal{L}_t\, w(x,t) = w_t(x,t) - \beta w(x,t) = \psi(x,t) \tag{5.51}$$

and we recall the Green function for this linear operator,

$$G(t) = \Theta(t)\mathrm{e}^{\beta t}\,. \tag{5.52}$$

Note that in this case the linear operator is chosen by simply dropping (only) the nonlinear term in $\mathcal{N}_{t,x}$. We now obtain the residual operator $\mathcal{R}_x$, which acts as follows on the function w,

$$\mathcal{R}_x\, w = (w^m)_{xx} \tag{5.53}$$

and set up the iteration sequence for the solution to (5.50)

$$\begin{aligned} w^{(n+1)}(x,t) &= w^{(0)}(x,t) + (B * \mathcal{R}_x\, w^{(n)})(x,t) \\ &= w^{(0)}(x,t) + \int_{0^-}^{t} \mathrm{d}s\, G(t-s)\mathcal{R}_x\, w^{(n)}(x,s) \\ &= w^{(0)}(x,t) + \int_{0^-}^{t} \mathrm{d}s\, G(t-s)(w^{(n)})^m_{xx}(x,s), \end{aligned} \tag{5.54}$$

where the BLUES function $B(\tau)$ is the Green function $G(\tau)$ of (5.52) for the chosen linear operator $\mathcal{L}_t$, whose action is given in (5.51). The zeroth approximant is the convolution of the BLUES function and the source $\psi(x,t)$, i.e.,

$$w^{(0)}(x,t) = \int_{0^-}^{t} \mathrm{d}s\, G(t-s)\psi(x,s) = x\,\mathrm{e}^{\beta t}\,. \tag{5.55}$$

Iterating further according to the procedure (5.54), one finds the following sequence of approximants for $m = 2$

$$\begin{aligned} w^{(0)}(x,t) &= x\mathrm{e}^{\beta t} \\ w^{(1)}(x,t) &= x\mathrm{e}^{\beta t} - \frac{2}{\beta}\mathrm{e}^{\beta t} + \frac{2}{\beta}\mathrm{e}^{2\beta t} \\ &\vdots \\ w^{(n)}(x,t) &= x\mathrm{e}^{\beta t} - \frac{2}{\beta}\mathrm{e}^{\beta t} + \frac{2}{\beta}\mathrm{e}^{2\beta t}\,, \end{aligned} \tag{5.56}$$

which, remarkably, produces the exact solution (5.47) to (5.43) already in the first iteration. Higher iterations remain at this "fixed point". In Fig. 5.3 we compare the results from each of the above methods and also compare their errors, at the level of the second iteration, where both the BLUES function method and the GVIM have reached the exact solution.

5.5 Diffusion equation with general nonlinearity

We now set the stage for the analysis of a simple physical model for the evolution of interfaces by first considering a more general example from a technical viewpoint. The heat equation with diffusion constant $D > 0$ and general nonlinearity $u^m u_x^n$, where $m, n \geq 0$ is given by the PDE,

$$\mathcal{N}_{t,x}\, u = u_t - D u_{xx} - u^m u_x^n = 0, \tag{5.57}$$

with Gaussian initial condition $u(x,0) = f(x)$,

$$f(x) = \frac{\mathrm{e}^{-x^2/2\sigma^2}}{\sqrt{2\pi\sigma^2}} \tag{5.58}$$

and boundary conditions $u(|x| \to \infty, t) = 0$. As before, we adopt the notation $\mathcal{N}_{t,x}\, u$ to denote the nonlinear operator acting on $u(x,t)$. The associated linear PDE of our choice is the one-dimensional heat equation describing normal diffusion,

$$\mathcal{L}_{t,x}\, u = u_t - D u_{xx} = 0, \tag{5.59}$$

with the same initial condition and the same boundary conditions. This linear PDE has Green function

$$G(x,t) = \frac{\mathrm{e}^{-\frac{x^2}{4Dt}}}{\sqrt{4\pi D t}}. \tag{5.60}$$

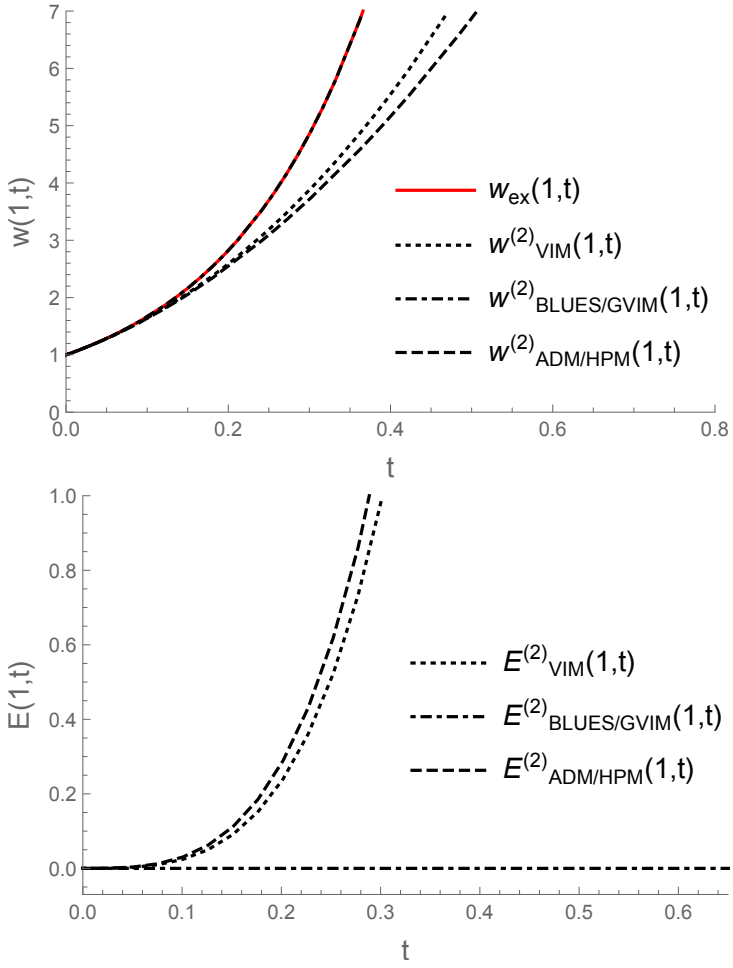

Figure 5.3: Exact solution $w_{\rm ex}(1,t)$ and approximants $w^{(2)}(1,t)$ in second iteration or second order (upper panel). Note that the ADM and HPM, and the BLUES method and GVIM give identical results at this order $n = 2$, respectively. The BLUES/GVIM approximant is exact. Difference $E^{(2)}(1,t)$ (lower panel) between the exact solution (5.47) and the approximant of order $n = 2$ for the different methods: VIM (5.48) (dotted line), BLUES and GVIM (5.56) (dot-dashed line) and ADM and HPM (5.45) (dashed line). The position in space is fixed at $x = 1$ and $\beta = 3$.

In the small time limit $t \to 0$, the Green function (5.60) approaches a Dirac-delta distribution $\delta(x)$. The solution to the diffusion equation with the Gaussian

initial condition $f(x)$ can be calculated by convoluting $f(x)\delta(t)$ with the kernel $G(x,t)$,

$$u^{(0)}(x,t) = \int_{0^-}^{t} \int_{\mathbb{R}} \mathrm{d}y\, \mathrm{d}s\, G(x-y, t-s) f(y)\delta(s). \tag{5.61}$$

Integrating over time and space gives

$$u^{(0)}(x,t) = \int_{\mathbb{R}} \mathrm{d}y\, G(x-y,t) f(y) = \frac{\mathrm{e}^{-x^2/2\Sigma^2(t)}}{\sqrt{2\pi\Sigma^2(t)}}\,, \tag{5.62}$$

which is itself a decaying Gaussian with mean zero and with variance $\Sigma^2(t) \equiv \sigma^2 + 2Dt$. This solution $u^{(0)}$ serves as the zeroth iteration in the BLUES scheme. One now considers the residual operator $\mathcal{R}_x = \mathcal{L}_{t,x} - \mathcal{N}_{t,x}$ which can be applied to the zeroth approximant (5.62),

$$\mathcal{R}_x\, u^{(0)}(x,t) = \left(u^{(0)}(x,t)\right)^m \left(u_x^{(0)}(x,t)\right)^n = (-1)^n \frac{x^n \mathrm{e}^{-(m+n)x^2/2\Sigma^2(t)}}{(2\pi)^{\frac{m+n}{2}} \Sigma(t)^{m+3n}}\,. \tag{5.63}$$

Convoluting the previous expression with the Green function (5.60) results in the correction

$$\begin{aligned}\Delta u^{(1,0)}(x,t) &= u^{(1)}(x,t) - u^{(0)}(x,t) \\ &= \frac{(-1)^n}{(2\pi)^{\frac{m+n+1}{2}}} \int_{0^-}^{t} \mathrm{d}s \frac{\mathrm{e}^{-x^2/2S^2(t,s)}}{\sqrt{2D(t-s)}\Sigma(s)^{m+3n}} \int_{\mathbb{R}} \mathrm{d}y\, y^n \mathrm{e}^{-\alpha(y-cx)^2}\,,\end{aligned} \tag{5.64}$$

where $S^2(t,s) \equiv 2D(t-s) + \Sigma^2(s)/(m+n)$, which can be interpreted as a variance. Further, $c(t,s) \equiv (\Sigma^2(s)/S^2(t,s))/(m+n)$ and $\alpha(t,s) \equiv (m+n)(S^2(t,s)/\Sigma^2(s))/(4D(t-s))$. The spatial integral can be calculated exactly

$$\begin{aligned}\Xi(x,t,s,m,n) &\equiv \int_{\mathbb{R}} \mathrm{d}y\, y^n \mathrm{e}^{-\alpha(t,s)\,(y-c(t,s)\,x)^2} \\ &= \alpha^{-\frac{n+1}{2}} \begin{cases} \Gamma\left(\frac{n+1}{2}\right) {}_1F_1\left(-\frac{n}{2}, \frac{1}{2}, -\alpha c^2 x^2\right), & n \text{ even} \\ n\sqrt{\alpha c^2 x^2}\, \Gamma\left(\frac{n}{2}\right) {}_1F_1\left(-\frac{n-1}{2}, \frac{3}{2}, -\alpha c^2 x^2\right), & n \text{ odd} \end{cases}\end{aligned} \tag{5.65}$$

where $\Gamma(n)$ is the gamma function and ${}_1F_1(a,b,z)$ is the confluent hypergeometric function of the first kind [52]. This spatial integral can equivalently be

expressed in terms of the Hermite polynomials $H_n(z)$ in the following way,

$$\Xi(x,t,s,m,n) \equiv \left(\frac{-i}{2}\right)^n \sqrt{\frac{\pi}{\alpha(t,s)^{n+1}}} H_n\left(i\sqrt{\alpha(t,s)}c(t,s)x\right) . \tag{5.66}$$

We list here the following useful properties for the hypergeometric functions and for the Hermite polynomials:

$$ {}_1F_1(0,b,z) = 1 \tag{5.67}$$

$$ {}_1F_1(-1,b,z) = 1 - \frac{z}{b} \tag{5.68}$$

$$ H_1(z) = 2z \tag{5.69}$$

$$ H_2(z) = 4z^2 - 2\,. \tag{5.70}$$

The first correction to the zeroth approximant (5.62) now becomes

$$\Delta u^{(1,0)}(x,t) = \frac{(-1)^n}{(2\pi)^{\frac{m+n+1}{2}}} \int_{0^-}^{t} \mathrm{d}s\, \frac{\mathrm{e}^{-x^2/2S^2(t,s)}}{\sqrt{2D(t-s)}\Sigma(s)^{m+3n}} \Xi(x,t,s,m,n)\,. \tag{5.71}$$

For some choices of (m,n) this can be simplified greatly. In the next section we discuss a physical system which features two such cases combined, $(m,n) = (1,1)$ and $(m,n) = (0,2)$.

5.6 Interface growth under shear

We propose a minimalistic model for the growth of an interface between two fluids near two-phase coexistence and subject to an externally imposed shear flow. On the one hand, we exploit the finding that the growing interface between a stable and an unstable domain in a kinetic Ising model at low temperature can be described by including in the effective growth equation a Kardar-Parisi-Zhang (KPZ) nonlinearity which allows for lateral growth [3, 53, 4, 54]. On the other hand, we make use of the growth equation proposed for studying interface fluctuations under shear flow, including a Burgers type of nonlinearity [55] which allows for a background linear shear flow imposed on the phase-separated fluid [56, 57]. We combine the two growth equations but limit ourselves to the

minimal setting of two-dimensional systems (i.e., a one-dimensional interface) and the deterministic version of the equation. We ignore thermal noise and postpone an application to the stochastic DE until later work.

Our starting point is, as usual, the Edwards-Wilkinson equation for interface growth [2], which, in its deterministic version, reads

$$h_t - Dh_{xx} = 0\,, \tag{5.72}$$

where $h(x,t)$ is the height of an interface that fluctuates, measured relative to a (horizontal) straight reference line (along x). This reference line is co-moving with the growing interface and therefore a velocity term v is omitted in (5.72). D is a diffusion coefficient (proportional to the interfacial tension whose action is to smoothen the interface).

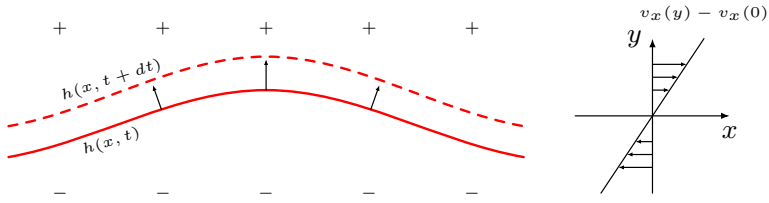

Figure 5.4: Cartoon of a coarse-grained growing interface, a density contour of which is described by a collective coordinate $h(x,t)$, between (stable) "−" and (unstable) "+" domains in the 2d Ising model representation of a phase-separated fluid. **(a)** In the absence of flow the interface advances mainly in the direction normal to its tangent. **(b)** The fluid as a whole is subject to an externally imposed shear flow with linear profile $v_x(y)$.

A cartoon of the physical setting is shown in Fig. 5.4. Following Bray *et al.* [56, 57] we include an externally imposed shear flow. The motivation, in part, for this was that there is an interesting subtle competition between the smoothing of an interface under shear and the roughnening of an interface under thermal noise. Later studies elucidated interface confinement under shear using Monte Carlo simulation [58, 59]. Incorporating a (horizontal) shear velocity profile $v_x(y)$ amounts to invoking the total time derivative,

$$h_t \to \frac{dh}{dt} = h_t + v_x(h)h_x, \tag{5.73}$$

since h is the y-coordinate of the interface position. For shear flow, $v_x(h)$ is a linear function $Ah + B$ and we can choose a reference frame co-moving at the mean velocity, so $B = 0$. We thus add a Burgers convective nonlinearity to the PDE.

Next, following Devillard and Spohn [53] we recognize that the interface growth, ignoring the lattice anisotropies of the model, is in the direction normal to the local tangent. This growth, in which a stable domain overtakes an unstable one, is driven by a pressure difference, or chemical potential difference, with respect to two-phase coexistence (i.e., a non-zero external magnetic field in the Ising model). Incorporating this lateral growth amounts to invoking the KPZ geometric correction,

$$v \to v + \frac{v}{2}(h_x)^2, \tag{5.74}$$

where v is the velocity of the growing interface. Since the term v is already absorbed in (5.72) we need to add only the gradient-squared term to the PDE. Altogether we obtain the nonlinear PDE

$$h_t + Ah\, h_x = Dh_{xx} + \frac{v}{2}h_x^2\,, \tag{5.75}$$

where A is the shear rate.

This PDE combines the Burgers and KPZ nonlinearities but, we recall, ignores thermal noise. When taken separately, each of these two nonlinearities amount to exactly solvable PDEs (through the use of the Cole-Hopf transform), but to our knowledge not when combined. This makes it worthwhile to derive a useful analytical approximant to the solution of the combined equation. Note that in our physical context extra terms proportional to h or h^2 are not present in (5.75) because in the absence of shear flow we require translational invariance of the growth equation along the y-direction. In addition, we require translational invariance along x. Also note that in terms of the scaling properties of interface growth the Burgers term is the dominant perturbation [56, 57] and the KPZ term is subsidiary. We do not discuss these properties here.

There is an alternative route to the PDE (5.75) which is worth pointing out. One may start from the stochastic KPZ equation for interface growth and couple it to the stochastic Navier-Stokes (NS) equation for the velocity field v, by replacing the time derivative in KPZ by the total time derivative, as in (5.73), and invoking the NS equation for v. This system of coupled DEs was proposed and studied in [60]. If, in that system, one ignores the random force in the stochastic NS equation and imposes a (deterministic) shear flow velocity profile, and if one also ignores thermal noise in the KPZ equation, one arrives again at (5.75).

We now proceed to the calculations and adapt the notation slightly in order to be conform with that of previous sections. We define the nonlinear operator, acting on the function $u(x,t)$,

$$\mathcal{N}_{t,x}\, u = u_t - Du_{xx} + \alpha u\, u_x + \beta u_x^2\,, \tag{5.76}$$

with α and β real parameters. For the linear operator $\mathcal{L}_{t,x}$ we choose the entire linear part of $\mathcal{N}_{t,x}$, which is the linear diffusion operator. The residual operator $\mathcal{R}_x$ (cf. Section 5.5), is then defined through

$$\mathcal{R}_x\, u = -\alpha u\, u_x - \beta u_x^2 \tag{5.77}$$

By doing so, the nonlinear problem would be suited to be tackled by *perturbation theory* (PT), if the terms that feature the parameters α and β can be considered to be small compared to the terms of the linear part. This brings us in position to compare the BLUES iteration, which is non-perturbative, to a direct perturbation expansion, keeping in mind that the former makes no assumptions on the magnitude of the nonlinear terms. What we find is akin to our observations in the treatment of ODEs [33]. The BLUES iteration generates a sequence that is in general different from summing up the terms a series expansion, except possibly in the first iteration in which the BLUES result may coincide with that of 1st-order PT.

We consider two different initial conditions, corresponding to distinct physical situations. The first is a single (Gaussian) interface protrusion or "bump", for which we will illustrate the method at the level of the zeroth and first iteration only, and show its close similarity to 1st-order PT. The second one is a (sinusoidal) periodic interface front, for which we will study the time evolution to higher level in the iteration scheme. For that case, we will perform a detailed comparison of the results from ADM, VIM, GVIM, BLUES and PT.

5.6.1 Gaussian initial condition

First, we will consider the situation of a solitary interface bump that can be modeled by a Gaussian initial condition $u(x,0) = f(x)$, given in equation (5.58). We assume the boundary conditions $u(|x| \to \infty) = 0$. The associated linear PDE is the heat equation (3.18). The zeroth approximant is now the decaying Gaussian solution (5.62) of the linear equation. Using equation (5.71) twice, once for the convective nonlinearity (Burgers) and once for the nonlinear lateral growth (KPZ), the first approximant can be calculated analytically. We report here the result (a detailed calculation can be found in Appendix A.3),

$$\begin{aligned} u^{(1)}(x,t) = {} & \frac{\mathrm{e}^{-x^2/2\Sigma^2(t)}}{\sqrt{2\pi\Sigma^2(t)}} + \frac{\beta}{4\pi D}\left[\frac{\mathrm{e}^{-x^2/\Sigma^2(t)}}{\Sigma^2(t)} - \frac{\mathrm{e}^{-x^2/\Sigma^2(2t)}}{\Sigma(2t)\sigma}\right] \\ & + \frac{\alpha}{4D\sqrt{2\pi}}\left[\frac{\mathrm{e}^{-x^2/2\Sigma^2(t)}}{\Sigma(t)}\left(\operatorname{erf}\left(\frac{x}{\sqrt{2}\Sigma(t)}\right) - \operatorname{erf}\left(\frac{\sigma x}{\sqrt{2}\Sigma(t)\Sigma(2t)}\right)\right)\right] \end{aligned} \tag{5.78}$$

Note that the effects introduced by the convective nonlinearity contain only odd functions of x, and the effects introduced by the nonlinear growth contain only even functions of x. In the first iteration the effect of nonlinearity is a simple superposition of the individual nonlinear effects, i.e., nonlinear convection and nonlinear growth. Only in higher iterations does the interplay (mixing) between these different effects take place.

At this level of approximation, the BLUES approximant $u^{(1)}$ coincides with the result of straightforward PT to first order in α and β. This is not surprising in view of the fact that the chosen residual operator coincides with the nonlinear part of the differential operator, which is precisely the "perturbation" when α and β are considered small. We have also performed the ADM and VIM calculations for this case. These methods are, however, not suitable here because they produce large oscillations that grow uncontrollably both in time and in higher orders of approximation. We will return to these methods when we consider a periodic interface undulation.

In the first iteration of the nonlinear problem we obtain,

$$\int_{\mathbb{R}} dx\, u^{(1)}(x,t) = 1 + \frac{\beta}{4D\sqrt{\pi}} \left(\Sigma^{-1}(t) - \sigma^{-1}\right) \tag{5.79}$$

This is a non-decreasing function of time for $\beta < 0$, hence the bump grows as a consequence of the lateral growth correction, even when there is no overall (vertical) growth along y in the co-moving frame. Note that the parameter α does not enter the equation. The shear flow only moves particles along x and does not influence the bump size but only its shape.

In Fig. 5.5 the short-time shift of the bump is illustrated (snapshot at $t = 1/2$), as obtained with zeroth and 1st iteration BLUES as well as zeroth and 1st-order PT, which gives the same results. In Fig. 5.6 the time evolution at fixed position ($x = 2$) is shown, using the zeroth and first BLUES approximants. In both figures the results are compared with the numerically exact solution.

5.6.2 Space-periodic initial condition

For convenience and simplicity, in this example we will work with dimensionless variables x and t, as well as dimensionless u, D, α and β. To study a space-periodic interface contour, we can choose the following trigonometric initial condition $f(x)$

$$f(x) = \sin x \tag{5.80}$$

and examine the behavior of solutions of the suitably rescaled version of equation (5.76) on the real line. The zeroth approximant is the convolution integral of

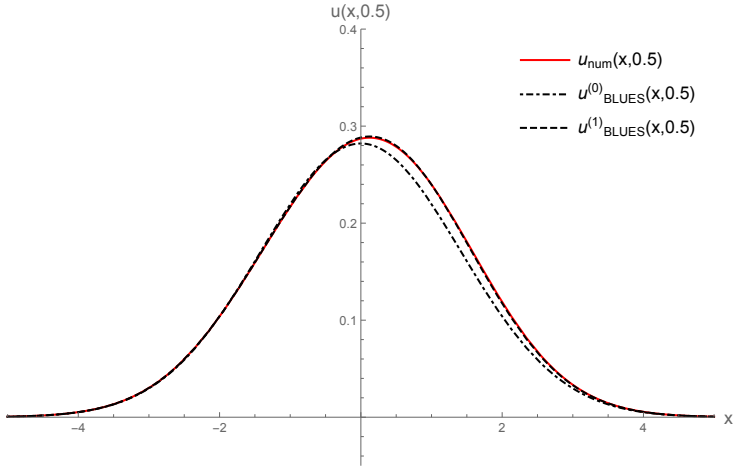

Figure 5.5: Solitary Gaussian height profile at time $t = 1/2$. The numerical solution (red line) is compared with the zeroth (dot-dashed line) and first (dashed line) BLUES approximants (5.78). Reduced (dimensionless) values of the parameters are $D = \sigma = \alpha = 1$ and $\beta = -1$. These results coincide with, respectively, those of standard zeroth and 1st-order PT in the parameters α and β. In the course of time the Gaussian moves to the right (for $\alpha > 0$) and grows somewhat (for $\beta < 0$) until its mass saturates.

the Green function (5.60) with (5.80),

$$u^{(0)}(x,t) = \mathrm{e}^{-Dt} \sin x \,. \tag{5.81}$$

One can now apply the residual operator (5.77) to (5.81). After simplifying the result by using trigonometric power reduction identities, the residual is

$$\mathcal{R}_x \, u^{(0)}(x,t) = -\frac{\mathrm{e}^{-2Dt}}{2} \left(\alpha \sin 2x + \beta \cos 2x + \beta\right) \tag{5.82}$$

The first approximant to the solution of equation (5.76) can be calculated by convoluting the residual (5.82) with the Gaussian Green function, making use of the following identities

$$\begin{aligned} \int_{\mathbb{R}} dy \, \frac{\mathrm{e}^{-\frac{(x-y)^2}{4D(t-s)}}}{\sqrt{4\pi D(t-s)}} \sin ay &= \mathrm{e}^{-a^2 D(t-s)} \sin ax \\ \int_{\mathbb{R}} dy \, \frac{\mathrm{e}^{-\frac{(x-y)^2}{4D(t-s)}}}{\sqrt{4\pi D(t-s)}} \cos ay &= \mathrm{e}^{-a^2 D(t-s)} \cos ax \end{aligned} \tag{5.83}$$

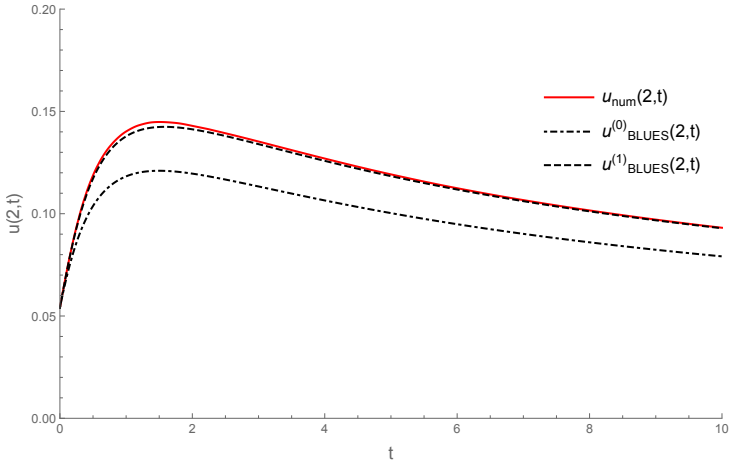

Figure 5.6: Solitary Gaussian time evolution at position $x = 2$. The numerical solution for the height profile u (red line) is compared with the zeroth (dot-dashed line) and first (dashed line) BLUES approximants (5.78). These results coincide with, respectively, those of standard zeroth and 1st-order PT in the parameters α and β. Reduced (dimensionless) values of the parameters are $D = \sigma = \alpha = 1$ and $\beta = -1$.

Hence, the first approximant is

$$u^{(1)}(x,t) = \mathrm{e}^{-Dt}\sin x + \frac{\mathrm{e}^{-2Dt}\left(\mathrm{e}^{-2Dt}-1\right)}{4D}\left[\alpha\sin 2x + \beta\cos 2x + \beta\mathrm{e}^{2Dt}\right] \tag{5.84}$$

Higher approximants can be calculated with moderate effort. In Fig. 5.7 we show the first three BLUES approximants together with the numerically exact solution for a fixed time $t = 1/3$. Next, in Fig.5.8 we compare the numerical solution and the fourth BLUES approximant with the 4th-order VIM and ADM results at $t = 1/3$.

Let us now juxtapose BLUES approximant of the second iteration with a 2nd-order solution obtained from PT. The first(-order) approximants of both methods coincide exactly so we will consider the following perturbation expansion u_{PT} for the solution

$$\begin{aligned} u_{PT}(x,t) = {} & u_{0,0}(x,t) + \alpha u_{1,0}(x,t) + \alpha^2 u_{2,0}(x,t) + \beta u_{0,1}(x,t) \\ & + \beta^2 u_{0,2}(x,t) + \alpha\beta u_{1,1}(x,t) + \mathcal{O}(\alpha^m\beta^n), \quad m+n=3, \end{aligned} \tag{5.85}$$

and we assume, within PT, to avoid ambiguity, that α and β are of the same order of magnitude. Performing the expansion and solving the resulting linear

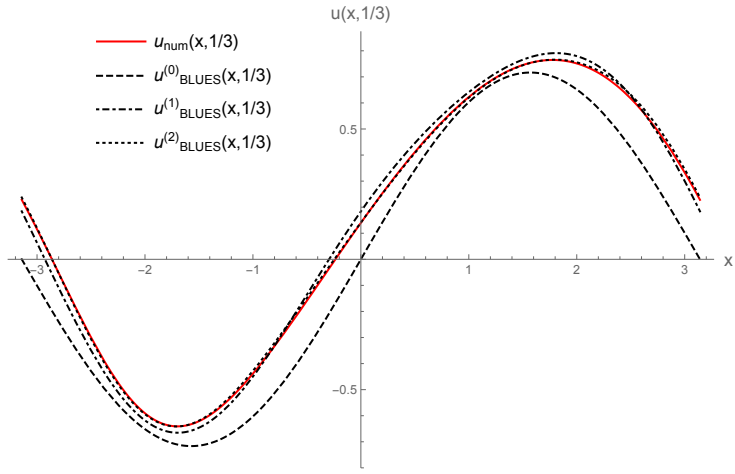

Figure 5.7: Periodic height profile at time $t = 1/3$. The numerical solution (red line) is compared with the $n = 0, 1$ and 2 BLUES approximants. The second approximant nearly coincides with the numerical solution at this resolution. Parameter values are $D = \alpha = 1$ and $\beta = -1$.

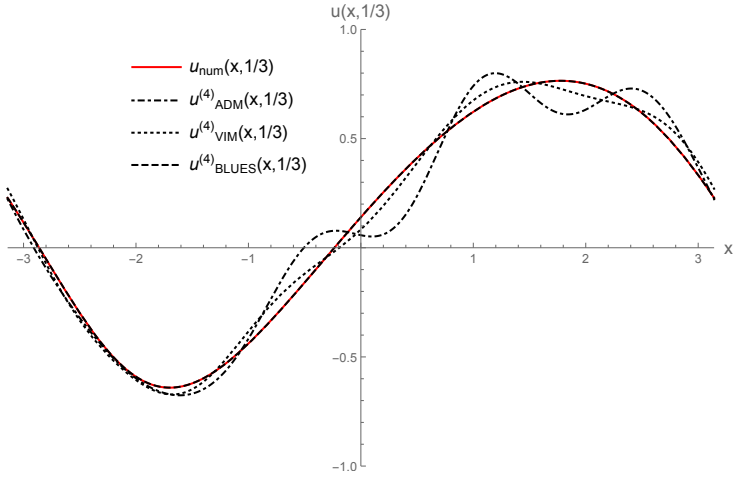

Figure 5.8: Periodic height profile at time $t = 1/3$. The numerical solution (red line) is compared with the $n = 4$ BLUES method approximant (dashed line) and the $n = 4$ approximant of the VIM and the ADM (respectively dot-dashed and dotted lines). At this resolution the fourth BLUES approximant falls on top of the numerical solution. Parameters are $D = \alpha = 1$ and $\beta = -1$.

PDEs yields the expressions given in Appendix A for the perturbative solution $u^{(2)}_{PT}$ up to, and including, second order in α and β.

Note that PT generates terms of second order in α and β, i.e., α^2, β^2 and $\alpha\beta$, and Fourier modes up to and including the third harmonic (with respect to the period of the initial condition). In contrast, in the second iteration the BLUES function method does not yet provide the exact coefficients of the 2nd-order terms. Furthermore, this method also generates terms of higher order in α and β, e.g., α^3, β^3, $\alpha^2\beta$, etc., and Fourier modes of the fourth harmonic are also already present in the second approximant. We provide the full expressions of the Fourier coefficients of the 2nd approximant in Appendix A and compare them quantitatively with PT.

In Fig. 5.9, we compare the second BLUES approximant with 2nd-order PT at $t = 2/3$. Finally, in Fig. 5.10 we show the various $n = 2$ approximations (ADM, VIM and BLUES) for a fixed spatial coordinate $x = \pi$. We remark that the 2nd-order approximations for the ADM and VIM coincide exactly for $x = \pi$.

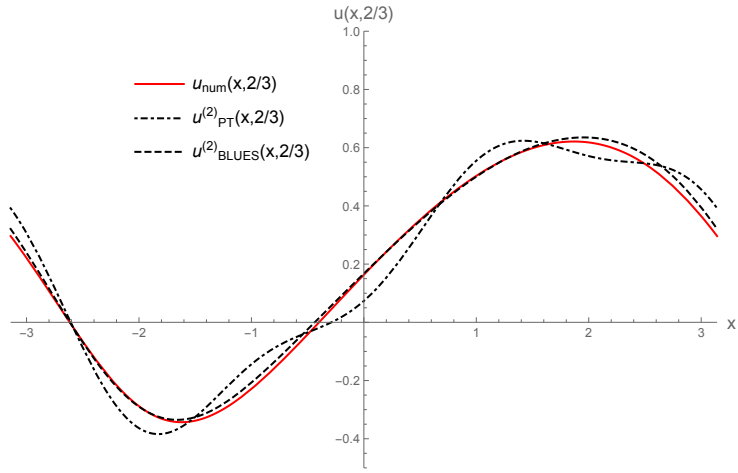

Figure 5.9: Periodic height profile at time $t = 2/3$. The numerical solution (red line) is compared with the $n = 2$ BLUES approximant (dashed line) and the 2nd-order PT (dot-dashed line). Parameters are $D = \alpha = 1$ and $\beta = -1$.

From equation (5.84) it is easy to see that a second harmonic is generated by both deposition and shearing. In further iterations higher harmonics are generated. Hence, the BLUES function method iteratively generates all harmonics as a Fourier series for which the coefficients are time-dependent. These coefficients are recursively modified by the method up to the point that they converge to their final exact value. For the function $u(x, t)$, for fixed time t, the complex

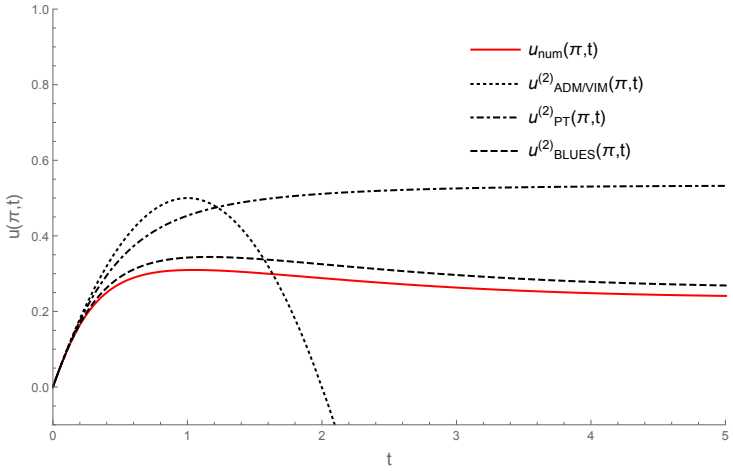

Figure 5.10: Periodic height profile time evolution at position $x = \pi$. The numerical solution (red line) is compared with the $n = 2$ BLUES approximant (dashed line), the $n = 2$ approximants of ADM and VIM (dotted line), which coincide for $x = \pi$, and the $n = 2$ PT (dot-dashed line). Parameters are $D = \alpha = 1$ and $\beta = -1$.

(c_p) and real (a_p and b_p) pth harmonic coefficients in the Fourier series are given by

$$\begin{aligned} c_p(t) &= \frac{1}{2\pi}\int_{-\pi}^{\pi} dx\, u(x,t)\mathrm{e}^{-ipx} \\ a_p(t) &= \frac{1}{\pi}\int_{-\pi}^{\pi} dx\, u(x,t)\cos px \\ b_p(t) &= \frac{1}{\pi}\int_{-\pi}^{\pi} dx\, u(x,t)\sin px, \end{aligned} \tag{5.86}$$

with $c_p = (a_p - ib_p)/2$. In Fig. 5.11 the time evolution of the modulus of the coefficients $c_p(t)$ is shown for $p \in \{0, 1, 2, 3\}$ and a comparison is made between the numerically exact values, the $n = 4$ BLUES approximants and the $n = 4$ ADM and VIM approximants. Note that the coefficients calculated with both the ADM and VIM diverge uncontrollably (truncated lines) as time increases while the BLUES approximants reproduce the exact coefficients almost perfectly. For $p = 3$ the ADM and VIM are nearly coincident for small t.

It is conspicuous that BLUES iteration progresses differently from PT. There is even a qualitative difference. For long times the asymptotic behavior of the BLUES approximants agrees with the numerically exact solution in that all the harmonics decay to zero. This is not always the case in the PT (e.g., for $|c_1(t)|$ and $|c_2(t)|$ in Fig. 5.12). Note that the $|c_2(t)|$ coefficients for BLUES and PT are indistinguishable on the scale of Fig. 5.12.

An interesting quantity is the average asymptotic "excess" Δ of the solution as a consequence of the growth of the interface. This is given by the long-time limit of $c_0(t)$,

$$\Delta \equiv \lim_{t\to\infty} c_0(t) = \frac{1}{2\pi} \lim_{t\to\infty} \int_{-\pi}^{\pi} dx\, u(x,t). \tag{5.87}$$

The numerically obtained precise value for the excess is $\Delta_{\rm num} = 0.2356$, while the nth BLUES approximants give $\Delta_{\rm BLUES}^{(n=0)} = 0$, $\Delta_{\rm BLUES}^{(n=1)} = 0.25$, $\Delta_{\rm BLUES}^{(n=2)} = 0.2604$, $\Delta_{\rm BLUES}^{(n=3)} = 0.2421$, $\Delta_{\rm BLUES}^{(n=4)} = 0.2358$. The parameter values are $D = \alpha = 1$ and $\beta = -1$.

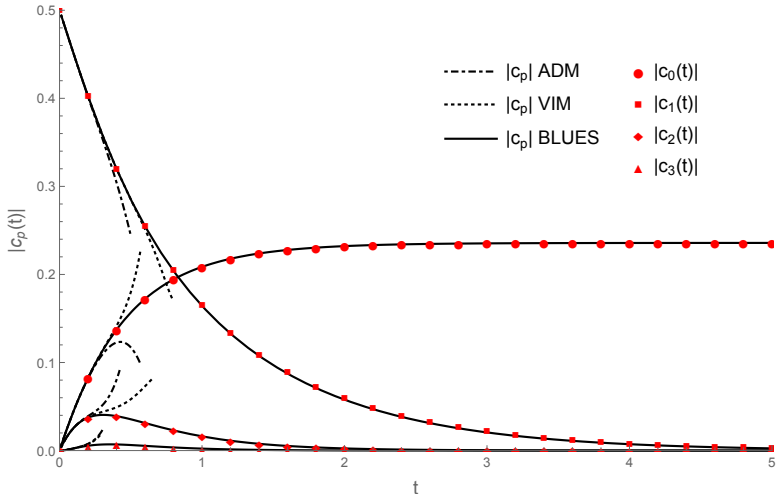

Figure 5.11: Time evolution of the modulus of the pth coefficient, for $p \in \{0,1,2,3\}$, in the Fourier series expansion of the solution of (5.76). The numerical solutions (symbols) for $|c_p(t)|$ are compared with the fourth BLUES approximant (full lines), 4th-order ADM (dotted lines) and 4th-order VIM (dot-dashed lines). Parameter values are $D = \alpha = 1$ and $\beta = -1$. For $p = 3$ the ADM and VIM are nearly coincident for small t.

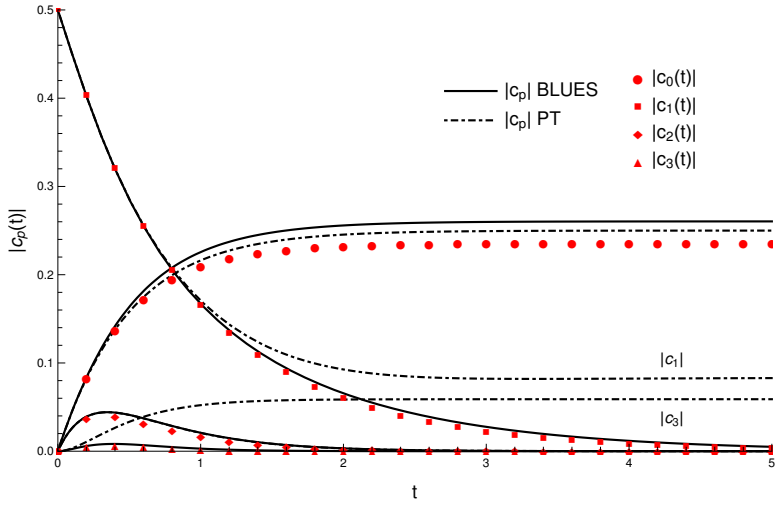

Figure 5.12: Time evolution of the modulus of the pth coefficient in the Fourier series expansion of the solution of (5.76). The numerical solutions (symbols) for $|c_p(t)|$ are compared with the second BLUES approximant (full lines) and 2nd-order PT. Parameter values are $D = \alpha = 1$ and $\beta = -1$. The $|c_2(t)|$ coefficients for BLUES and PT are indistinguishable on this scale.

Chapter 6

Systems of coupled differential equations

In this chapter we present a redefinition of the BLUES function method to study systems of coupled differential equations. We first study extensions to the well-known SIR and SEIR epidemiological models, which are coupled *ordinary* differential equations. Next, we combine the newly minted matrix BLUES function method with concepts from the previous chapter 5 to investigate whether the BLUES function method can be usefully extended to include coupled *partial* differential equations.

This chapter is based on our most recent work, which can be found in the preprints *"Epidemic processes with constant vaccination and immunity loss studied with the BLUES function method"* [61] and *"The BLUES function method for second-order partial differential equations: application to a nonlinear telegrapher equation"* (in preparation). It is supplemented with additional calculations.

6.1 The BLUES function method for coupled DEs

6.1.1 Coupled ordinary differential equations

Here we extend the BLUES iteration to a system of coupled ordinary DEs. The role of the inhomogeneous *source (or sink) term* in the context of the ordinary DE will now be taken over by a vector of sources (or sinks).

Let us start from an n-dimensional system of inhomogeneous nonlinear coupled ordinary DEs that can be written as a nonlinear operator $\mathcal{N}_t$ acting on a vector $\boldsymbol{X}(t)$, with source vector $\boldsymbol{\chi}(t)\Theta(t)$, with $\Theta(t)$ the Heaviside step function (which we take to be unity for positive times *including* $t = 0$),

$$\mathcal{N}_t \boldsymbol{X}(t) = \boldsymbol{\chi}(t), \ \forall t > 0 \tag{6.1}$$

and suitable initial conditions for $t = 0$

$$\boldsymbol{X}(0) = \boldsymbol{C}\,. \tag{6.2}$$

We now judiciously decompose the nonlinear operator $\mathcal{N}_t$ into a linear operator $\mathcal{L}_t$, which contains *inter alia* a first derivative in time, and a residual operator $\mathcal{R}$, i.e., $\mathcal{R} \equiv \mathcal{L}_t - \mathcal{N}_t$, which contains the nonlinear part of $\mathcal{N}_t$. We add the subscript t to the linear and nonlinear operators to emphasize their dependence on time. In the application we consider in this work, $\mathcal{R}$ does not depend on t. Thus the action of the linear operator on $\boldsymbol{X}$ results in the following associated linear coupled system

$$\mathcal{L}_t \boldsymbol{X} = \boldsymbol{X}_t - A\boldsymbol{X} = \boldsymbol{\chi}, \ \forall t > 0 \tag{6.3}$$

where the subscript denotes the derivative w.r.t. time and the same boundary conditions are imposed as in (6.1). The elements of the matrix A are constants in most of the applications we have in mind. We now propose to rewrite the system of DEs in an equivalent form by incorporating the initial condition through multiplication of $\boldsymbol{C}$ with a Dirac delta source $\delta(t)$ located at $t = 0$ and by including this term on the right-hand-side of the inhomogeneous system, i.e.,

$$\mathcal{L}_t \boldsymbol{X} = \boldsymbol{X}_t - A\boldsymbol{X} = \boldsymbol{\chi}\Theta + \boldsymbol{C}\delta \equiv \boldsymbol{\psi}, \ \forall t \geq 0 \tag{6.4}$$

where we have combined the external source $\boldsymbol{\chi}\Theta$ and the "initial condition source" $\boldsymbol{C}\delta$ into the combined source $\boldsymbol{\psi}$. This formulation amounts to reset the initial condition to zero, so that $\boldsymbol{X}(t) = 0$ for $t \leq 0^-$, followed by a jump in $\boldsymbol{X}$ implied by integrating the DE over the delta source, so that $\boldsymbol{X}(0^+) = \boldsymbol{C}$ and $\boldsymbol{X}(t)$ evolves in a continuous manner for $t > 0$. The solution of this linear system (6.48) is the following convolution integral [62, 63]

$$\boldsymbol{X}(t) = (G * \boldsymbol{\psi})(t) = G(t)\boldsymbol{C} + \int_{\mathbb{R}} G(t - t')\boldsymbol{\chi}(t')\Theta(t')\mathrm{d}t', \ \ \forall t > 0 \tag{6.5}$$

where $G(t)$ is the Green function matrix for the inhomogeneous linear system. This object can be calculated by finding the matrix exponential $\exp(At) \equiv \mathbb{1} + At + ...$, i.e.,

$$G(t) = \mathrm{e}^{At}\Theta(t)\,. \tag{6.6}$$

This Green function matrix solves the linear system with a delta function unit matrix source, i.e., it is a solution of the matrix equation

$$G_t(t) - AG(t) = \delta(t)\mathbb{1}.\ \forall t \geq 0 \tag{6.7}$$

Adopting the BLUES function strategy, a solution to the nonlinear system (6.1), rewritten in the equivalent form

$$\mathcal{N}_t \boldsymbol{X} = \boldsymbol{\chi}\Theta + \boldsymbol{C}\delta \equiv \boldsymbol{\psi},\ \forall t \geq 0 \tag{6.8}$$

is now proposed in the form of a convolution $\boldsymbol{X}(t) = (B * \boldsymbol{\phi})(t)$, in which the function $B(t)$, named BLUES function, is taken to be equal to the Green function of the chosen related linear system, i.e., $B(t) = G(t)$ and the new source $\boldsymbol{\phi}(t)$ is to be calculated by systematic iteration, using the given (combined) source $\boldsymbol{\psi}(t)$. This procedure starts from the following implicit equation, which makes use of the action of the residual operator,

$$\boldsymbol{\phi} = \boldsymbol{\psi} + \mathcal{R}(B * \boldsymbol{\phi})\,. \tag{6.9}$$

To find the solution to the nonlinear system (6.1), equation (6.9) can be iterated to calculate an approximation for $\boldsymbol{\phi}$ in the form of a sequence in powers of the residual $\mathcal{R}$. This leads to the sequence $\boldsymbol{\phi}^{(n)}(t)$, with $\boldsymbol{\phi}^{(0)}(t) = \boldsymbol{\psi}(t)$. By subsequently taking the convolution product with $B(t)$, approximate solutions $\boldsymbol{X}_{\psi}^{(n)}(t)$ to (6.1) can be obtained. Explicitly, the iteration for these approximants reads

$$\boldsymbol{X}_{\psi}^{(n)}(t) = (B * \boldsymbol{\phi}^{(n)})(t) = \boldsymbol{X}_{\psi}^{(0)}(t) + \left(B * \mathcal{R}\boldsymbol{X}_{\psi}^{(n-1)}\right)(t)\,, \tag{6.10}$$

where

$$\boldsymbol{X}_{\psi}^{(0)}(t) = (B * \boldsymbol{\phi}^{(0)})(t) = (B * \boldsymbol{\psi})(t) \tag{6.11}$$

is the zeroth approximant, which is the convolution product of the linear problem. We now turn to applying the BLUES iteration procedure to the SIRS epidemiological model for the spreading of infectious diseases.

6.1.2 The SIRS model with constant vaccination

The SIRS model consists of a group of susceptible (S), infected (I) and recovered/immune (R) (human) individuals. The total population $N = S+I+R$ can grow by virtue of a (constant) birth rate π and decay through natural deaths at a rate μ. At birth, the individuals are vaccinated with probability p and

consequently acquire immunity, effectively adding up to the group of immune individuals. The remainder of the new births are added to the susceptible group with probability $1 - p$. Through contact with infected individuals, a person can become infected, following a mass-action law βSI with force of infection βI. The infected can recover with rate γ, acquiring (temporary) immunity and moving to the group of recovered or immune individuals. Finally, immunity can be lost with rate ξ, whereby recovered individuals move back to the susceptible population. Fig. 6.1 illustrates these different processes in a flow diagram. We assume that all system parameters and populations are positive, and $0 \leq p \leq 1$.

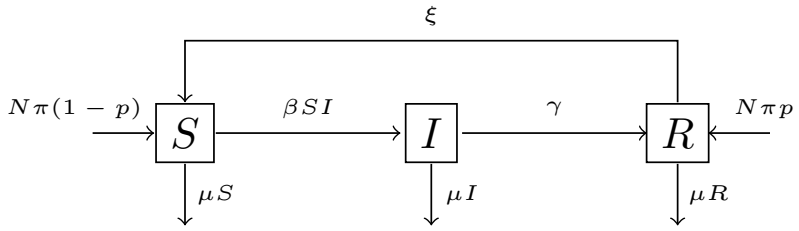

Figure 6.1: SIRS model with vaccination, immunity loss, births and natural deaths.

The interactions between the different populations can be described by the following nonlinear system of DEs, in which the prime denotes derivative w.r.t. time,

$$S'(t) = N(t)\pi(1-p) - \beta\frac{S(t)I(t)}{N(t)} - \mu S(t) + \xi R(t) \tag{6.12a}$$

$$I'(t) = \beta\frac{S(t)I(t)}{N(t)} - (\gamma + \mu)I(t) \tag{6.12b}$$

$$R'(t) = N(t)\pi p + \gamma I(t) - (\mu + \xi)R(t)\,. \tag{6.12c}$$

The time evolution of the total population $N = S + I + R$ can be found by adding (6.12a)-(6.12c)

$$N'(t) = (\pi - \mu)N(t)\,, \tag{6.13}$$

which indicates that the population is not constant. $N(t)$ is a nondecreasing function of t when the birth rate is higher than or equal to the death rate, $\pi \geq \mu$. To study the relative importance of the various population fractions, we scale S, I and R by the total population N, i.e., $s(t) = S(t)/N(t)$, $i(t) = I(t)/N(t)$

and $r(t) = R(t)/N(t)$. This transforms the system (6.12) into the following system for the fractions,

$$s'(t) = \pi(1-p) - \beta s(t)i(t) - \pi s(t) + \xi r(t) \tag{6.14a}$$

$$i'(t) = \beta s(t)i(t) - (\gamma + \pi)i(t) \tag{6.14b}$$

$$r'(t) = \pi p + \gamma i(t) - (\pi + \xi)r(t)\,, \tag{6.14c}$$

where $s(t) + i(t) + r(t) = 1$, $\forall t \geq 0$. Note that μ is eliminated by this transformation. By using the constraint on the population fractions, we can eliminate $r(t)$ and study the "two-dimensional" invariant system

$$s'(t) = \pi(1-p) - \beta s(t)i(t) - (\pi + \xi)s(t) - \xi i(t) + \xi \tag{6.15a}$$

$$i'(t) = \beta s(t)i(t) - (\pi + \gamma)i(t)\,. \tag{6.15b}$$

From a stability analysis performed in appendix B.1, we deduce that the above system has two globally stable fixed points, which are known exactly: a disease-free equilibrium (B.1a) $\varepsilon_0 \equiv (s_0^*, i_0^*) = \left(1 - \frac{\pi p}{\pi+\xi}, 0\right)$ for which the disease is eradicated and an endemic equilibrium (B.1b) $\varepsilon_e \equiv (s_e^*, i_e^*) = \left(\frac{\pi+\gamma}{\beta}, \frac{\beta((1-p)\pi+\xi)-(\gamma+\pi)(\xi+\pi)}{\beta(\gamma+\pi+\xi)}\right)$ for which the disease persists and keeps circulating through the population. The final state of the system is characterised by the *vaccination reproduction number* R_V

$$R_V = \frac{\beta\left((1-p)\pi + \xi\right)}{(\pi+\gamma)(\pi+\xi)}\,, \tag{6.16}$$

which represents the average number of susceptible individuals that are infected by one sick individual during their infectuous period, while a vaccination program is in long-time use [64].

Obviously, the endemic equilibrium ε_e can only exist when $s_e^* < 1$ and $i_e^* > 0$ which means that the vaccination reproduction number must satisfy $R_V > 1$. The disease will be fully eradicated whenever the disease-free equilibrium is the only possible stable fixed point and the endemic equilibrium does not exist. This happens when the vaccination probability is higher than the critical vaccination threshold $p_c^{(\mathrm{SIRS})}$, which can be inferred from equation (6.16) by setting $R_V = 1$,

$$p_c = \left(\frac{\xi}{\pi} + 1\right)\left(1 - \frac{\gamma+\pi}{\beta}\right)\,. \tag{6.17}$$

Note that p_c may exceed unity, whereas p cannot.

6.1.3 BLUES function method for the SIRS model

To find solutions of the system (6.15), we can write it as a nonlinear matrix equation, as was demonstrated in section 6.1, i.e.,

$$\mathcal{N}_t \boldsymbol{X}(t) = \boldsymbol{\psi}(t)\,, \tag{6.18}$$

with $\boldsymbol{X}(t)$ the vector of solutions,

$$\boldsymbol{X}(t) = \begin{pmatrix} s(t) \\ i(t) \end{pmatrix} \tag{6.19}$$

and with source vector $\boldsymbol{\psi}(t) = \boldsymbol{\chi}\Theta(t) + \boldsymbol{C}\delta(t)$. Now $\boldsymbol{\chi}$ is the (time-independent) vector of external sources and $\boldsymbol{C}$ the vector of initial conditions, i.e.,

$$\boldsymbol{\chi} = \begin{pmatrix} \chi_s \\ \chi_i \end{pmatrix} \qquad \text{and} \qquad \boldsymbol{C} = \begin{pmatrix} s_0 \\ i_0 \end{pmatrix} \equiv \begin{pmatrix} s(0) \\ i(0) \end{pmatrix}\,. \tag{6.20}$$

Note that we have included the initial conditions in the source $\boldsymbol{\psi}$ by multiplication with a Dirac point source located at $t = 0$, as was explained in Section 6.1.

Now we judiciously tailor the linear operator that is congruous with the asymptotic equilibrium, by rewriting the nonlinear term in (6.15) so that already the linear system captures the stable fixed point exactly. This is done by including the deviations of the population fractions from their equilibrium values in the (revised) nonlinear term, as follows,

$$\begin{aligned} s'(t) &= \pi(1-p) - \beta(s(t)-s^*)(i(t)-i^*) - (\pi+\xi-\beta i^*)s(t) \\ &\quad - (\xi+\beta s^*)i(t) + \xi + \beta s^* i^* \end{aligned} \tag{6.21a}$$

$$i'(t) = \beta(s(t)-s^*)(i(t)-i^*) - (\pi+\gamma-\beta s^*)i(t) + \beta i^* s(t) - \beta s^* i^*\,, \tag{6.21b}$$

where s^* and i^* are the elements of the fixed point vector $\epsilon = (s^*, i^*)$ which represents the equilibrium that is reached. This equilibrium depends uniquely on the value of R_V. Note that the refurbished nonlinear term vanishes at the fixed point and represents the product of the fluctuations in susceptible and in infected fractions relative to the equilibrium values. This approach captures the correct asymptotic behavior for long times provided the linear relaxation times for both $s(t)$ and $i(t)$ exist. This is the case for all $R_V \neq 1$. We will discuss the special (critical) case $R_V = 1$ separately.

With the calibration chosen as in (6.21) we proceed to identify the linear operator

$$\mathcal{L}_t \boldsymbol{X} = \boldsymbol{X}_t - A\boldsymbol{X} = \boldsymbol{\chi}\Theta + \boldsymbol{C}\delta = \boldsymbol{\psi}\,, \tag{6.22}$$

where the subscript t on $\boldsymbol{X}$ denotes the time derivative, A is the matrix with elements

$$A = \begin{pmatrix} -(\pi + \xi - \beta i^*) & -(\xi + \beta s^*) \\ \beta i^* & -(\pi + \gamma - \beta s^*) \end{pmatrix}, \tag{6.23}$$

and $\boldsymbol{\chi}$ is the vector with elements

$$\boldsymbol{\chi} = \begin{pmatrix} \pi(1-p) + \xi + \beta s^* i^* \\ -\beta s^* i^* \end{pmatrix}. \tag{6.24}$$

The (nonlinear) residual operator $\mathcal{R}$ applied to the solution vector $\boldsymbol{X}$ then takes the form,

$$\mathcal{R}\boldsymbol{X}(t) = \begin{pmatrix} -\beta(s(t) - s^*)(i(t) - i^*) \\ \beta(s(t) - s^*)(i(t) - i^*) \end{pmatrix}. \tag{6.25}$$

Following the procedure outlined in Section 6.1, we construct an iteration sequence (6.10) for the solution vector $\boldsymbol{X}(t)$, i.e.,

$$\boldsymbol{X}^{(n)}(t) = (B * \boldsymbol{\phi}^{(n)})(t) = \boldsymbol{X}^{(0)}(t) + \left(B * \mathcal{R}\boldsymbol{X}^{(n-1)}\right)(t), \tag{6.26}$$

where $B(t)$ is taken to be the matrix Green function $G(t)$ for the linear problem defined through (6.22). This $G(t)$ can be found as the inverse of the fundamental matrix of the matrix of coefficients A or equivalently as the matrix exponential of tA multiplied by a step function, i.e.,

$$G(t) = \mathrm{e}^{tA}\,\Theta(t). \tag{6.27}$$

For the disease-free equilibrium ($R_V < 1$) we obtain,

$$G(t) = \begin{pmatrix} \mathrm{e}^{-(\pi+\xi)t} & \frac{\xi+(\pi+\gamma)R_V}{(\xi-\gamma)+(\pi+\gamma)R_V}\left(\mathrm{e}^{-(\pi+\xi)t} - \mathrm{e}^{-(\pi+\gamma)(1-R_V)t}\right) \\ 0 & \mathrm{e}^{-(\pi+\gamma)(1-R_V)t} \end{pmatrix} \Theta(t). \tag{6.28}$$

In this (simple) case the Green function matrix is triangular, so that its eigenvalues are conspicuous on the main diagonal. These eigenvalues contain the essential "damping" by virtue of the decaying exponentials, with finite "linear relaxation times" $\tau_s = 1/((\pi + \xi)$ and $\tau_i = 1/((\pi + \gamma)(1 - R_V))$. Note that τ_i diverges for $R_V \uparrow 1$. In this limit the relaxation to the disease-free equilibrium becomes "nonlinear". The damping (for $R_V < 1$) ensures that the long-time asymptotics of the approximants, calculated through convolution, are well behaved.

The general Green function matrix, appropriate for both disease-free and endemic equilibria, is more involved and reads,

$$G(t) = \frac{\mathrm{e}^{-\frac{Lt}{2}}}{2M}\begin{pmatrix} Z_+\,\mathrm{e}^{\frac{Mt}{2}} + Z_-\,\mathrm{e}^{-\frac{Mt}{2}} & 2\left(\mathrm{e}^{-\frac{Mt}{2}} - \mathrm{e}^{\frac{Mt}{2}}\right)(\beta s^* + \xi) \\ 2\left(\mathrm{e}^{\frac{Mt}{2}} - \mathrm{e}^{-\frac{Mt}{2}}\right)\beta i^* & Z_+\,\mathrm{e}^{\frac{-Mt}{2}} + Z_-\,\mathrm{e}^{\frac{Mt}{2}} \end{pmatrix}\Theta(t), \tag{6.29}$$

with

$$Z_{\pm} = M \pm K \tag{6.30a}$$

$$K = \gamma - \xi - \beta(s^* + i^*) \tag{6.30b}$$

$$L = \gamma + \xi + 2\pi - \beta(s^* - i^*) \tag{6.30c}$$

$$M^2 = \gamma^2 + \left[\beta(s^* - i^*) + \xi\right]^2 - 2\gamma(\gamma - K)\,. \tag{6.30d}$$

The zeroth approximant (6.11) is the convolution of the matrix Green function with the source vector $\boldsymbol{\psi}(t)$, i.e.,

$$\boldsymbol{X}^{(0)}(t) = (G * \boldsymbol{\psi})(t) = \int_{\mathbb{R}} G(t - t')\left[\boldsymbol{\chi}\Theta(t') + \boldsymbol{C}\delta(t')\right] \mathrm{d}t' \tag{6.31}$$

and results in the following expressions for the population fraction of susceptible and infected individuals, respectively,

$$\begin{aligned}
s^{(0)}(t) = {} & \frac{i_0(\beta s^* + \xi)}{M} \mathrm{e}^{-Lt/2}\left(\mathrm{e}^{-Mt/2} - \mathrm{e}^{Mt/2}\right) \\
& + \frac{s_0}{2M} \mathrm{e}^{-Lt/2}\left(Z_- \, \mathrm{e}^{-Mt/2} + Z_+ \, \mathrm{e}^{Mt/2}\right) \\
& + \frac{2\beta s^* i^* (\beta s^* + \xi)}{M}\left(\frac{(\mathrm{e}^{-Lt/2} - \mathrm{e}^{-Mt/2})}{L - M} - \frac{(\mathrm{e}^{-Lt/2} - \mathrm{e}^{Mt/2})}{L + M}\right) \\
& + \frac{(\beta s^* i^* + \pi(1-p) + \xi)\mathrm{e}^{-Lt/2}}{M}\left(\frac{Z_- \, (\mathrm{e}^{Lt/2} - \mathrm{e}^{-Mt/2})}{L + M}\right) \\
& + \frac{(\beta s^* i^* + \pi(1-p) + \xi)\mathrm{e}^{-Lt/2}}{M}\left(\frac{Z_+ \, (\mathrm{e}^{Lt/2} - \mathrm{e}^{Mt/2})}{L - M}\right)
\end{aligned} \tag{6.32}$$

$$
\begin{aligned}
i^{(0)}(t) = {} & \frac{s_0\beta i^*}{M}\mathrm{e}^{-Lt/2}\left(\mathrm{e}^{Mt/2}-\mathrm{e}^{-Mt/2}\right) \\
& + \frac{i_0}{2M}\mathrm{e}^{-Lt/2}\left(Z_-\,\mathrm{e}^{Mt/2}+Z_+\,\mathrm{e}^{-Mt/2}\right) \\
& - \frac{2\beta i^*(\beta s^* i^* + (1-p)\pi + \xi)\mathrm{e}^{Mt/2}}{M}\left(\frac{(\mathrm{e}^{-Lt/2}-\mathrm{e}^{-Mt/2})}{L-M}\right) \\
& + \frac{2\beta i^*(\beta s^* i^* + (1-p)\pi + \xi)\mathrm{e}^{Mt/2}}{M}\left(\frac{(\mathrm{e}^{-Lt/2}-\mathrm{e}^{-Mt/2})\mathrm{e}^{-Mt}}{L+M}\right) \\
& - \frac{\beta s^* i^*}{M}\mathrm{e}^{-Lt/2}\left(\frac{Z_-\,(\mathrm{e}^{Lt/2}-\mathrm{e}^{Mt/2})}{L-M}+\frac{Z_+\,(\mathrm{e}^{Lt/2}-\mathrm{e}^{-Mt/2})}{L+M}\right). \qquad (6.33)
\end{aligned}
$$

Upon inspection of this and higher approximants (not reported analytically here) we infer that all BLUES approximants, regardless of the number of iterations ($n \geq 0$), are qualitatively correct asymptotically, for all $R_V \neq 1$, in that they converge exponentially rapidly towards the exact fixed point values for long times, in contrast with the other methods which yield divergences.

We proceed to compare graphically the solution of the SIRS model calculated with the BLUES method with a precise numerical solution and with approximate solutions obtained by the ADM, the VIM, or HPM. In Table 6.1 the parameters are shown for three different cases, together with the values for the vaccination reproduction number R_V and critical vaccination threshold p_c. Depending on the value of R_V, we indicate in the last column of Table 6.1 the equilibrium attained by the system.

Table 6.1: Parameters and corresponding equilibria for the 3 studied cases in the SIRS model. The vaccination reproduction number R_V and critical vaccination threshold p_c are also shown. Note that the latter exceeds unity in Case 2, which is physically equivalent to setting it equal to unity. For all cases $s_0 = 0.8$, $i_0 = 0.2$, $r_0 = 0$, $\beta = 0.8$, $\gamma = 0.03$ and $\pi = 0.4$.

	ξ p	p_c	R_V	Equilibrium
Case 1	0.1 0.9	0.5781	0.5209	$\varepsilon_0 = (0.28, 0)$
Case 2	0.5 0.9	$1.0406 \implies 1$	1.1163	$\varepsilon_e = (0.5375, 0.0605)$
Case 3	0.1 p_c	0.5781	1	$\varepsilon_0 = (0.5375, 0)$

Case 1: small loss of immunity and high vaccination probability.

As a preliminary remark, we mention that for $\xi = 0$ (no loss of immunity) the SIRS reduces to a SIR model with vaccination, which was treated earlier in [65, 66] by means of the ADM, HPM and VIM. Here we consider the SIRS model in which the protection offered by vaccination or post-disease immunity is lost with a small rate $\xi = 0.1$ after some time. When the vaccination probability $p = 0.9$ is higher than the critical vaccination threshold $p_c = 0.5781$, the disease will eventually die out and the system will reach the stable disease-free equilibrium for which $i \to 0$ and $s \to 0.28$. This is shown in Fig. 6.2. As we already discussed the BLUES method is accurate and captures the fixed-point values (B.1a) of (s_0^*, i_0^*) in the equilibrium exactly. We remark that the approximants generated by the ADM, VIM and HPM diverge uncontrollably for longer times while the BLUES approximants converge globally for all $t \geq 0$ and in every iteration.

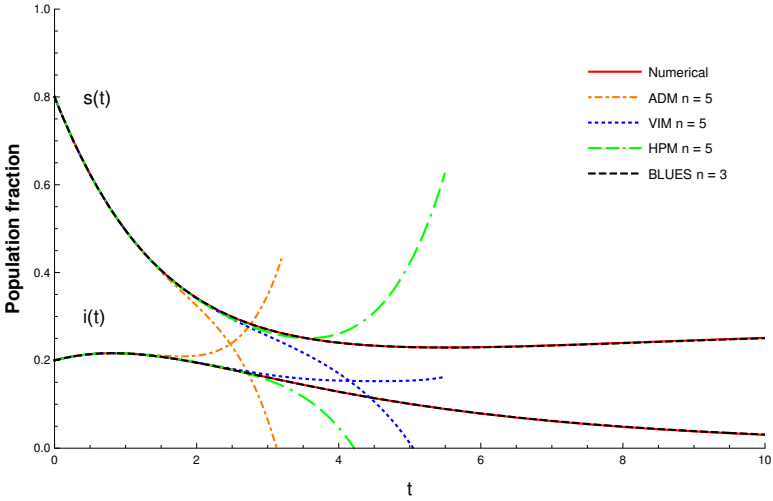

Figure 6.2: Comparison between the numerical solution (red line), the fifth-order VIM, ADM and HPM approximants (respectively, blue dotted, orange dot-dashed and green dot-dash-dashed lines) and the third BLUES approximant (black, dashed line) for Case 1 of the SIRS model: $\xi = 0.1$ and $p = 0.9$. Note that the numerical solution and the third BLUES approximant are indistinguishable at this resolution.

We also compare the BLUES approximants for different numbers of iteration and notice that they converge rapidly towards the numerical solution. This is

shown in Fig. 6.3.

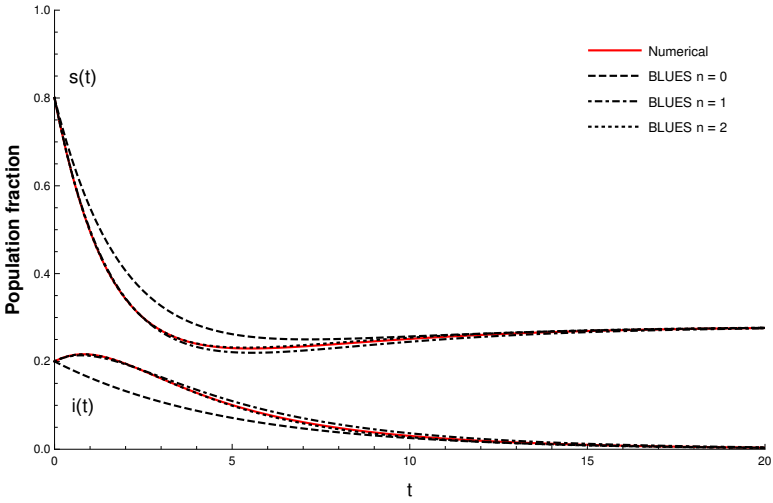

Figure 6.3: Internal comparison among BLUES approximants after zero (dashed line), one (dot-dashed line) and two (dotted line) iterations. The numerical solution is also shown (red line). This figure is for Case 1 of the SIRS model: $\xi = 0.1$ and $p = 0.9$.

Case 2: high loss of immunity and high vaccination probability.

As a second example, we consider the case in which immunity is more easily lost ($\xi = 0.5$) and the population is putting in an effort to vaccinate a larger number of newborns ($p = 0.9$). We can deduce from the critical vaccination probability $p_c = 1.0406$ in Table 6.1 that even when all newborns are vaccinated, immunity is lost so quickly that the population always reaches the endemic equilibrium and the disease cannot be eradicated. The result of a comparison between the VIM, ADM, HPM and BLUES method is shown in Fig. 6.4. We also compare the BLUES approximants for different numbers of iteration and observe that they converge rapidly towards the numerical solution. This is shown in Fig. 6.5.

Case 3: nonlinear relaxation at the dynamical critical point.

In this third example, we consider the dynamical criticality at $R_V = 1$. The population still reaches the disease-free equilibrium asymptotically, but much

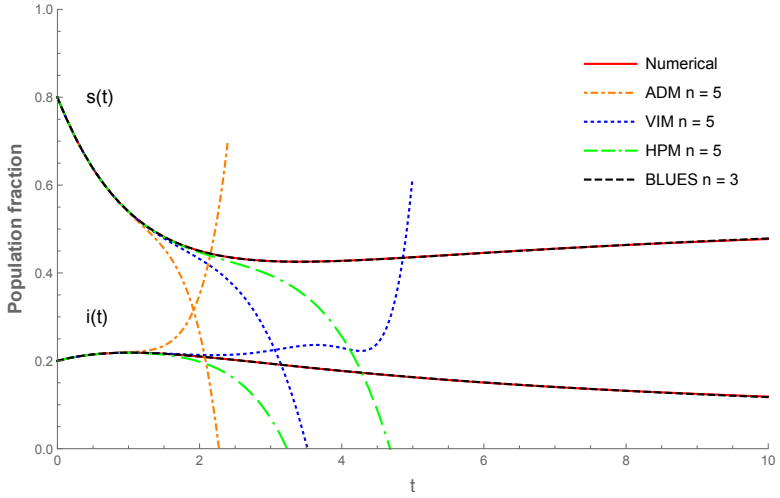

Figure 6.4: Comparison between the numerical solution (red line), the fifth-order VIM, ADM and HPM approximants (respectively, blue dotted, orange dot-dashed and green dot-dash-dashed lines) and the third BLUES approximant (black, dashed line) for Case 2 of the SIRS model: $\xi = 0.5$ and $p = 0.9$. Note that again the numerical solution and the third BLUES approximant are indistinguishable at this resolution.

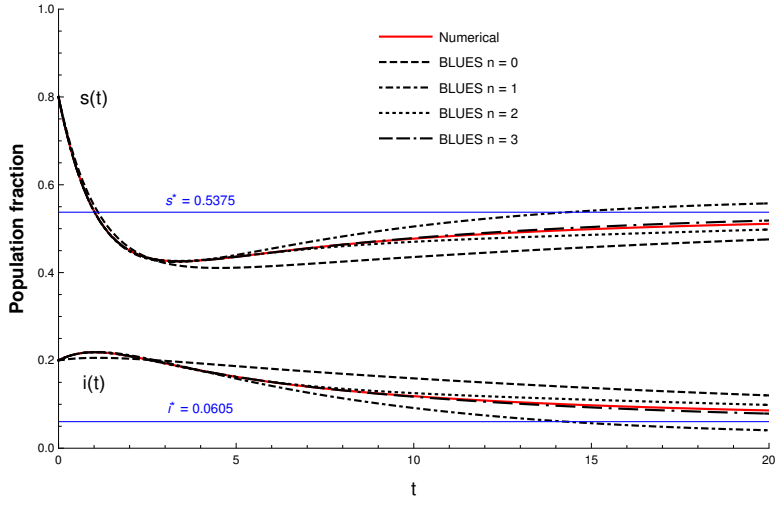

Figure 6.5: Internal comparison among the zeroth-order BLUES approximant (dashed line) and the first three iterations. The numerical solution is also shown (red line). This figure is for Case 2 of the SIRS model: $\xi = 0.5$ and $p = 0.9$.

more slowly since in the limit $R_V \uparrow 1$ the linear relaxation time diverges. The "linear" exponential relaxation is replaced by a "nonlinear" algebraic one, with leading behavior proportional to $1/t$. This can be inferred exactly from an analysis of the asymptotic behavior of the system of DEs (6.21), which at $R_V = 1$ reduces to,

$$s'(t) = \pi(1-p) - \beta(s(t)-s^*)i(t) - (\pi+\xi)s(t) - (\xi+\beta s^*)i(t) + \xi \quad (6.34a)$$

$$i'(t) = \beta(s(t)-s^*)i(t)\,, \quad (6.34b)$$

with, in this special case, $s^* = s_0^* = s_e^*$. Inspection of these DEs yields that the leading asymptotic behavior is a $1/t$ power-law decay towards the fixed point,

$$s(t) = s^* - \frac{1}{\beta\, t} + \mathcal{O}(t^{-2}) \quad (6.35a)$$

$$i(t) = \frac{\pi+\xi}{\pi+\xi+\gamma}\,\frac{1}{\beta\, t} + \mathcal{O}(t^{-2})\,, \quad (6.35b)$$

which can be seen in Fig. 6.7, together with the $n = 0, 2, 4$ BLUES approximants and the numerically exact solutions. In this Case, the BLUES approximants approach the fixed point exponentially with the same linear relaxation time $(\pi+\gamma)^{-1}$ in every iteration while the exact solution approaches the fixed point as a power law. As a consequence, the $n = 4$ BLUES approximant does not coincide exactly with the numerical solution for larger times, in contrast with Cases 1 and 2. This can be seen in Fig. 6.6, where a comparison between the VIM, ADM, HPM and BLUES method is shown together with the numerical solution.

We now calculate the time $t = \hat{t}$ at which the peak of the infection occurs from the BLUES approximants and compare with the numerically precise values. At the infection peak, $i'(\hat{t}\,) = 0$, and hence, using equation (6.15b), we deduce that $s(\hat{t}\,) = (\gamma+\pi)/\beta$. So, instead of trying to solve $i'(\hat{t}\,) = 0$ directly, we can find $\hat{t}$ from the susceptible population fraction. The results are shown in Fig. 6.8. The BLUES function method accurately captures the infection peak time, both for the disease-free and the endemic equilibrium.

The cumulative fraction of infected individuals $\mathcal{A}(t)$ is the integral of $i(t)$. In the disease-free equilibrium this fraction decays to zero and hence the integral is finite. We now inspect this quantity analytically and numerically in the framework of the BLUES approximants. For the zeroth-order approximant (6.33), $\mathcal{A}_0(t)$ is given generally by

$$\mathcal{A}^{(0)}(t) = \int_0^t i^{(0)}(t')\mathrm{d}t' = \frac{i_0}{(\pi+\gamma)(1-R_V)}\left(1 - \mathrm{e}^{-(\pi+\gamma)(1-R_V)t}\right), \quad (6.36)$$

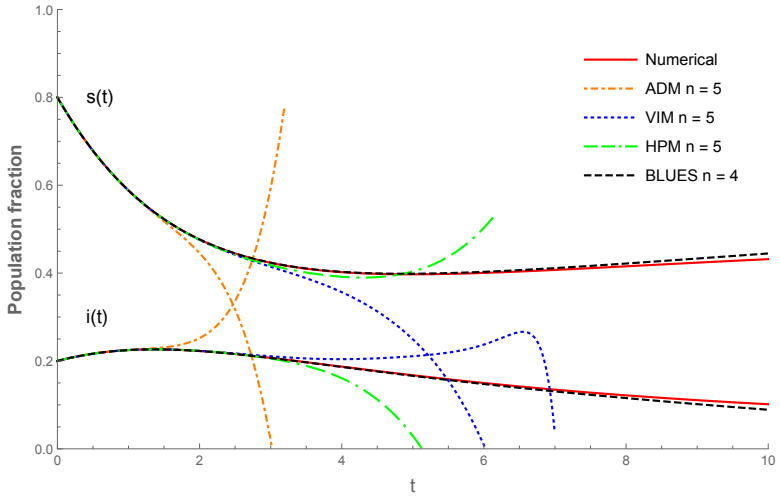

Figure 6.6: Comparison between the numerical solution (red line), the fifth-order VIM, ADM and HPM approximants (respectively, blue dotted, orange dot-dashed and green dot-dash-dashed lines) and the fourth BLUES approximant (black, dashed line). This figure is for Case 3 of the SIRS model: $R_V = 1$.

which is valid for both the disease-free and endemic fixed points. In the latter case, $\mathcal{A}(t)$ is an increasing function of time for all $t > 0$.

It is now easy to see that for the disease-free equilibrium ($R_V < 1$), the exponential decays to zero for $t \to \infty$ and the zeroth-order cumulative fraction of infected individuals saturates at the finite limiting value $\mathcal{A}_\infty^{(0)} = \lim_{t\to\infty} \mathcal{A}^{(0)}(t)$, i.e.,

$$\mathcal{A}_\infty^{(0)} = \frac{i_0}{(\pi+\gamma)(1-R_V)}\,. \tag{6.37}$$

For Case 1 this results in the value $\mathcal{A}_\infty^{(0)} = 0.970874$. The numerically exact value in this case is $\mathcal{A}_\infty^{(num)} = 1.28687$. We can obtain a better approximation by integrating the first-order solution $i^{(1)}(t)$, i.e.,

$$\begin{aligned}\mathcal{A}_\infty^{(1)} = &\frac{i_0^2\beta(\xi + R_V(\pi+\gamma))}{2(\pi+\gamma)^2(1-R_V)^2\left((\pi+\gamma)R_V - (\gamma+\xi+2\pi)\right)} \\ &+ \frac{i_0\left[s_0\beta + (\gamma+\xi+2\pi) - 2R_V(\pi+\gamma)\right]}{(1-R_V)(\pi+\gamma)\left[(\gamma+\xi+2\pi) - R_V(\pi+\gamma)\right]}\,,\end{aligned} \tag{6.38}$$

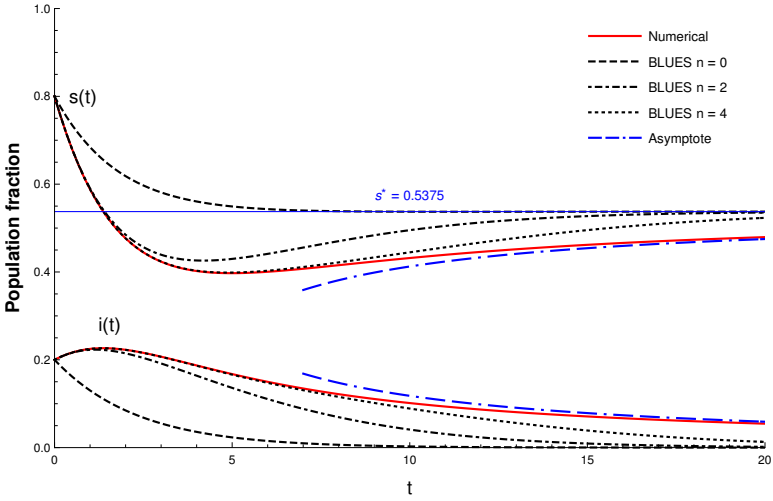

Figure 6.7: Internal comparison among BLUES approximants after zero (dashed line), two (dot-dashed line) and four (dotted line) iterations. The numerical solution is also shown (red line) together with its exact asymptotic behavior (a power-law decay). This figure is for Case 3 of the SIRS model: $R_V = 1$.

which results in the numerical value of $\mathcal{A}_\infty^{(1)} = 1.36991$. The different approximants for the cumulative fraction of infected individuals for Case 1 are compared with the numerical solution in Fig. 6.9.

6.1.4 The SEIRS model with constant vaccination

We will now digress somewhat from the SIRS model and briefly study a well-known extension: the SEIRS model. In this extension to the original SIRS system, individuals do not directly transition from the group of susceptibles (S) to the group of infected (I). Instead, they first pass through a phase of being *exposed* to the disease before becoming sick. Therefore, the new compartment is called the group of exposed individuals (E) and they become sick with a rate σ, moving them to the group of infected individuals. These dynamics are shown in Fig. 6.10.

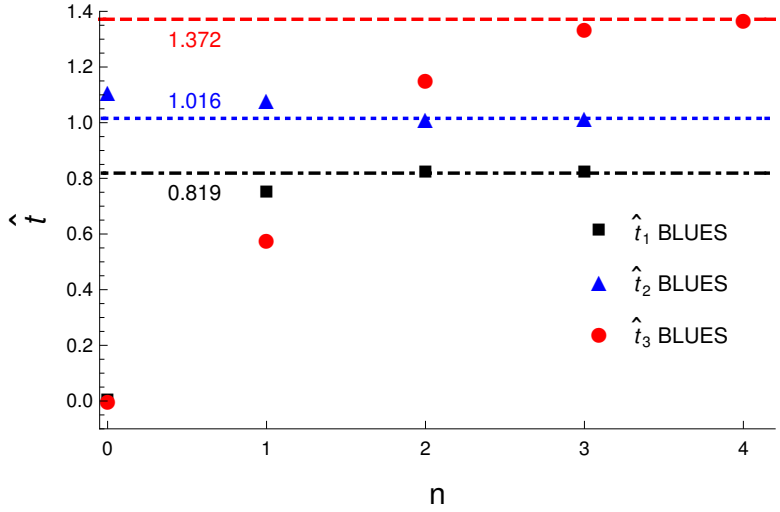

Figure 6.8: Comparison between the numerically precise time of the infection peak $\hat{t}$ in the SIRS model and the values calculated using the nth BLUES approximants ($n = 0, 1, 2, 3$) for Case 1 (black dot-dashed line and black squares), 2 (blue dotted line and blue triangles) and 3 (red dashed line and red circles). For Case 3, the $n = 4$ approximant is also calculated.

The system of nonlinear differential equations describing the time-evolution of the normalised populations is then

$$s'(t) = \pi(1-p) - \beta s(t) i(t) - \pi s(t) + \xi r(t) \tag{6.39a}$$

$$e'(t) = \beta s(t) i(t) - (\sigma + \pi) e(t) \tag{6.39b}$$

$$i'(t) = \sigma e(t) - (\gamma + \pi) i(t) \tag{6.39c}$$

$$r'(t) = \pi p + \gamma i(t) - (\pi + \xi) r(t)\,, \tag{6.39d}$$

with $e = E/N$ the normalized population of exposed individuals, where now the total population is $N = S + E + I + R$.

Adding a new compartment and new interactions to the model changes the vaccination reproduction number and critical vaccination threshold, which we will now denote with superscript (SEIRS), i.e., the reproduction number becomes

$$R_V^{(\mathrm{SEIRS})} = \frac{\beta\sigma\,(\pi(1-p)+\xi)}{(\pi+\gamma)(\pi+\sigma)(\pi+\xi)} = \frac{\sigma}{(\pi+\sigma)} R_V^{(\mathrm{SIRS})}\,. \tag{6.40}$$

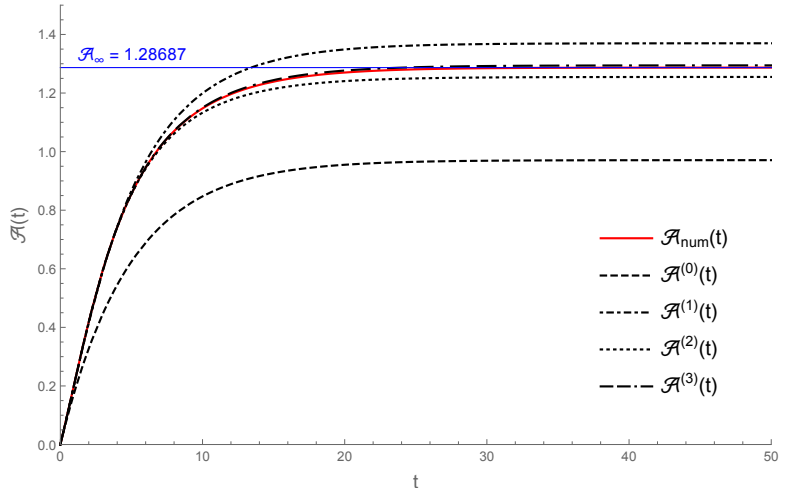

Figure 6.9: The cumulative fraction of infected individuals $\mathcal{A}(t)$ approximated by the the first four BLUES approximants (black lines) together with the numerical result (red, full line) for Case 1. The numerically calculated saturated value of $\mathcal{A}_\infty = 1.28687$ is also shown.

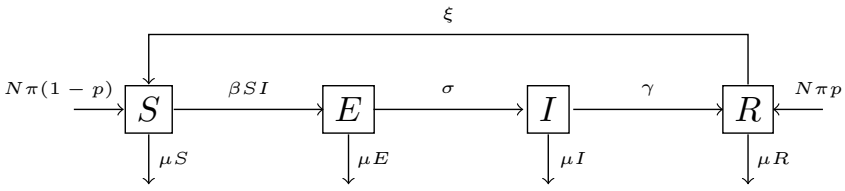

Figure 6.10: The SEIRS model with vaccination, immunity loss and natural deaths.

Note that the reproduction number for the SEIRS model is linearly related to the one in the SIRS model (6.16). However, the critical vaccination threshold is now

$$p_c^{(\mathrm{SEIRS})} = \left(\frac{\xi}{\pi} + 1\right)\left(1 - \frac{(\gamma+\pi)(\sigma+\pi)}{\beta\sigma}\right) . \tag{6.41}$$

We can obtain the critical vaccination threshold for the SIRS model (6.17) by noticing that if the average incubation time $\tau_{inc} = 1/\sigma$ an individual spends in the exposed category is reduced to zero, the exposed class is effectively removed and the SEIRS model reduces to the SIRS model. This can be achieved by

letting the rate σ tend to infinity, i.e.,

$$\lim_{\sigma\to\infty} p_c^{(\mathrm{SEIRS})} = p_c^{(\mathrm{SIRS})}\,. \tag{6.42}$$

In the following discussion, we will omit the superscript (SEIRS). No confusion should arise from this choice.

Global stability properties of the SEIRS model will not be discussed here, but it can be shown [67, 68] that both the disease-free and endemic equilibria are at least locally stable, respectively when the disease dies out and when the disease reaches the endemic equilibrium, depending on the value of R_V.

We can once again carefully choose the linear operator in such a way that it includes both the disease-free and endemic equilibrium. To this end, we first substitute the constraint $s+e+i+r=1$ to eliminate r and reduce the system to a three-dimensional subsystem. Next, we rewrite the nonlinear term as was done in equation (6.21), i.e.,

$$\begin{aligned} s'(t) &= \pi(1-p) - \beta(s(t)-s^*)(i(t)-i^*) - (\pi+\xi-\beta i^*)s(t) \\ &\quad - (\xi+\beta s^*)i(t) - \xi e(t) + \xi + \beta s^* i^* \qquad (6.43a) \\ e'(t) &= \beta(s(t)-s^*)(i(t)-i^*) - (\pi+\sigma)e(t) + \beta i^* s(t) + \beta s^* i(t) \\ &\quad - \beta s^* i^* \qquad (6.43b) \\ i'(t) &= \sigma e(t) - (\pi+\gamma)i(t)\,. \qquad (6.43c) \end{aligned}$$

Next, we can calculate approximants to the solution of (6.39) by using the BLUES method outlined in Section 6.1.3. The exact fixed-point values and detailed calculations for the set-up of the BLUES method for the SEIRS model are performed in appendix B.3. We treat here only two cases, for which the parameter values are indicated in Table 6.2.

Case 1: small loss of immunity and high vaccination probability

We first consider the situation in which the vaccination probability is high and there is some loss of immunity ($R_V < 1$). The systems reaches the stable disease-free equilibrium (B.13a). If we compare Figures 6.2 and 6.11, we see that the infected population fraction in the SEIRS model first decreases and only later reaches a maximum, while the SIRS model only reaches a maximum. This

Table 6.2: Parameters and corresponding equilibria for the two cases in the SEIRS model. The vaccination reproduction number R_V and critical vaccination threshold p_c are also shown. For all cases $s_0 = 0.8$, $e_0 = 0$, $i_0 = 0.2$, $r_0 = 0$, $\beta = 0.8$, $\gamma = 0.03$, $\pi = 0.4$, $\xi = 0.1$ and $\sigma = 5$.

	p	p_c	R_V	Equilibrium
Case 1	0.9	0.5244	0.4823	$\varepsilon_0 = (0.28, 0, 0)$
Case 2	0.3	0.5244	1.3092	$\varepsilon_e = (0.5805, 0.0135, 0.1566)$

can be explained by the fact that the first newly infected individuals initially go through an incubation period before becoming sick and entering the $i(t)$ compartment. Meanwhile, a fraction of the initially sick population recovers, reducing $i(t)$. The BLUES function method is able to reproduce the solutions almost exactly and seems to converge globally, while the VIM, ADM and HPM diverge even for small times.

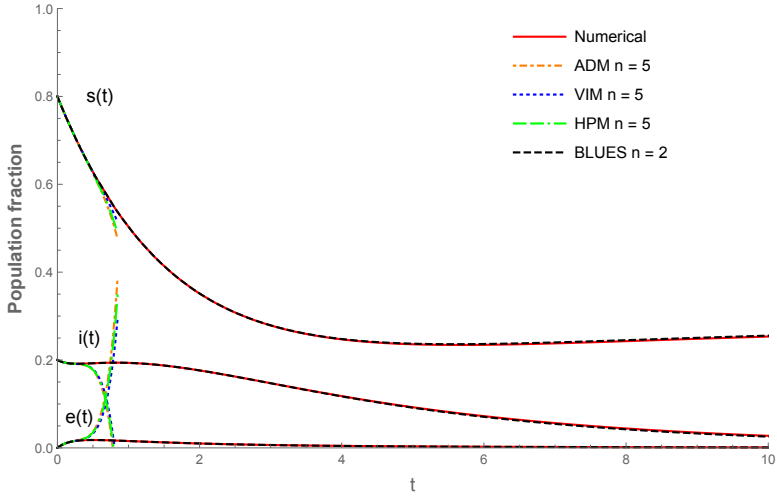

Figure 6.11: Comparison between the numerical solution (red line), the second-order BLUES method solution (black, dotdashed line) and the fifth-order ADM, VIM and HPM approximants (respectively orange dot-dashed, blue dotted and green dot-dash-dashed lines) for Case 1 of the SEIRS model.

Case 2: small loss of immunity and low vaccination probability

As a final example, we assume that the vaccination probability decreases to $p = 0.3$ such that the disease now reaches the endemic equilibrium (B.13b), with $R_V > 1$. Once again, the infected fraction of the population in the SEIRS model first reaches a local minimum before reaching its peak. Already in first order, the BLUES function method generates a very accurate approximation for the exact solution while the other methods diverge quickly.

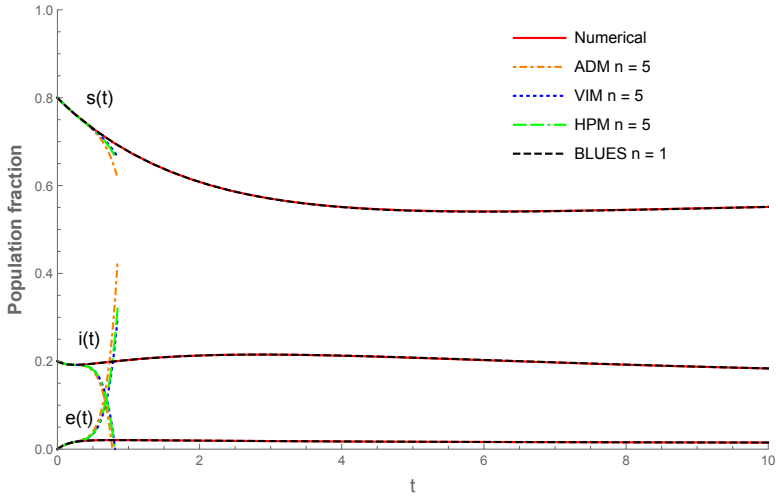

Figure 6.12: Comparison between the numerical solution (red line), the first-order BLUES method solution (black, dotdashed line) and the fifth-order ADM, VIM and HPM approximants (respectively orange dot-dashed, blue dotted and green dot-dash-dashed lines) for Case 2 of the SEIRS model.

We refrain from comparing the different BLUES approximants because the first and second orders are already indistinguishable from the numerically exact solution.

We now conclude the discussion of coupled ODEs and move on the coupled PDEs resulting from either *ab initio* physical systems or by converting higher-order PDEs into a system of coupled first-order nonlinear PDEs.

6.2 Higher-order time derivatives

For nth-order time derivatives the BLUES approach can be extended to include the initial conditions of the derivatives of the solution. We propose the following approach: the nth-order in time nonlinear PDE

$$\widetilde{\mathcal{N}}_{t,x}\, u = \chi(x,t) \tag{6.44}$$

with source $\chi(x,t)$ can be decomposed into n first-order coupled PDEs where the initial conditions for the solution and the derivatives can be included as sources in their respective constituent equations by a suitable multiplication with a point source at $t = 0$. The BLUES method can subsequently be applied to the system of first-order in time equations.

For equation (6.44), this system can be written as a nonlinear operator $\mathcal{N}_{t,x}$ acting on a vector of solutions $\boldsymbol{U} = (U_1, U_2, ..., U_n)$, i.e.,

$$\mathcal{N}_{t,x}\, \boldsymbol{U}(x,t) = \boldsymbol{\psi}(x,t),\ \forall t > 0 \tag{6.45}$$

wherein $U_1 = u$, $U_2 = \partial u/\partial t$, ..., $U_n = \partial^n u/\partial t^n$. The initial conditions for $t = 0$ are collected in the vector $\boldsymbol{C}$,

$$\boldsymbol{U}(x,0) = \boldsymbol{C}(x)\,. \tag{6.46}$$

Now, $\boldsymbol{\psi}(x,t) = (0, ..., \chi(x,t))$ is a vector of length n that contains the external source in the last entry and zeroes everywhere else. We now judiciously decompose the nonlinear operator $\mathcal{N}_{t,x}$ into a linear operator $\mathcal{L}_{t,x}$, which contains at the highest a first derivative in time as a consequence of the decomposition, and a residual operator $\mathcal{R}_x$, i.e., $\mathcal{R}_x \equiv \mathcal{L}_{t,x} - \mathcal{N}_{t,x}$, which contains at least the nonlinear part of $\mathcal{N}_{t,x}$. Thus the action of the linear operator on $\boldsymbol{U}$ results in the following associated linear coupled system

$$\mathcal{L}_{t,x}\, \boldsymbol{U} = \boldsymbol{U}_t - A\boldsymbol{U} = \boldsymbol{\psi},\ \forall t > 0 \tag{6.47}$$

We now propose to rewrite the system of DEs in an equivalent form by incorporating the initial condition by multiplying $\boldsymbol{C}$ with a Dirac delta source $\delta(t)$ located at $t = 0$ and including this term on the right-hand-side of the inhomogeneous system, i.e.,

$$\mathcal{L}_{t,x}\, \boldsymbol{U} = \boldsymbol{U}_t - A\boldsymbol{U} = \boldsymbol{\psi}\Theta + \boldsymbol{C}(x)\delta \equiv \boldsymbol{\varphi},\ \forall t \geq 0 \tag{6.48}$$

where we have combined the external source $\boldsymbol{\psi}\Theta$ and the "initial condition source" $\boldsymbol{C}\delta$ into the combined source $\boldsymbol{\varphi}$.

The solution of this linear system (6.48) is the following convolution integral

$$\begin{aligned}\boldsymbol{U}(x,t) &= (G * \boldsymbol{\varphi})(t) \\ &= G(t)\boldsymbol{C}(x) + \int_{0^-}^{t} G(t-t')\boldsymbol{\psi}(x,t')\Theta(t')\mathrm{d}t', \;\; \forall t > 0\end{aligned} \tag{6.49}$$

where $G(t)$ is the Green function matrix for the inhomogeneous linear system. This object can be calculated by finding the matrix exponential $\exp(At) \equiv \mathbb{1} + At + ...$, i.e.,

$$G(t) = \mathrm{e}^{At}\Theta(t)\,. \tag{6.50}$$

This Green function matrix solves the linear system with a delta function unit matrix source, i.e., it is a solution of the matrix equation

$$G_t - AG = \delta(t)\mathbb{1}, \;\forall t \geq 0\,. \tag{6.51}$$

Adopting the BLUES function strategy, a solution to the nonlinear system (6.45) is now proposed in the form of a convolution $\boldsymbol{U}(x,t) = (B * \boldsymbol{\phi})(x,t)$, in which the function $B(t)$, named BLUES function, is taken to be equal to the Green function of the chosen related linear system, i.e., $B(t) \equiv G(t)$ and the new (combined) source $\boldsymbol{\phi}(x,t)$ is to be calculated by systematic iteration, using the given (combined) source $\boldsymbol{\varphi}(x,t)$. This procedure starts from the following implicit equation, which makes use of the action of the residual operator,

$$\begin{aligned}\mathcal{R}_x\left(B * \boldsymbol{\phi}\right) &= \mathcal{L}_{t,x}\left(B * \boldsymbol{\phi}\right) - \mathcal{N}_{t,x}\left(B * \boldsymbol{\phi}\right) \\ &= \boldsymbol{\phi} - \boldsymbol{\varphi}\,.\end{aligned} \tag{6.52}$$

To find the solution to the nonlinear system (6.45), equation (6.52) can be iterated to calculate an approximation for $\boldsymbol{\phi}$ in the form of a sequence in powers of the residual $\mathcal{R}_x$. By subsequently taking the convolution product with $B(t)$, approximate solutions $\boldsymbol{U}_{\psi}^{(n)}(t)$ to (6.45) can be found, i.e.,

$$\boldsymbol{U}_{\phi}^{(n)}(x,t) = (B * \boldsymbol{\phi}^{(n)})(x,t) = \boldsymbol{U}_{\phi}^{(0)}(x,t) + \left(B * \mathcal{R}_x\,\boldsymbol{U}_{\phi}^{(n-1)}\right)(x,t)\,, \tag{6.53}$$

where

$$\boldsymbol{U}_{\phi}^{(0)}(x,t) = (B * \boldsymbol{\phi}^{(0)})(x,t) = (B * \boldsymbol{\varphi})(x,t). \tag{6.54}$$

is the zeroth-order convolution product where the sources $\boldsymbol{\phi}^{(0)}(x,t)$ and $\boldsymbol{\phi}(x,t)$ are identical.

We can now continue our discussion with an application to a second-order nonlinear PDE.

6.2.1 BLUES function method for the nonlinear telegrapher equation

The linear telegrapher equation with $\alpha, c \in \mathbb{R}$

$$u_{tt}(x,t) + \alpha u_t(x,t) - c^2 u_{xx}(x,t) = 0 \tag{6.55}$$

is used in a broad spectrum of scientific disciplines, ranging from electrical transmission in cables to the statistical mechanics of active matter [69, 70] and mathematical biology [71, 72]. Equation (6.55) interpolates between the wave equation ($\alpha \to 0$ with c fixed) and the diffusion equation ($\alpha \to \infty$ and $c \to \infty$, with $c^2/\alpha \to D$ constant) and has the advantage of having a finite propagation speed for disturbances, in contrast to the infinite disturbance propagation speed for the diffusion equation [73]. For the remainder of this work we will assume $c = 1$ without loss of generality.

We now consider the telegrapher equation with a quadratic nonlinearity and constant forcing, i.e.,

$$\begin{aligned} \widetilde{\mathcal{N}}_{t,x}\, u &= \frac{\partial^2 u}{\partial t^2} + \alpha \frac{\partial u}{\partial t} - c^2 \frac{\partial^2 u}{\partial x^2} + u^2 = 1 \\ u(x,0) &= f(x) \\ \frac{\partial u}{\partial t}(x,0) &= g(x) \end{aligned} \tag{6.56}$$

where $f(x)$ and $g(x)$ are the initial conditions for respectively $u(x,t)$ and the time derivative $u_t(x,t)$. We will now attempt to generate approximate solutions to equation (6.56) using the formalism developed in section 2.1.

We can convert this second-order PDE (6.56) into two coupled first-order PDEs by introducing $v = \partial u/\partial t$, i.e.,

$$\begin{aligned} \frac{\partial u}{\partial t} &= v \\ \frac{\partial v}{\partial t} &= \frac{\partial^2 u}{\partial x^2} - \alpha v - u^2 + 1 \end{aligned} \tag{6.57}$$

We can rewrite the system (6.57) with solution vector $\boldsymbol{U} = (u, v)^\intercal$ such that it has the form required by the matrix BLUES function method (6.45),

$$\mathcal{N}_{t,x}\, \boldsymbol{U}(x,t) = \boldsymbol{\varphi}(x,t)\,, \tag{6.58}$$

where the linear operator $\mathcal{L}_{t,x}\boldsymbol{U}$, residual $\mathcal{R}_x\boldsymbol{U}$ and source vector $\boldsymbol{\varphi}$ are given by the following expressions

$$\begin{aligned}\mathcal{L}_{t,x}\boldsymbol{U} &= \begin{pmatrix} u_t \\ v_t \end{pmatrix} - A\begin{pmatrix} u \\ v \end{pmatrix} \qquad \boldsymbol{\varphi} = \delta(t)\begin{pmatrix} f(x) \\ g(x) \end{pmatrix} + \begin{pmatrix} 0 \\ 1 \end{pmatrix} \\ \mathcal{R}_x\boldsymbol{U} &= \begin{pmatrix} 0 \\ u_{xx} - u^2 \end{pmatrix}\end{aligned} \tag{6.59}$$

The matrix of coefficients A of the linear operator is

$$A = \begin{pmatrix} 0 & 1 \\ 0 & -\alpha \end{pmatrix} \tag{6.60}$$

and hence the matrix Green function for the linear operator is the matrix exponential $G(t) = \exp\{(At)\}\Theta(t)$, i.e.,

$$G(t) = \begin{pmatrix} 1 & \frac{1-\mathrm{e}^{-\alpha t}}{\alpha} \\ 0 & \mathrm{e}^{-\alpha t} \end{pmatrix}\Theta(t)\,, \tag{6.61}$$

where $\Theta(t)$ is the Heaviside step function.

We can now set up the BLUES iteration procedure. The nth approximant for the solution of (6.57) is calculated by

$$\boldsymbol{U}^{(n)}(x,t) = \boldsymbol{U}^{(0)}(x,t) + \int_{0^-}^{t} G(t-s)\mathcal{R}_x\boldsymbol{U}^{(n-1)}(x,s)\mathrm{d}s \tag{6.62}$$

where $\boldsymbol{U}^{(0)}(x,t)$ is the zeroth approximant and is defined as the convolution product of the Green function and the source $\boldsymbol{\varphi}(x,t)$, i.e,

$$\boldsymbol{U}^{(0)}(x,t) = \left(f(x) + \frac{t}{\alpha} + \frac{1-\alpha g(x)}{\alpha^2}(\mathrm{e}^{-\alpha t} - 1), \frac{1}{\alpha} - \frac{1-\alpha g(x)}{\alpha}\mathrm{e}^{-\alpha t}\right)^{\intercal} \tag{6.63}$$

For initial conditions $f(x) = 1 + \sin(x)$ and $g(x) = 0$, the zeroth approximant becomes (for $\alpha = 1$),

$$\boldsymbol{U}^{(0)}(x,t) = \left(t + \sin(x) + \mathrm{e}^{-t}, 1 - \mathrm{e}^{-t}\right)^{\intercal}\,. \tag{6.64}$$

Note that when a higher-order PDE is converted to a system of coupled PDEs, the residual is zero in the individual channels of the "new" variables, i.e., the derivatives. The matrix formalism therefore decouples into individual integrations of the elements in the last column of the Green function matrix

with the residual applied to the previous approximant for the solution $u(x,t)$. Hence, it is only necessary to perform the integration corresponding to the channel for the solution $u(x,t)$ and not for all the derivatives. However, this is not the case when the system is *a priori* coupled and the Green matrix and residual are nontrivial.

In Figs. 6.13 and 6.14, we compare the approximate solutions of the matrix BLUES method, VIM, ADM, HPM and GVIM for $\alpha = 1$, with initial conditions $f(x) = 1 + \sin(x)$ and $g(x) = 0$. In Fig. 6.13, the spatial profile of the approximants is shown for a fixed time $t = 1$. It is clear that the matrix BLUES function method outperforms the VIM, ADM and HPM and is comparable to the GVIM. This is confirmed in Fig. 6.14, where the time evolution of the approximants for fixed position $x = -\pi/2$ is shown. Note however that all of the implemented methods diverge for $t \to \infty$. The accuracy can be increased by considering higher-order iterations.

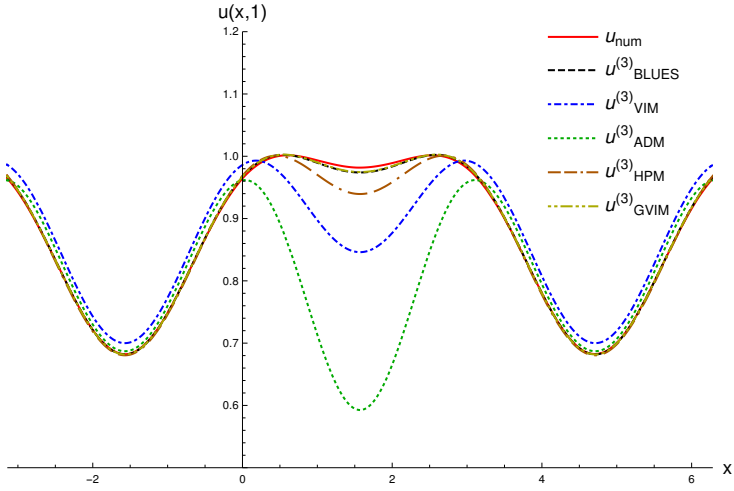

Figure 6.13: A comparison is made between the numerical solution of equation (6.56) (red, full line), the matrix BLUES method (black, dashed line), the VIM (blue, dot-dashed line), ADM (green, dotted line), the HPM (brown, dot-dash-dashed line) and the GVIM (yellow, dot-dot-dashed line). The time is fixed at $t = 1$.

Note that while all of the methods can quite accurately reproduce the spatial profile at the *global* minima, the behaviour differs significantly in the region where the maxima and *local* minima occur (e.g., around $x = \pi/2$). The VIM, ADM, HPM, GVIM and the BLUES function method succeed in reproducing a

(local) minimum at the correct coordinates at a fixed time $t = 1$, albeit with varying degrees of success.

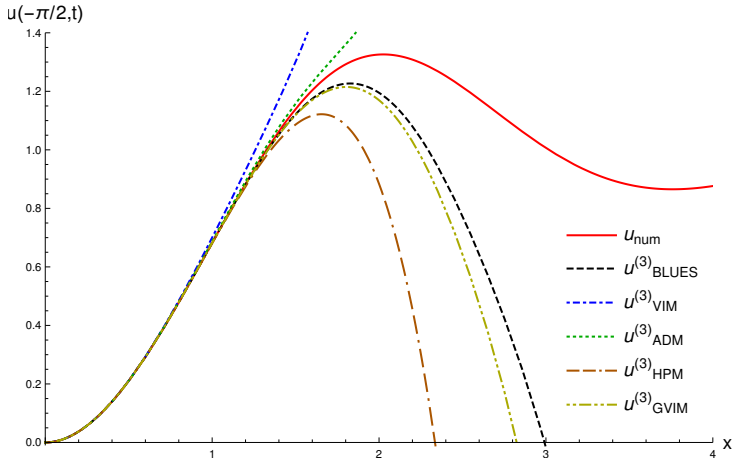

Figure 6.14: A comparison is made between the numerical solution of equation (6.56) (red, full line), the matrix BLUES method (black, dashed line), the VIM (blue, dot-dashed line), ADM (green, dotted line), the HPM (brown, dot-dash-dashed line) and the GVIM (yellow, dot-dot-dashed line). The position is fixed at $x = -\pi/2$.

To study the time evolution of the approximants more closely, we first average the solutions over one period to eliminate spatial dependency. Hence, we study the following time-dependent function

$$\mu(t) = \frac{1}{2\pi} \int_{-\pi}^{\pi} u(x,t) \mathrm{d}x \tag{6.65}$$

for all of the above methods. This is shown in Fig. 6.15. In Fig. 6.16, the consecutive matrix BLUES method approximants for $n \in \{0, 1, 2, 3\}$ are compared with the numerical solution at $t = 1$. Note that the local minimum around $x = \pi/2$ is reproduced in third order.

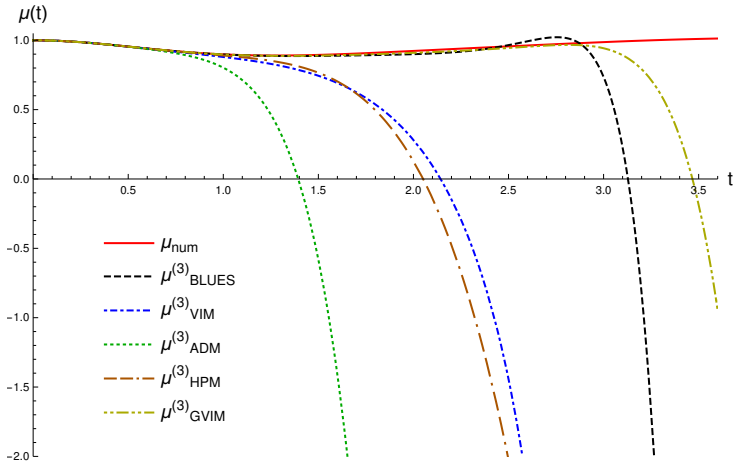

Figure 6.15: Time evolution of the one-period averaged approximants (6.65) of the solution of equation (6.56). A comparison is made between the numerical solution of equation (6.56) (red, full line), the matrix BLUES method (black, dashed line), the VIM (blue, dot-dashed line), ADM (green, dotted line), the HPM (brown, dot-dash-dashed line) and the GVIM (yellow, dot-dot-dashed line).

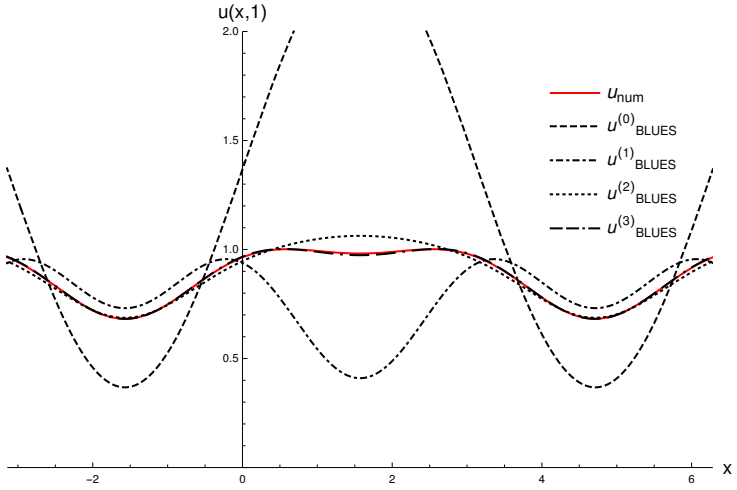

Figure 6.16: Spatial plot of the solution of the nonlinear telegrapher equation (6.56) for a fixed time $t = 1$. A comparison is made between the numerical solution (red, full line) and the $n \in \{0, 1, 2, 3\}$ matrix BLUES method approximants (black lines).

Chapter 7

Hierarchical deposition models

In this chapter we first study a model for the hierarchical *random* deposition (HRDM) of debris onto a flat substrate. We calculate the number of coastal points and the percolation probability. From these calculations, we deduce a connection between these two seemingly unrelated quantities. Furthermore, we briefly comment on surface roughness properties. Next, we extend the rules of the model to include lateral adhesion of incoming particles, transforming the model into the hierarchical *ballistic* deposition process (HBDM). We study the void fraction or porosity, the surface length increment and the roughness exponents analytically and by means of numerical simulations.

The first part of this chapter, i.e., the hierarchical random deposition model, is based on the article *"Coastlines and percolation in a model for hierarchical random deposition"* that appeared in *Physica A: Statistical Mechanics and its Applications* [74]. It builds upon earlier work of Evi Bervoets and Claudiu V. Giuraniuc (University of Aberdeen) who performed the initial calculation of the number of coastal points. The hierarchical ballistic deposition model calculations and numerical simulations are based on my most recent research on this topic.

7.1 Logarithmic fractals

While both Euclidean and fractal geometry are well-known to physicists and mathematicians, the borderline case where the Hausdorff-Besicovitch dimension D_f equals the topological (or Euclidean) dimension D has received much less attention in the literature. A subset of these cases can be characterised by the fractal measure h with ruler length ρ

$$h(\rho) = \rho^{D_f} \left[\log\left(1/\rho\right)\right]^{\Delta_1} \text{ , with } D_f = D, \tag{7.1}$$

where Δ_1 is a subdimension [75]. The occurrence of the logarithm in the fractal measure has led researchers [76] to coin the term *logarithmic fractals*. These objects can be distinguished from classical fractals by observing that quantities such as length and area increase linearly instead of exponentially, upon decreasing the "ruler length". The same research has shown that the logarithmic fractal behaviour of a basic model for hierarchical deposition is robust under randomness and that the surface length or area, asymptotically for large generation number, increases by a constant.

One can study level sets for random hierarchical deposition on a Euclidean substrate of dimension D and the resulting collection of points or contour lines, which are, respectively, named coastal points and coastlines for $D = 1$ or $D = 2$ [77]. This nomenclature stems from the context of islands, which result when the landscape is flooded up to a certain level, and is useful for describing the geometry of their jagged beaches. Real-world applications of fractal level sets come to mind when considering such geometries, some examples include the flooding of Arctic melt ponds [78] or the fractal growth of thin metallic films [79] or of bacterial populations [80, 81].

The study of level sets is deeply connected to the theory of percolation [82, 83], in which the geometry of the system under consideration changes drastically when the deposition probability reaches a critical value named the *percolation threshold*. When percolation is achieved, one expects the behaviour of the number of coastal points/coastlines to change. We will show that in the random hierarchical deposition model the percolation threshold indicates a transition from a Euclidean to a fractal geometry. Exactly at the percolation threshold, however, the number of coastal points exhibits a logarithmic fractal behaviour, growing linearly with increasing generation number.

7.2 Hierarchical random deposition

In this section we recapitulate briefly the setup and some of the elementary properties of the hierarchical deposition model in the situation when the substrate dimension is $D = 1$ (and $D = 2$). Let us consider the deposition of squares (or the digging of square holes) on a line $[0, 1]$ which fall down in a temporal order determined by their size. The largest ones fall down first, followed by squares of which the sides are smaller by a factor λ. We assume a hyperbolic distribution of the number of squares deposited according to their size. The number of squares of linear size s is denoted by $N(s)$ and obeys the following scaling,

$$N(s) = \lambda^{-1} N(s/\lambda) \tag{7.2}$$

where $\lambda \in \mathbb{R}^+$ and $\lambda > 1$. One can see that the number of squares is proportional to the inverse impact cross-section. In this model [76, 77] a logarithmic fractal law was found for the surface (length) of the resulting landscape. An illustration of this landscape is shown in Fig. 7.1. Note that it resembles a skyline of a city [84], with the characteristic urban morphology of the different building layers.

Figure 7.1: Resulting landscape for the HRDM with $\lambda = 3$, $P = 0.5$ and $Q = 0$ after six generations.

Let us first recapitulate the above model for *random* deposition, as was investigated in [76]. First, divide the unit interval in λ subsets of length $1/\lambda$, where now $\lambda \in \mathbb{N}$ and either deposit a square "hill" in each of the subsets with probability P or dig a square "hole" with probability Q, which reduces the height with a factor λ. The third option is to do nothing with probability $1 - S \equiv 1 - (P + Q)$. In the second generation ($n = 2$) we divide each of the subsets of the previous generation in smaller subsets with length $1/\lambda^2$ and start

depositing blocks or digging holes once again. This process can be repeated indefinitely and the resulting asymptotic fractal properties for the generation number $n \to \infty$ can be studied.

It has been shown in [76] that for $\lambda \geq 3$, the asymptotic surface length increment ΔL_∞ for infinite generation number n has the following form

$$\Delta L_\infty = \frac{2\left[P(1-P)+Q(1-Q)\right]}{1+2\left[P(1-P)+Q(1-Q)-PQ\right]/(\lambda-1)}\,, \tag{7.3}$$

while for $\lambda = 2$, partial levelling of vertical segments of the landscape increases the resulting surface length increment somewhat [76].

These results are easily extended to one substrate dimension higher [76]. The main difference with respect to the situation for $D = 1$ is that in $D = 2$ the number of cubes of linear size s is inversely proportional to their cross-sectional area s^2, i.e.,

$$N(s) = \lambda^{-2} N(s/\lambda) \tag{7.4}$$

and that in generation n a wall that was put in generation m occupies λ^{n-m} edges. The surface is now divided into square *plaquettes*. Neighbouring plaquettes share an edge. In generation n there are λ^{2n} plaquettes and twice as many edges. After a careful inspection and calculation one concludes that the (dimensionless) area increment for $D = 2$ obeys a law similar to that which is satisfied by the (dimensionless) length increment for $D = 1$. The substrate directions manifest themselves as independent. Consequently, in dimensionless units of reduced area, ons obtains twice the result of equation (7.3) for $D = 2$, i.e., the *area* increment is related to the *length* increment through [76],

$$\Delta S_\infty = 2\Delta L_\infty\,. \tag{7.5}$$

7.2.1 Coastal points and non-universality

A richer variety of phenomena appears when level sets of the deposition model are studied [77]. We define a "sea level" in the landscape and study the geometry of the coastal points in $D = 1$ (or coastlines in $D = 2$) that remain. If the substrate upon which the squares are placed is a line, the level set at sea level is the number of coastal points. For $D = 2$, i.e., the substrate is planar, the level set is the total length of the coastlines of the resulting islands. In the following discussion, we choose the sea level to be close to the zero level of the substrate. We will present here the case for the one-dimensional model in which the substrate is a line, generalization to higher dimensions is straightforward.

Consider the unit interval $[0, 1]$ with rescaling factor $\lambda \geq 2$ and probabilities P, Q, respectively, to deposit a hill or dig a hole. In generation n, we will call a

coastal point a meeting point at sea level between two segments of length λ^{-n}, one of which supports a newly placed hill above sea level and the other marking a newly dug hole below sea level or being a segment that has remained at sea level, and vice versa, as shown in Fig. 7.2. Points that are created and are not coastal points we call *internal points*. Points that remain from a previous generation without being coastal or internal points are called *external points*.

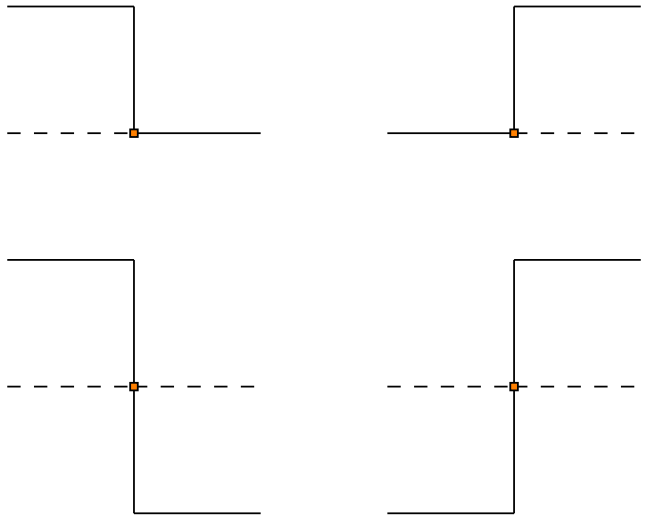

Figure 7.2: Definition of coastal points. The dotted line indicates sea level, while full lines represent either a hill or a hole. The coastal points are drawn as orange squares.

New coastal points can be created in generation n in a number of different ways [85, 86]:

1. Internal points are formed in generation n on a segment which was at sea level in generation $n-1$, see Fig. 7.3. These internal points from all previous generations generate on average the following number of coastal points
$$\lambda(\lambda-1)(1-S)\sum_{i=2}^{n}\left[\lambda(1-S)\right]^{i-2}2P(1-P)\,. \tag{7.6}$$
2. External points at sea level that did not experience any deposition up until generation $n-1$, see Fig. 7.4.

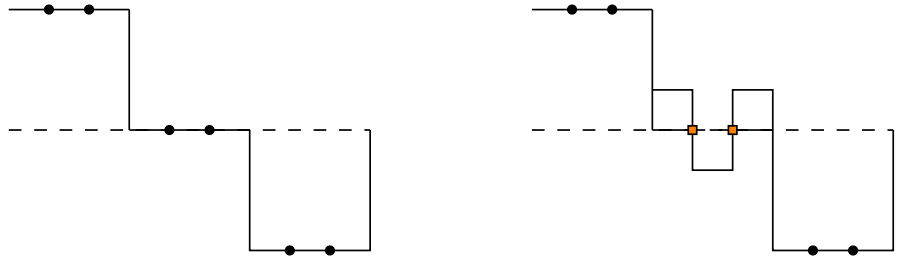

Figure 7.3: Creation of coastal points (orange squares) in generation n (right) by deposition on internal points (black circles) that were still at sea level in generation $n-1$ (left).

Figure 7.4: Creation of coastal points (orange square) in generation n (right) by deposition on external points (black squares) that were still at sea level in generation $n-1$ (left).

These external points generate on average

$$\begin{aligned} &\lambda \sum_{i=1}^{n} \left[(1-S)^2\right]^{i-1} 2P(1-P) \\ &+ \lambda(\lambda-1)(1-S)^3 \left(\sum_{k=3}^{n} \sum_{i=3}^{k} \lambda^{k-i}(1-S)^{k-6+i} \right) 2P(1-P) \end{aligned} \tag{7.7}$$

coastal points in generation n.

3. External points at sea level which at generation $n-1$ connect a segment at sea level with a hole. Placing a hill on sea level next to the hole in generation n creates the coastal point, see Fig. 7.5. This procedure yields the following number of coastal points

$$2\lambda Q(1-S) \left(\sum_{k=2}^{n} \sum_{i=2}^{k} \lambda^{k-i}(1-S)^{k-4+i} \right) P\,. \tag{7.8}$$

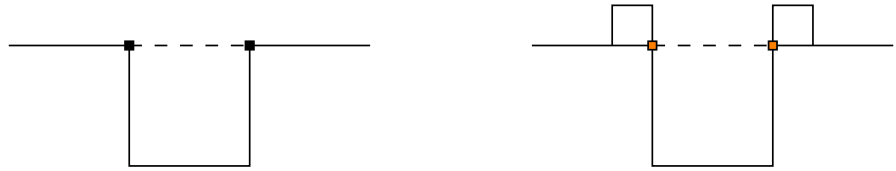

Figure 7.5: Creation of coastal points (orange squares) in generation n (right) by deposition on external points (black squares) which at generation $n-1$ (left) connect a segment at sea level with a hole.

Coastal points can also be destroyed in generation n by placing a smaller hill on a sea level segment right next to an existing hill, hereby lifting the point. This is illustrated in Fig. 7.6. On average, the number of coastal points that

Figure 7.6: Destruction of coastal points (orange squares) in generation $n-1$ (left) by deposition of a smaller hill on sea level, lifting the point in generation n (right).

get destroyed in generation n is equal to

$$2\lambda P(1-S)\left(\sum_{k=2}^{n}\sum_{i=2}^{k}\lambda^{k-i}(1-S)^{k-4+i}\right)P\,. \tag{7.9}$$

Finally, adding equations (7.6), (7.7), (7.8) and subtracting equation (7.9) results in a complete expression for the number of coastal points $\mathcal{N}_n(P,Q)$ in

generation n as a function of the deposition probabilities P and Q,

$$\begin{aligned}\mathcal{N}_n(P,Q) = \lambda \sum_{i=1}^{n} \left[(1-S)^2\right]^{i-1} 2P(1-P) \\ + \lambda(\lambda-1)(1-S) \sum_{i=2}^{n} \left[\lambda(1-S)\right]^{i-2} 2P(1-P) \\ + 2\lambda(Q-P)(1-S) \left(\sum_{k=2}^{n} \sum_{i=2}^{k} \lambda^{k-i}(1-S)^{k-4+i} \right) P \\ + \lambda(\lambda-1)(1-S)^3 \left(\sum_{k=3}^{n} \sum_{i=3}^{k} \lambda^{k-i}(1-S)^{k-6+i} \right) 2P(1-P)\,.\end{aligned} \tag{7.10}$$

The number of coastal points (7.10) for generation $n = 10$ are shown in Fig. 7.7 for $\lambda = 2$ and $Q = 0.2$ together with numerical results from simulations which were performed using direct simulation with a random number generator. The sums in expression (7.10) can be worked out exactly and the expression can be simplified. The details of these calculations can be found in the appendix C. From these calculations one can distinguish three regimes for the number of coastal points:

- Euclidean regime for $\lambda(1-S) < 1$. Here the number of coastal points saturates to a constant value γ, see equation (C.2).
- Fractal regime with nontrivial fractal dimension $0 < D_f < 1$ for $\lambda(1-S) > 1$. In this regime the number of coastal points increases exponentially.
- Logarithmic fractal regime at $\lambda(1-S) = 1$. The number of coastal points increases linearly with increasing generation n.

This non-universality of the coastal points is in sharp contrast with the universal fractal properties of the surfaces described in Section 7.2, which are always marginally fractal, independent of the model parameters. Note that the term "(non)-universality" does not pertain to a universality class but is merely a linguistic choice to describe this behaviour. In two dimensions ($D = 2$), the previously obtained expression for the number of coastal points (7.10) is to be multiplied by a factor 2 in order to obtain the (dimensionless) length of the coastline. This can easily be verified by noticing that in each generation a number of $2\lambda(\lambda-1)(\lambda^{j-1})^2$ become available and the size reduction is λ^{-j}. In Fig. 7.8, a two-dimensional *cityscape* is shown where the volume underneath height $h = 0$ is "flooded" to show the formation of islands and coastlines.

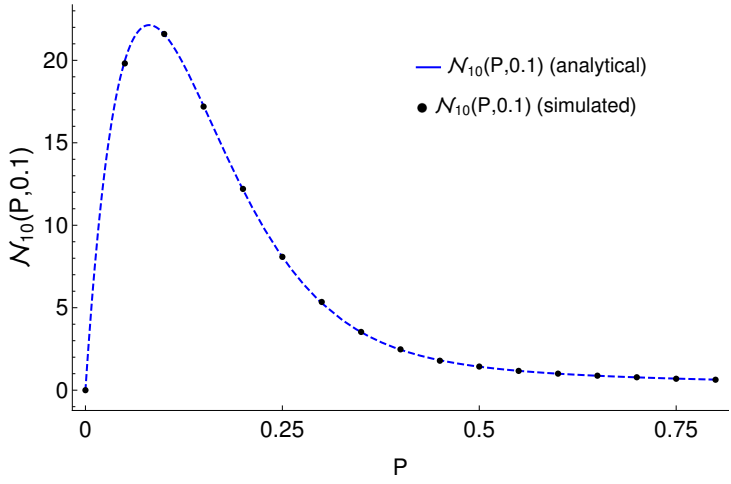

Figure 7.7: The number of coastal points $\mathcal{N}_{10}(P, 0)$ in generation $n = 10$ for $\lambda = 2$ and $Q = 0.2$. The numerical results are shown (black dots) together with the theoretical prediction (7.10) (blue, dashed line). The numerical results were averaged over 20000 runs.

The fractal dimension D_f can be calculated by considering the increase of the number of coastal points with increasing generation number n, i.e.,

$$D_f = \lim_{n\to\infty} \frac{\ln \mathcal{N}_n(P,Q)}{\ln \lambda^n} = \frac{\ln\left[\lambda(1-S)\right]}{\ln \lambda} = 1 + \frac{\ln(1-S)}{\ln \lambda} \tag{7.11}$$

for deposition on a line. When the substrate is planar ($D = 2$), the above expression (7.11) is augmented by 1. This gives, respectively, $0 < D_f < 1$ and $1 < D_f < 2$ for deposition on a line or on a plane.

7.2.2 The critical exponents of the resulting surface

We now calculate the comparative surface roughness exponent [87] α by considering the following height-height correlation function [86, 88]

$$\langle (h(x) - h(x+r))^2 \rangle \propto r^{2\alpha} \,. \tag{7.12}$$

At distances $r > \lambda^{-1}$, since the deposition probabilities are independent, there is no possible dependence of the height difference on r and $\langle \Delta h^2 \rangle$ has a value which is given only by all the possible combinations: hole-hill, hole-nothing, hill-nothing. With increasing number of generations the number of combinations

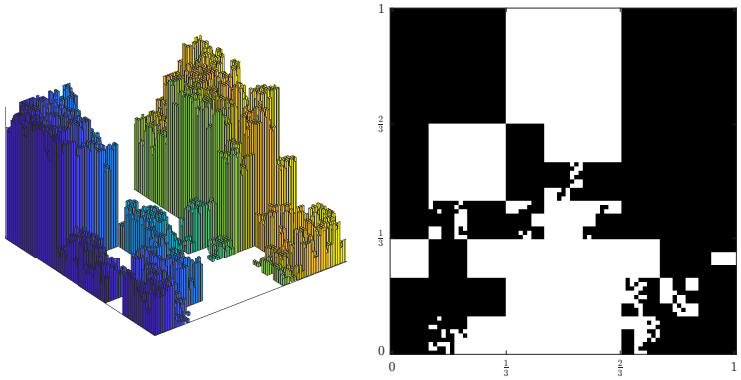

Figure 7.8: Cityscape created by "flooding" the $\lambda = 3$, $n = 4$ landscape to a height $h = 0$ (left panel) and a top-down view of the resulting islands and coastlines (right panel). Parameters are $P = 0.5$ and $Q = 0.3$.

at each site increases; the height difference also increases but saturates as well to a value proportional to the total height (or depth). For shorter distances $r < \lambda^{-1}$ there are two possibilities for the height after the first generation: either they can be the same or differ by λ^{-1} or $2\lambda^{-1}$, depending on whether the two points separated by r are on the same block or not. The r-dependence of the height originates from the probability whether two points separated by a distance r are on the same block or not, and this probability is proportional to r. Hence, $\langle \Delta h^2 \rangle \sim r$. A similar reasoning can be made for $\lambda^{-2} < r < \lambda^{-1}$ and for all the other intervals. We can conclude that $\alpha = 1/2$ but that the slope changes at λ^{-1}, λ^{-2}, λ^{-3} and so on. Hence, a fine structure emerges in the correlation, where the time evolution can be interpreted as successive magnifications, revealing more and more of this structure. This is shown in Figures C.3 and C.4 in the appendix C for respectively $\lambda = 3$ and $\lambda = 2$.

We have calculated the value of the roughness exponent α for $P = 0.7$, $Q = 0$ and $\lambda = 3$ in generation $n = 6$, which results in $\alpha = 0.4935 \pm 0.0006$ and which is close to the theoretically predicted value of $1/2$. It should be noted that this roughness exponent is a power law of the length from the beginning of the deposition process and consequently there is no initial growth that can be found as a power law of time. Hence, exponents β or z are nonexistent in this model.

These results are in stark contrast with the well-known models of random deposition and ballistic deposition where the exponents β and z do exist [2, 3, 89, 90]. In these deposition models it is assumed that all of the particles are of unit size and identical. While there have been studies on properties of surfaces resulting from the deposition of particles with varying size [91], none

consider the hyperbolic scaling and the simultaneous increase of the number of columns on the substrate. There are two fundamental differences between the current model model and these preexisting models. First, the former model is *synchronous*, meaning that all columns are visited simultaneously (i.e., in one generation), while other deposition models consider one particle being deposited at a time, updating time $t \to t + 1$ when on average each column has been visited once. In the HRDM model, the probabilities P and Q control the number of deposition events in one generation. Second, in the HRDM, the number of available columns increases as λ^n for increasing generations n. This signifies that we cannot define a uniform "time" such as for the regular random deposition that is studied in the literature.

7.2.3 Percolation in the one-dimensional HRDM

Consider the hierarchical deposition model where now the hills are made of some conductive material such as copper or zinc, and an electric current is allowed to pass through the system from end to end. The substrate is assumed to be a perfect insulator. We now investigate whether a current is able to flow between the two endpoints and when a spanning cluster of conducting hills appears for the first time. This turns out to be connected to the discussion of the previous section(s). We only consider percolation on a one-dimensional substrate. In [92], the calculation for a two-dimensional substrate is performed in a real space renormalization group approach.

Percolation manifests itself when an uninterrupted chain of conducting hills is placed between the left and right sides of the unit interval $[0, 1]$. This can be realised in every generation $n > 0$. Note that when in generation n a hole is dug on a segment which did not experience any deposition up to order $n - 1$, percolation is made impossible for every generation number exceeding n. The probability to have reached percolation in generation n or earlier is denoted by $\mathcal{P}_n(P, Q)$. We give here the example of $\lambda = 3$ but the results are valid for general $\lambda \geq 2$.

- Percolation in $n = 0$ will be nonexistent. We assume the substrate is initially flat and has not experienced any deposition. Hence, by construction, $\mathcal{P}_0(P, Q) = 0$.
- Percolation in $n = 1$. The only possibility for percolation already in the first step is when all $\lambda = 3$ lattice sites are filled. So, $\mathcal{P}_1(P, Q) = P^3$.
- Percolation in $n = 2$. Here are three possibilities: either 0, 1 or 2 hills have been deposited in the first generation, as shown in Fig.7.9.

The total percolation probability is the probability that percolation has already occurred in the previous generation added to the probability that percolation occurs in this generation, i.e.,

$$\mathcal{P}_2(P,Q) = P^3 + 3P^2(1-S)P^3 + 3P(1-S)^2P^6 + (1-S)^3P^9\,. \quad (7.13)$$

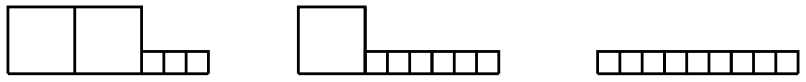

(a) (b) (c)

Figure 7.9: (a) A possible configuration in which percolation is achieved when two blocks were deposited in $n = 1$, with associated probability $3P^2(1-S)P^3$. (b) Possible percolation when one block has been deposited, with probability $3P(1-S)^2P^6$. (c) Possible percolation when no blocks have been deposited, with probability $(1-S)^3P^9$.

- Percolation in $n = 3$. Some of the different possibilities are shown graphically in the appendix C. The percolation probability is

$$\begin{aligned}\mathcal{P}_3(P,Q) &= \sum_{k=0}^{3}\binom{3}{k}P^{3-k}(1-S)^k\sum_{i=0}^{3k}\binom{3k}{i}P^{3k-i}(1-S)^iP^{3i} \\ &= \sum_{k=0}^{3}\sum_{i=0}^{3k}\binom{3}{k}\binom{3k}{i}P^{-(k+i)}(1-S)^{k+i}P^{3(k+i)}\,.\end{aligned} \quad (7.14)$$

For general λ, the probability of percolation in $n = 3$ is given by

$$\begin{aligned}\mathcal{P}_3(P,Q) &= \sum_{k=0}^{\lambda}\binom{\lambda}{k}P^{\lambda-k}(1-S)^k\sum_{i=0}^{\lambda k}\binom{\lambda k}{i}P^{\lambda k-i}(1-S)^iP^{\lambda i} \\ &= \sum_{k=0}^{\lambda}\sum_{i=0}^{\lambda k}\binom{\lambda}{k}\binom{\lambda k}{i}P^{-(k+i)}(1-S)^{k+i}P^{\lambda(k+i)}\,.\end{aligned} \quad (7.15)$$

This can now be repeated for general n and λ to result in the following expression for the percolation probability

$$\mathcal{P}_n(P,Q) = P^{\lambda}\sum_{k_1=0}^{\lambda}\sum_{k_2=0}^{\lambda k_1}\cdots\sum_{k_{n-1}=0}^{\lambda k_{n-2}}\prod_{i=k_{n-1}}^{k_1}\binom{\lambda k_{i-1}}{i}\left[P^{\lambda-1}(1-S)\right]^{\sum_{j=1}^{n-1}k_j}\,. \quad (7.16)$$

The nested summations in (7.16) indicate the strong memory effect pertaining to the history of deposition in previous generations. Working out the above expressions explicitly starting with $\mathcal{P}_0 = 0$ gives

$$\begin{aligned}
\mathcal{P}_1(P,Q) &= P^\lambda \\
\mathcal{P}_2(P,Q) &= \left(P + (1-S)P^\lambda\right)^\lambda \\
\mathcal{P}_3(P,Q) &= \left(P + (1-S)\left(P + (1-S)P^\lambda\right)^\lambda\right)^\lambda \\
&\vdots \\
\mathcal{P}_n(P,Q) &= \left(P + (1-S)\mathcal{P}_{n-1}(P,Q)\right)^\lambda \,.
\end{aligned} \tag{7.17}$$

The fixed point of the recurrence equation (7.17) can be computed analytically for low values of λ and numerically for larger values. In Fig. 7.10 and 7.11, the first 100 iterations are shown for $\lambda = 2$ and $\lambda = 3$ with $Q = 0$ together with numerically simulated results for $n = 11$ averaged over 20000 realisations. Note that a singularity in the derivative develops at some values for P, which is reminiscent of a first-order phase transition.

The asymptotic behaviour for large n of the recurrence relation (7.17) can be studied by considering a complementary problem for the hierarchical deposition model. Let us study the distribution of *empty* intervals in generation n. We can identify the process of depositing a hill or an empty space with a rooted tree [93] where each vertex has λ children and we select edges with probability $1 - S$. The probability that a vertex has exactly k children (i.e., empty disjoint subsets) is therefore

$$\xi_k = \binom{\lambda}{k}(1-S)^k P^{\lambda-k} \,, \tag{7.18}$$

so the expected number μ of empty subsets after one generation is

$$\begin{aligned}
\mu &= \sum_{k=0}^{\lambda} k\binom{\lambda}{k}(1-S)^k P^{\lambda-k} \\
&= \lambda(1-Q)^{\lambda-1}(1-S)\,.
\end{aligned} \tag{7.19}$$

We now define the stochastic variable X_n as the number of vertices in generation n, with probability distribution $\mathbb{P}(X_n)$. The probability for a percolation cluster to form in generation n is equal to the probability that the number of vertices for the branching process is equal to zero, i.e., there are no remaining empty

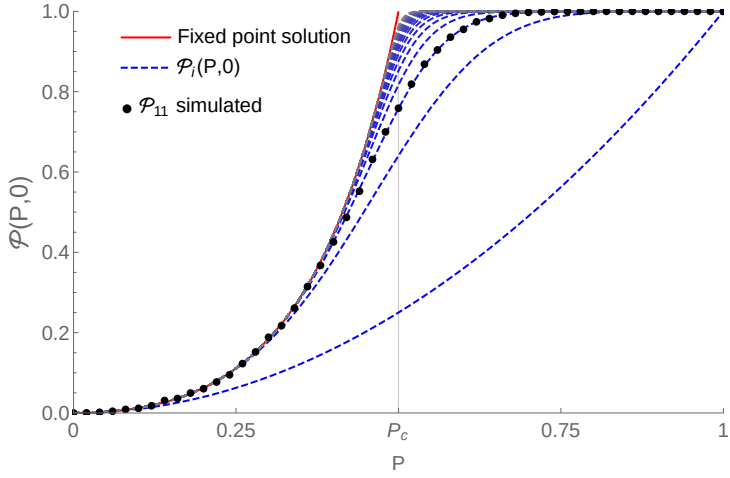

Figure 7.10: Percolation probability for $\lambda = 2$ and $Q = 0$. The fixed-point solution is shown (red line) together with the percolation probabilities $\mathcal{P}_i$ for the first 100 generations in steps of five (blue, dashed lines) in ascending order, starting with $n = 1$, and the simulated results for generation $n = 11$ (black circles).

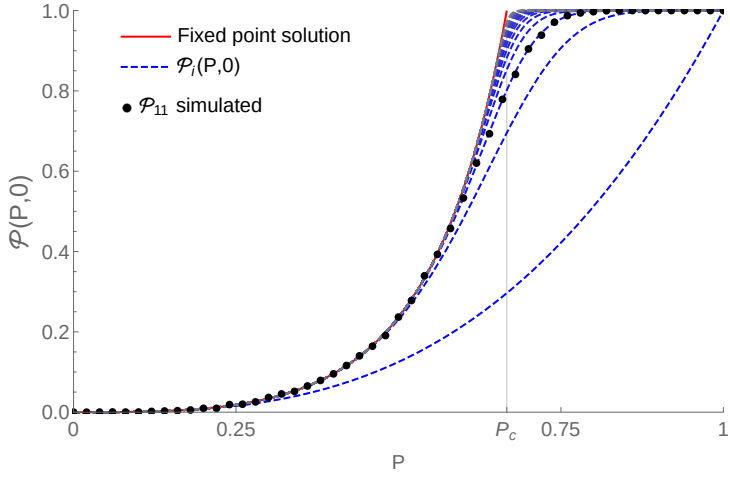

Figure 7.11: Percolation probability for $\lambda = 3$ and $Q = 0$. The fixed-point solution is shown (red line) together with the percolation probabilities $\mathcal{P}_i$ for the first 100 generations in steps of five (blue, dashed lines) in ascending order, and the simulated results for generation $n = 11$ (black circles).

subsets. Therefore, the connection between the original percolation problem and the complementary problem can be expressed as follows

$$\mathcal{P}_n(P,Q) = \mathbb{P}(X_n = 0)\,. \tag{7.20}$$

To calculate the probability $\mathbb{P}(X_n = 0)$, we define the following generating function f for the sequence $\{\xi_k\}$,

$$\begin{aligned} f(x) &= \sum_{k=0}^{\lambda} \xi_k x^k \\ &= \sum_{k=0}^{\lambda} x^k \binom{\lambda}{k} (1-S)^k P^{\lambda-k} \\ &= (P + (1-S)x)^{\lambda}\,. \end{aligned} \tag{7.21}$$

Note that this generating function has the same functional form as the recurrence relation (7.17). Furthermore, it follows that $f(0) = P^{\lambda}$, $f(1) = (1-Q)^{\lambda}$ and $f'(1) = \mu$. Now, define the conditional probabilities $\xi_j^{(n)} = \mathbb{P}(X_n = j | X_0 = 1)$. The generating function for this new process is

$$F_n = f^{(n)} \equiv f \circ f \circ ... f\,, \tag{7.22}$$

which is the n-fold composition of the generating function f with itself. Therefore, assuming that $X_0 = 1$, the probability $\mathbb{P}(X_n = 0)$ is the following function

$$\mathbb{P}(X_n = 0) = f^{(n)}(0)\,. \tag{7.23}$$

This implies that for $n \to \infty$ the iteration converges to the first fixed point of $f(x)$ that is reached when starting from $x = 0$. If $\mu \leq 1$, the sequence converges to 1, indicating percolation while for $\mu > 1$ the iteration converges to another fixed point. Hence, the percolation threshold P_c can be calculated as follows

$$P_c = 1 - Q - \frac{(1-Q)^{1-\lambda}}{\lambda}\,, \tag{7.24}$$

and for $Q = 0$ this reduces to

$$P_c = 1 - \frac{1}{\lambda}\,. \tag{7.25}$$

For $\lambda = 2$ and $\lambda = 3$, the percolation thresholds are, respectively, $P_c = 1/2$ and $P_c = 2/3$, as can be seen in Fig. 7.10 and 7.11. Note that the above threshold value (7.25) is the same value as was found for S in the previous section, for the separation point between the Euclidean and the fractal regimes for the number

of coastal points. Since now $Q = 0$, $S = P = P_c$ is precisely the condition for logarithmic fractality.

This coincidence can be understood from the following correspondence. When percolation occurs, the sea level is covered with conducting blocks, which, on average, inhibit the formation of new coastal points and, at the same time, destroy existing coastal points. For $P > P_c$ and $n \to \infty$, percolation is almost certainly achieved and the number of coastal points enters the Euclidean regime where it saturates on average to a constant value $\gamma < 1$, as shown in Section 7.2.1 and Appendix C. This γ is the following number (for $Q = 0$):

$$\gamma = \frac{2\lambda(\lambda-1)(1-P)^2(1-P+P^2)}{\lambda-1+P}\,. \tag{7.26}$$

For $P \leq P_c$, the number of coastal points grows either exponentially, for $P < P_c$, or linearly, for $P = P_c$. However, for $P > P_c$ this number effectively becomes zero, as can be seen in Fig. 7.12 for different values of λ. In this regime, the number of coastal points vanishes, since its asymptotic average is $\gamma \ll 1$ (in a statistical sense) and percolation is almost certainly achieved. This explains the precise correspondence between coastal-point non-proliferation and percolation.

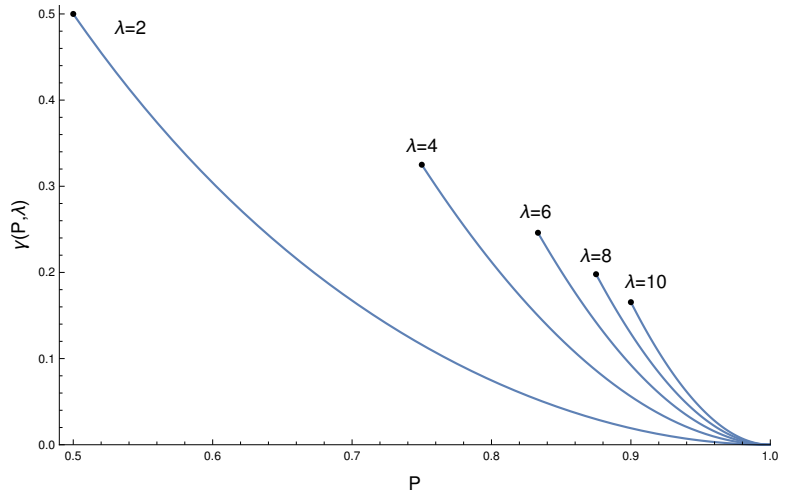

Figure 7.12: The constant γ describing the asymptotic average of the number of coastal points for $P > P_c$ for $\lambda \in \{2, 4, 6, 8, 10\}$. The black dots indicate $P = P_c$ for each value of λ.

The calculation involving the rooted tree of empty subsets can be directly mapped to the study of the random Cantor set [94, 95]. The above results are valid for $Q = 0$. When $Q > 0$, the probability for a percolation cluster to form

is never equal to one so a percolation threshold is nonexistent. Therefore, a singularity is absent for the fixed point of the recurrence relation (7.17).

The functional form of the solution of equation (7.17) for $P \leq P_c$ can be directly calculated by finding the fixed-point solution $\mathcal{P}_\infty$, which is possible for low values of λ. Note that $\mathcal{P}_\infty = 1$ is the trivial fixed-point solution for $P \geq P_c$. We will denote the nontrivial solution by $\theta_\lambda(P)$ and we assume $Q = 0$. Hence, for $\lambda = 2$, the nontrivial solution $\theta_2(P)$ of

$$\mathcal{P}_\infty = \left(P + (1-P)\mathcal{P}_\infty\right)^2 \tag{7.27}$$

is

$$\theta_2(P) = \left(\frac{P}{1-P}\right)^2, \tag{7.28}$$

while for $\lambda = 3$, the nontrivial solution $\theta_3(P)$ is

$$\theta_3(P) = 1 - \frac{3}{2(1-P)} + \frac{1}{2}\sqrt{\frac{1+3P}{(1-P)^3}}\,. \tag{7.29}$$

We now study the critical behaviour at P_c, which we expect to have the asymptotic form

$$1 - \theta_\lambda(P) \sim c(P_c - P)^\beta\,, \qquad P \uparrow P_c \tag{7.30}$$

for some $c > 0$ and $\beta > 0$. The critical behaviour of the solution at the fixed point can be found by expanding θ_λ about the percolation threshold, i.e.,

$$\begin{aligned}
\theta_2(P) &= 1 + 8(P - P_c) + \mathcal{O}((P - P_c)^2) \\
\theta_3(P) &= 1 + 9(P - P_c) + \mathcal{O}((P - P_c)^2) \\
\theta_4(P) &= 1 + \frac{32}{3}(P - P_c) + \mathcal{O}((P - P_c)^2) \\
&\vdots \\
\theta_\lambda(P) &= 1 + \frac{2\lambda^2}{\lambda - 1}(P - P_c) + \mathcal{O}((P - P_c)^2)\,.
\end{aligned} \tag{7.31}$$

Hence, the critical exponent $\beta = 1$ is obtained. This singularity is reminiscent of a first-order phase transition in view of the jump in the first derivative of $\mathcal{P}_\infty(P)$ at P_c.

7.2.4 Percolation with alternating deposition probabilities

It is possible for the hills (and holes) to originate from different sources, thereby changing the resulting landscape. First, we will study one such system where two sources of deposition are present and for which the characteristic length scales remain the same, i.e., $\lambda_1 = \lambda_2 = \lambda$. This has previously been studied in the context of evolving landscapes in the periodical extension of the hierarchical deposition model and logarithmic fractal geometry was confirmed [96]. As an extension of this previous study, we now explore percolation properties. We consider two sources with deposition probabilities (P_1, Q_1) and (P_2, Q_2).

Repeating the calculations from the previous section 7.2.3, now with alternating probabilities, it is straightforward to see that the percolation probability $\mathcal{P}_n(P_1, Q_1, P_2, Q_2)$ for the first four generations is given by, with $S_i = P_i + Q_i$,

$$\begin{aligned}
\mathcal{P}_1(P_1, Q_1, P_2, Q_2) &= P_1^{\lambda} \\
\mathcal{P}_2(P_1, Q_1, P_2, Q_2) &= \left[P_1 + P_2^{\lambda}\,(1 - S_1)\right]^{\lambda} \\
\mathcal{P}_3(P_1, Q_1, P_2, Q_2) &= \left[P_1 + (1 - S_1)\left(P_2 + P_1^{\lambda}(1 - S_2)\right)^{\lambda}\right]^{\lambda} \\
\mathcal{P}_4(P_1, Q_1, P_2, Q_2) &= \left[P_1 + (1 - S_1)\left(P_2 + (1 - S_2)\left(P_1 + P_2^{\lambda}(1 - S_1)\right)^{\lambda}\right)^{\lambda}\right]^{\lambda}.
\end{aligned} \tag{7.32}$$

Generalising this procedure, the percolation probability for generation n is then

$$\mathcal{P}_n(P_1, Q_1, P_2, Q_2) = \left[P_1 + (1 - S_1)\left(P_2 + (1 - S_2)\mathcal{P}_{n-2}\right)^{\lambda}\right]^{\lambda}. \tag{7.33}$$

From this expression one can see that when $P_1 = P_2 = P$ and $Q_1 = Q_2 = Q$ the percolation probability reduces to that of the uniform hierarchical random deposition model (7.17). Continuing as in the previous section, the expected number of empty subsets can be calculated in a similar manner, i.e.,

$$\begin{aligned}
\mu &= \sum_{k=0}^{\lambda} \binom{\lambda}{k} P_1^{\lambda-k}(1 - S_1)^k \sum_{i=0}^{\lambda k} i \binom{\lambda k}{i} P_2^{\lambda k - i}(1 - S_2)^i \\
&= \lambda^2(1 - S_1)(1 - S_2)\left((1 - Q_2)\left(P_1 + (1 - S_1)(1 - Q_2)^{\lambda}\right)\right)^{\lambda - 1}.
\end{aligned} \tag{7.34}$$

From equation (7.34) the percolation threshold can once again be calculated for either P_1 or P_2. With $Q_1 = Q_2 = 0$, the percolation threshold becomes

$$P_{1,c} = 1 - \frac{1}{\lambda^2(1 - P_2)}. \tag{7.35}$$

For P_2 a multiple of P_1, i.e., for $P_2 = rP_1$, $r \in \mathbb{R}^+$, the percolation threshold is

$$P_{1,c} = \frac{r+1}{2r} - \sqrt{\frac{1}{r\lambda^2} + \left(\frac{r-1}{2r}\right)^2}. \tag{7.36}$$

Notice that this expression reduces to the percolation threshold (7.25) for the uniform random deposition model when $r = 1$. In Fig. 7.13, the percolation probability is shown for the first 100 iterations of the alternating model with $\lambda = 3$ together with the fixed-point solution. The percolation threshold is $P_{1,c} = 7/9$ and the numerically simulated results for $n = 11$ are averaged over 20000 realisations. The probability to dig a hole is assumed to be zero for both sources, i.e., $Q_1 = Q_2 = 0$, while the probability to deposit a hill in the second generation is fixed at the value $P_2 = 1/2$.

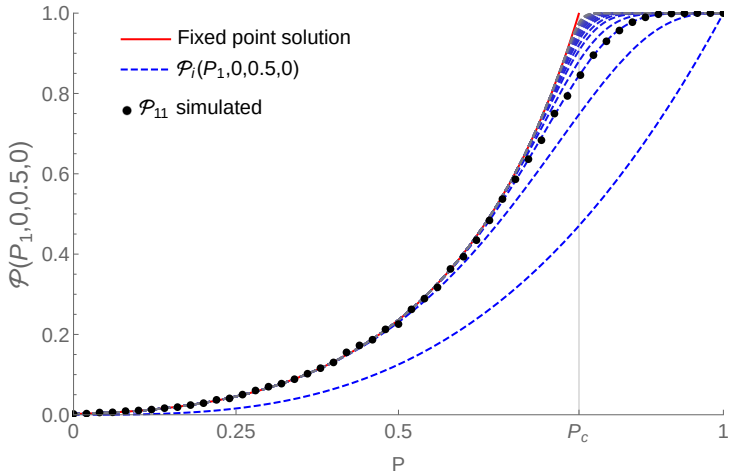

Figure 7.13: Percolation probability $\mathcal{P}_n(P_1, Q_1, P_2, Q_2)$ for alternating deposition probabilities with $\lambda = 3$, $Q_1 = Q_2 = 0$ and $P_2 = 1/2$, as a function of $P \equiv P_1$. The fixed-point solution is shown (red line) together with the percolation probabilities for the first 100 generations in steps of five (blue, dashed lines) in ascending order, and the simulated results for $n = 11$ (black circles).

7.2.5 Percolation with alternating rescaling factors

We now assume the probabilities (P, Q) to be constant but take the characteristic length rescaling factors λ_1 and λ_2 to be different, as was initially proposed in

[97]. The percolation probability for the first three generations can be calculated in the same manner as before, resulting in

$$\begin{aligned}
\mathcal{P}_1(P,Q,\lambda_1,\lambda_2) &= P^{\lambda_1} \\
\mathcal{P}_2(P,Q,\lambda_1,\lambda_2) &= \left[P + P^{\lambda_2}\,(1-S)\right]^{\lambda_1} \\
\mathcal{P}_3(P,Q,\lambda_1,\lambda_2) &= \left[P + (1-S)\left(P + P^{\lambda_1}(1-S)\right)^{\lambda_2}\right]^{\lambda_1} .
\end{aligned} \tag{7.37}$$

The percolation probability for generation n can be found by continuing the above sequence

$$\mathcal{P}_n(P,Q,\lambda_1,\lambda_2) = \left[P + (1-S)\left(P + (1-S)\mathcal{P}_{n-2}\right)^{\lambda_2}\right]^{\lambda_1} , \tag{7.38}$$

which reduces to the uniform random deposition model for $\lambda_1 = \lambda_2 = \lambda$. The average number of empty subsets after one generation, μ, is given by

$$\begin{aligned}
\mu &= \sum_{k=0}^{\lambda_1} \binom{\lambda_1}{k} P^{\lambda_1-k}(1-S)^k \sum_{i=0}^{\lambda_2 k} i \binom{\lambda_2 k}{i} P^{\lambda_2 k - i}(1-S)^i \\
&= \lambda_1\lambda_2(1-S)^2(1-Q)^{\lambda_2-1}\left(P + (1-S)(1-Q)^{\lambda_2}\right)^{\lambda_1-1} .
\end{aligned} \tag{7.39}$$

The percolation threshold P_c can be calculated by solving $\mu = 1$ for P, i.e.,

$$P_c = 1 - \frac{1}{\sqrt{\lambda_1\lambda_2}} , \tag{7.40}$$

which reduces to the formerly calculated expression (7.25) in the uniform random deposition model in which the rescaling factors are equal, $\lambda_1 = \lambda_2 = \lambda$. Note that for the calculation of the percolation threshold the roles of λ_1 and λ_2 in (7.39) can be freely interchanged.

In Fig. 7.14, the percolation probability is shown for $\lambda_1 = 2$ and $\lambda_2 = 3$ together with the fixed-point solution of the corresponding recurrence relation (7.38) and numerically simulated results for $n = 11$ averaged over 20000 realisations. The percolation threshold $P_c = 1 - 1/\sqrt{6}$ is also shown.

7.3 Hierarchical ballistic deposition

Consider a one-dimensional substrate of length one, i.e., the interval $[0, 1]$ and a rescale factor $\lambda \in \mathbb{N}$, where $\lambda \geq 2$. In the first generation we divide the interval

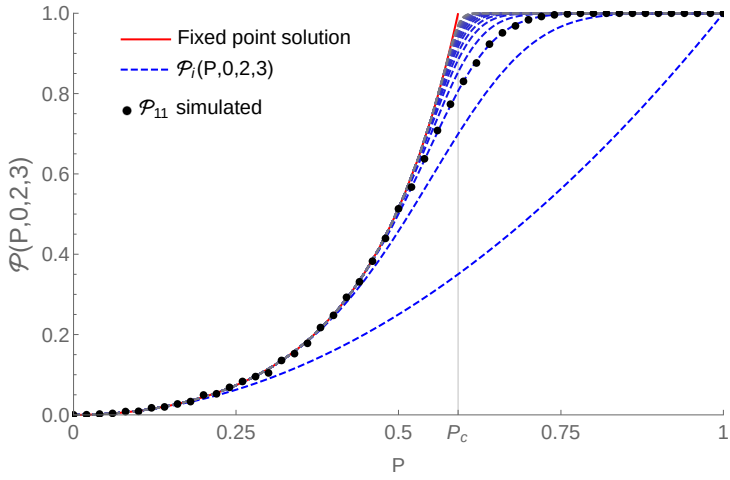

Figure 7.14: Percolation probability $\mathcal{P}_n(P, Q, \lambda_1, \lambda_2)$ for alternating rescaling factor deposition with $\lambda_1 = 2$, $\lambda_2 = 3$, $Q = 0$. The fixed-point solution is shown (red line) together with the percolation probabilities for the first 100 generations in steps of five (blue, dashed lines) in ascending order, and the simulated results for $n = 11$ (black circles).

in λ segments of length λ^{-1} and either deposit a square particle of side λ^{-1} with probability P or do nothing with probability $1 - P$ and move to the next segment. If we choose to deposit a particle, there is a probability Γ that it is sticky and attaches itself to the side of the highest column next to it. This is illustrated in Fig. 7.15. If the particle is not sticky, it is deposited on the lowest segment in the column where it was dropped. Hence, the compound probability of depositing a sticky or a regular particle in a column is respectively $P\,\Gamma$ and $P\,(1 - \Gamma)$. For now, let us only consider the case where no holes are deposited ($Q = 0$). A possible realisation of the sixth-generation hierarchical landscape is shown in Fig. 7.16 for $\lambda = 3$. We name this model the hierarchical *ballistic* deposition model (HBDM), by analogy with the well-known ballistic deposition model. Note that the HBDM is still a random model but with nonzero correlation between different columns.

Sticking to another particle from the same generation is not allowed. This would induce a reflection symmetry breaking in the horizontal direction due to the computational deposition rules, i.e., left-to-right deposition. However, if one does change the rules slightly to permit simultaneous deposition on all sites, neighbouring particles can aggregate before being deposited and collectively attach on the left, right, or both sides to the substrate. We will not study such

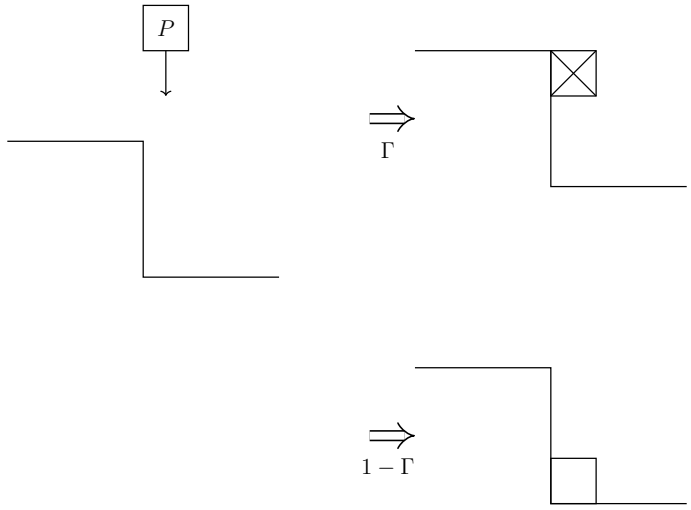

Figure 7.15: The possibilities for a particle to be deposited with a probability P. Either the particle sticks to the material already present at the left with probability Γ or is deposited at the bottom of the column with probability $1-\Gamma$. We denote a protruding particle with a crossmark.

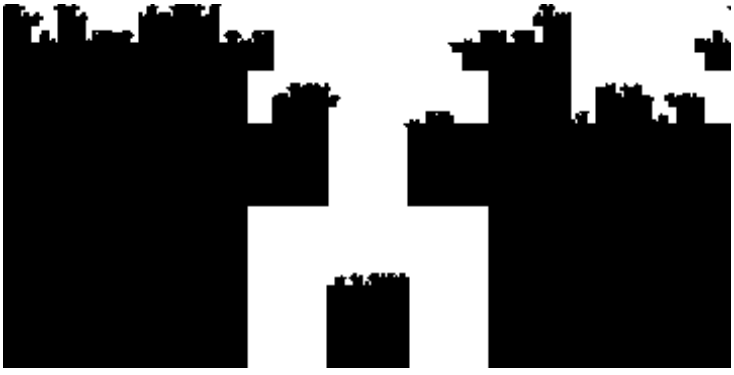

Figure 7.16: Landscape resulting from the HBDM with $\lambda = 3$, $P = 0.6$, $Q = 0$, $\Gamma = 0.75$ and $n = 6$. Periodic boundary conditions are imposed, which identify the left and right sides.

systems in this thesis.

We can now study the logarithmic fractal character of the resulting surface by developing an analytic expression for the surface length increment in generation n, i.e, ΔL_n. Note that the length increment arises from the creation of vertical *walls* or *cliffs* and horizontal *plateaus*. We will study each separately. To calculate the vertical length increment $\Delta V_n^{(0)}$ due to the creation of new walls, note that this can either originate from the placement of a vertical wall on a point between two segments of equal height, or by converting a preexisting cliff by the placement of particles next to it. For generation n, this can be calculated to be

$$\begin{aligned}\Delta V_n^{(0)} = \lambda^{-n} \sum_{i=1}^{\lambda^n} 2P(1-P) \left[1 - W_i^{(n-1)} - C_i^{(n-1)}\right] \\ + \lambda^{-n} \sum_{i=1}^{\lambda^n} P^2 \, \Gamma \, C_i^{(n-1)} ,\end{aligned} \tag{7.41}$$

where $W_i^{(n-1)}$ and $C_i^{(n-1)}$ are respectively the probability that point i was occupied by at least one wall or cliff in any of the previous $n-1$ generations. The sum over $W_i^{(n-1)}$ in equation (7.41) is the average number of points occupied by at least one wall after $n-1$ generations. This is equal to the number of new walls summed over all of the generations up to and including $n-1$, i.e.,

$$\sum_{i=1}^{\lambda^n} W_i^{(n-1)} = \sum_{m=1}^{n-1} \lambda^m \Delta V_m^{(0)} . \tag{7.42}$$

However, constructing new walls is not the only way to alter the surface length increment. The vertical increment can be increased or decreased by depositing a particle next to a preexisting wall/cliff without creating a new wall/cliff. We call this contribution $\Delta V_n^{(1)}$ and find it to be

$$\begin{aligned}\Delta V_n^{(1)} = \lambda^{-n} \sum_{i=1}^{\lambda^n} P \, \Gamma \, W_i^{(n-1)} \\ + \lambda^{-n} \sum_{i=1}^{\lambda^n} P \left[2 - \Gamma(P+1)\right] C_i^{(n-1)} .\end{aligned} \tag{7.43}$$

The horizontal increment can be increased by $2\lambda^{-n}$ by creating a protrusion through the deposition of a sticky particle. The increment ΔH_n is

$$\Delta H_n = 2\lambda^{-n} \sum_{i=1}^{\lambda^n} P \, \Gamma \, \left[W_i^{(n-1)} + C_i^{(n-1)}\right] . \tag{7.44}$$

Since $\Delta V^{(1)}$ and ΔH do not entail the creation of new walls, they did not appear in equation (7.41). The sum over $C_i^{(n-1)}$ is now the average number of points occupied by at least one cliff after $n-1$ generations. This is equal to the number of new cliffs summed over all of the generations up to and including $n-1$, i.e.,

$$\sum_{i=1}^{\lambda^n} C_i^{(n-1)} = \sum_{m=1}^{n-1} \frac{\lambda^m}{2} \Delta H_m \,, \tag{7.45}$$

where the factor 2 is added because every new protrusion contributes $2\lambda^{-n}$ to the total length and hence this must be divided out. Anticipating that for large n the increments $\Delta V_n^{(0)}$, $\Delta V_n^{(1)}$ and ΔH_n reach constant values $\Delta V_\infty^{(0)}$, $\Delta V_\infty^{(1)}$ and ΔH_∞, we can solve the coupled equations (7.41) and (7.44), resulting in

$$\Delta V_\infty^{(0)} = \frac{2P(1-P)(\lambda-(1-P\Gamma))(\lambda-1)}{(\lambda-1)^2+(2P(1-P)-P\Gamma)\,(\lambda-1)-P^3\Gamma^2} \tag{7.46}$$

$$\Delta H_\infty = \frac{4P^2\Gamma(1-P)(\lambda-1)}{(\lambda-1)^2+(2P(1-P)-P\Gamma)\,(\lambda-1)-P^3\Gamma^2} \,, \tag{7.47}$$

and from these find $\Delta V_\infty^{(1)}$,

$$\Delta V_\infty^{(1)} = \frac{2P^2\Gamma(1-P)\left((\lambda-1)+2P(1-\Gamma)-P^2\Gamma\right)}{(\lambda-1)^2+(2P(1-P)-P\Gamma)\,(\lambda-1)-P^3\Gamma^2} \,. \tag{7.48}$$

Now, the total surface length increment, ΔL_n in generation n, is

$$\Delta L_n = \Delta V_n^{(0)} + \Delta V_n^{(1)} + \Delta H_n \tag{7.49}$$

and for large n this finally becomes the sum of equations (7.46), (7.47) and (7.48)

$$\Delta L_\infty = \frac{2P(1-P)\left((\lambda-1)^2-P^2\Gamma^2(P+2)+2P\Gamma(\lambda-1+P)\right)}{(\lambda-1)^2+(2P(1-P)-P\Gamma)\,(\lambda-1)-P^3\Gamma^2} \,. \tag{7.50}$$

We now compare our analytical result with numerical simulations for $\lambda = 3$. This is shown in Fig. 7.17. One can see that the approximation is already fairly accurate. The increment is skewed towards higher values of P when $\Gamma > 0$. Note that for $\Gamma = 0$, the expression reduces to equation (7.3) that was calculated earlier in [76], i.e., for the HRDM [74].

7.3.1 Void ratio and porosity

For $\lambda = 2$ there exists the possibility to create closed cavities or *voids*, giving rise to a porous structure that has been studied sporadically in the literature,

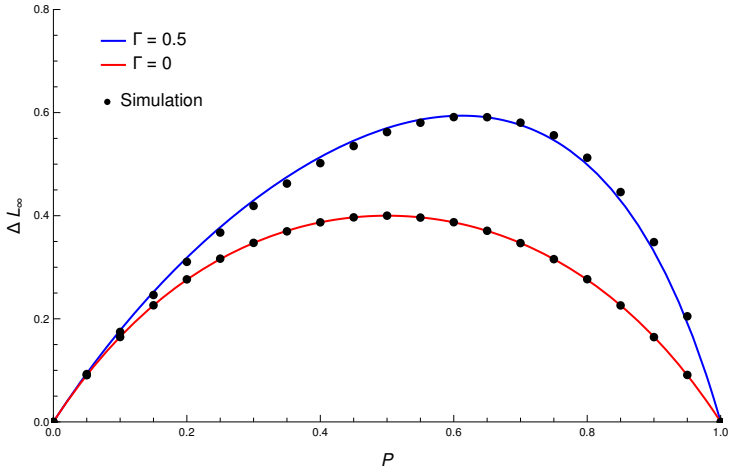

Figure 7.17: The asymptotic length increment ΔL_∞ (7.50) as a function of deposition probability P for $\lambda = 3$. A comparison is made between the HRDM with $\Gamma = 0$ and the HBDM with $\Gamma = 0.5$.

either in the context of deposition models [98, 99] or in a more geophysical context [100, 101]. A possible realisation of such a porous structure is shown in Fig. 7.18 with periodic boundary conditions in the horizontal direction. Note that for $\lambda \geq 3$ there is no possibility to create voids due to the hierarchical construction of the deposition process, as shown in Fig. 7.16.

In the few studies that appear in the literature, the porosity ϕ is either only studied numerically or by a combination of numerical simulation and scaling arguments. Analytical calculations are often unfeasible because of the lateral correlations introduced by the overhanging blocks. We will derive an approximate analytical expression for the total void ratio e, which is equivalent to the porosity ϕ under suitable scaling.

The total saturated void ratio e_∞ for $n \to \infty$ can be calculated as follows

$$e_\infty = \frac{V_v}{V_s}\,, \tag{7.51}$$

where V_v and V_s are respectively the volume (or area when the deposition is on a $D = 1$ substrate) of the voids and the solid matter for $n \to \infty$. The volume of the solid matter V_s is easily calculated to be the total volume of the blocks that are deposited, i.e.,

$$V_s = \sum_{n=1}^{\infty} (P\lambda^n)\lambda^{-2n} = \frac{P}{\lambda - 1}\,. \tag{7.52}$$

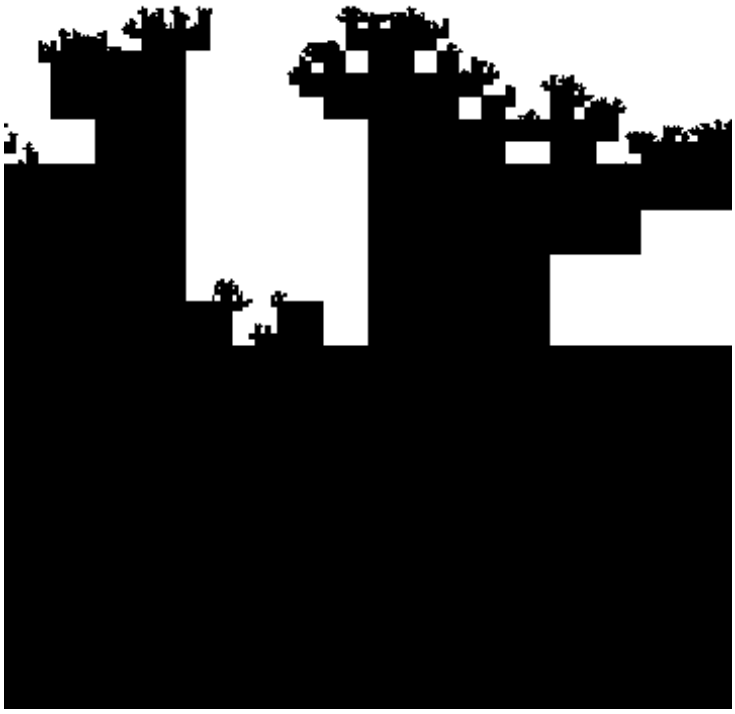

Figure 7.18: Porous structure resulting from the HBDM with $\lambda = 2$, $P = 0.6$, $\Gamma = 0.75$ and $n = 9$. Periodic boundary conditions are imposed, which identify the left and right sides.

Hence, for $\lambda = 2$, this reduces to $V_s = P$. The total volume of the voids V_v is calculated in appendix C. Combining equations (7.51), (7.52) and (C.18), the void ratio e_∞ becomes

$$\begin{aligned} e_\infty = & \frac{P^4\Gamma^3(1-P)^2(1-\Gamma)^2\left(5-2P\Gamma+2P^3\Gamma^2(1-\Gamma)\right)}{3(2-P\Gamma(1-P))(1-2P\Gamma(1-P))(2-P^2\Gamma(1-\Gamma))(1-2P^2\Gamma(1-\Gamma))} \\ & - \frac{P^4\Gamma^3(1-P)^2(1-\Gamma)^2\left(2P^4\Gamma^2(1-\Gamma)+2P^2\Gamma(2-3\Gamma)\right)}{3(2-P\Gamma(1-P))(1-2P\Gamma(1-P))(2-P^2\Gamma(1-\Gamma))(1-2P^2\Gamma(1-\Gamma))} \\ & + \frac{P^2\Gamma(1-P)(1-\Gamma)^2}{6(1-P^2\Gamma(1-\Gamma))(4-P^2\Gamma(1-\Gamma))} + \frac{P^2\Gamma(1-P)}{2}\,. \end{aligned} \tag{7.53}$$

The void ratio e and the porosity ϕ are connected through the following equation, which amounts to a simple rescaling

$$\phi = \frac{e}{1+e}\,. \tag{7.54}$$

Fig. 7.19 shows the saturated porosity as a function of P and Γ, together with numerical simulations averaged over 5000 realisations of the process. The void volume (or area in two dimensions) V_v is found by a 2-pass connected component labelling algorithm to find nearest-neighbour connected components. It is clear that the combination of equation (7.54) with (7.53) already yields a decent approximation for the numerical results.

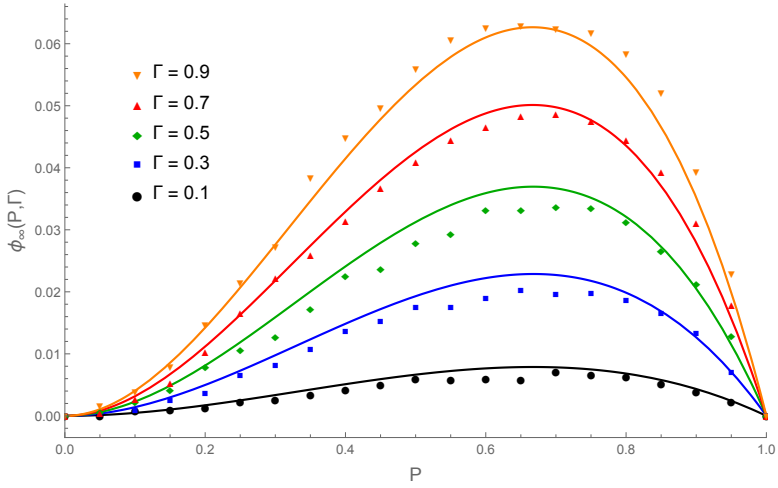

Figure 7.19: Porosity of the HBDM for $\lambda = 2$ and $n = 8$. The dependency on the deposition probability P is shown for different values of $\Gamma \in \{0.1, 0.3, 0.5, 0.7, 0.9\}$. The results are averaged over 5000 realisations for each data point. The lines are the analytical predictions for the porosity, obtained by combining equations (7.53) and (7.54).

Additional numerical results for the roughness exponent and the percolation probability in the HBDM are given in appendix C, sections C.3 and C.4 respectively.

Chapter 8

Conclusions

8.1 BLUES function method

For ODEs, FDEs, PDEs and CDEs, the BLUES function method was set up and analytical approximants were calculated for a plethora of (physical) problems. While the original setup for the method was situated in the realm of ODEs, the method was successfully extended to incorporate PDEs and CDEs by reinterpreting the role of the inhomogeneous source as a vector of external sources emerging from a set of initial conditions.

For ODEs, the method has been applied in chapter 3 to four equations that possess travelling wave solutions, albeit with different structure and boundary conditions. The first equation was the Camassa-Holm ODE without dispersion and with a comoving external source, combined with Dirichlet boundary conditions that decay at both positive and negative infinity. This equation possesses travelling wave solutions that have the form of a soliton. Next, the Burgers equation with both a symmetrical and asymmetrical source with respectively norm unity and zero was studied. This equation is complemented by Neumann boundary conditions where the derivative decays at both positive and negative infinity. This results in respectively kink and solitonic solutions for the symmetrical and asymmetrical external source, which was verified using a sum rule for the nonlinear ODE. A third example pertained to the nonlinear oscillator equation with Dirichlet boundary conditions whereby the solution exhibits oscillatory behaviour within a travelling wave envelope curve. For these three systems, the BLUES method was capable of generating analytic approximants to the solutions with a high degree of accuracy while also correctly

capturing the asymptotic behaviour, converging *globally* to the (numerically) exact solution. A final example, the Fisher equation with the same Neumann boundary conditions as the Burgers equation was studied and it was found that the approximants converged locally to the exact solution, while diverging for large negative values of the coordinate.

The method was subsequently applied to a FDE in chapter 4 that originated from the study of heat propagation in a semi-infinite solid with nonlinear cooling. It was found that the original formulation of the BLUES function method for ODEs is valid if one can find the Green function for the associated fractional linear equation. A first thorough comparison with the ADM was performed which indicated that the BLUES function method possesses a larger region of convergence than the ADM, while the latter requires either more iterations or subsequent manipulations of the results to achieve the same level of convergence.

Following the successful application of the BLUES function method to the field of ODEs and FDEs, we extended it to PDEs with a first-order time derivative by assuming that the initial condition fulfils the role of the source by multiplication with a Dirac point source located at $t = 0$. This was consequently applied in chapter 5 to a nonlinear reaction-diffusion-convection equation, a porous medium equation and the nonlinear Black-Scholes equation for testing purposes. It was established that the BLUES method can effectively generate a sequence that often converges faster to the exact solution than similar methods. Next, the method is employed to study the solution of a heuristic equation that describes the evolution of interfacial profiles through the combined effects of nonlinear growth and lateral shear. A Gaussian and a space-periodic initial condition were studied separately. It was found that although a first approximation is already a good approximation, higher iterations quickly become unfeasible. This first approximant coincides with a perturbative solution where the perturbation parameters are small and of the same order of magnitude. However, for the space-periodic initial condition, higher approximants were easily calculated and it was established that the BLUES function method is able to accurately reproduce the asymptotic behaviour of the Fourier coefficients of the solution while other methods and perturbation theory either diverge drastically or converge to a different value.

In the last chapter on the BLUES function method, i.e., chapter 6, we first extended the method to systems of coupled ordinary differential equations by considering an associated linear system that already possesses the fixed points of the full nonlinear system, resulting in a powerful iterative procedure for finding the exact solution. This was applied to the well-known SIRS and SEIRS models with constant vaccination strategies. By means of a thorough comparison with the ADM, VIM and HPM it was established that the BLUES function method is able to generate approximants that converge fast to the

numerically exact solution, in both the disease-free and endemic equilibrium. When the parameter R_V that controls the asymptotic behaviour is tuned to a dynamical critical point, it was shown that one can take a step back and choose the linear operator to only include the disease-free equilibrium, once again producing useful results. Finally, the BLUES method was extended to PDEs with higher-order time derivatives or, equivalently, systems of coupled partial differential equations by combining the concept whereby the initial condition can be included through multiplication with a point source and the matrix BLUES function method. This was illustrated by applying the new formulation of the method to a nonlinear telegrapher's equation with a second-order time derivative.

8.1.1 Perspectives and future research

One can imagine a myriad of extensions and applications for the different formulations of the BLUES function method. A possible extension of the method pertains to stochastic differential equations (SDEs), where the role of the source can be assumed by a stochastic noise and the approximants can for example be used to calculate the cumulants or moments of the solution. Such an extension to SDEs is especially interesting for the domain of interface growth, where the seminal KPZ equation involves diffusion, nonlinear growth and stochasticity. A direct example comes to mind concerning the interface problem studied in chapter 5. There it was assumed that the interface profile was derived from a deterministic KPZ equation. In the future, this could be extended to include a (possibly delta-correlated) noise term.

Possible extensions of the BLUES method aside, it can be noted that it is of practical use in many fields of science and technology. One concrete application is the characterisation of the potential of a pn-junction in semiconductor physics, which can be described in terms of a nonlinear Poisson equation. A first reconnaissance study has been conducted in the Master's thesis of Thierry Rondagh [102], which I co-supervised. This equation possesses an exponential nonlinearity, which presents some problems when the exponent is large. A further investigation of this type of nonlinearity in the BLUES method is of great importance.

In solid-state physics, one often needs to consider equations such as the nonlinear Schrödinger (or Gross-Pitaevskii) and the Ginzburg-Landau equations, which possess complex solutions. These solutions are especially useful in research on Bose-Einstein condensates and nonlinear optics [103, 104, 105, 106]. While the use of complex functions does not entail conceptual or computational problems within the BLUES method, it would still present an interesting research problem.

For the Fisher equation, a possible avenue of research would be to check the relation between the *source* velocity and the *natural* velocity of the solution profile. This needs to be investigated in the context of PDEs. Furthermore, it would be interesting to study the BLUES method in the framework of so-called *pushed* or *pulled* fronts, e.g., in the dynamics of the density in an autocatalytic reaction-diffusion equation. The main difference between these two types of fronts is that pushed fronts converge to their asymptotic speed exponentially fast, while pulled fronts converge much more slowly [107]. The BLUES method may be ideally suited to find the analytical form of the asymptotic speed.

Finally, it would be interesting to explore whether the BLUES method is able to approximate physically relevant profiles of tidal bores in a minimal model [108, 109].

One important aspect of the method that has to be investigated is the mathematical theory of convergence. The sequential structure of the method makes it amenable to fixed-point analysis. A possible avenue for future research would be the construction of a proof for the convergence of the method, based on a Lipschitz argument, by showing that the operator for the sequence is a contraction. The general procedure is as follows. First and foremost, one needs to find a suitable complete metric space, say, the Banach space X and define a norm or metric $\|.\|$ in this space. Second, one needs to check whether the residual operator $\mathcal{R}$ satisfies a Lipschitz property, i.e., for $u, v \in X$,

$$\|\mathcal{R}\, u - \mathcal{R}\, v\| \leq L\|u - v\|\,, \tag{8.1}$$

where L is a positive constant. One then needs to prove that the BLUES method operator

$$(\mathcal{T} u)\,(x,t) \equiv u^{(0)}(x,t) + (B * \mathcal{R}\, u)(x,t) \tag{8.2}$$

is a contraction. From this property, one can then prove that the sequence of BLUES approximants is a Cauchy sequence. Now, because X is a complete metric space, the sequence converges to a fixed point u^*, which is the solution of the nonlinear differential equation at hand.

While this "proof" might seem simple enough, finding a complete metric space and norm is not trivial, and the Lipschitz property for the residual operator needs to be checked for every individual case. From the previous discussion one can find the "region" in parameter space where the BLUES function method converges and assess whether or not the method is useful for the problem at hand.

8.2 Deposition models

The synchronous hierarchical deposition model was studied in two distinct parts where the rules governing the deposition are different. In the first part, the hierarchical *random* deposition model (HRDM) was studied where particles are deposited simultaneously and a hyperbolic scaling law governs the particle size in each generation. The number of coastal points (or coastlines) was calculated, which are points (or lines) on the interface between a "sea level" and an elevated region. Next, the percolation probability for a spanning cluster to form laterally was calculated and a connection between the percolation threshold probability and the probability where the coastal points exhibit logarithmic fractal behaviour was found. This indicates that exactly at the onset of percolation, the number of coastal points grows linearly. Furthermore, the surface roughness exponent α was determined to be $1/2$ for a scaling factor $\lambda \geq 2$. All of the theoretical predictions are supported by numerical simulations.

In the final part we extended the rules of the HRDM to include lateral adhesion to previously deposited material through a "stickiness" parameter Γ, inducing lateral correlations between neighbouring columns. This model was aptly named the hierarchical *ballistic* deposition model (HBDM). Approximate calculations were performed for the surface length increment and the void ratio or porosity, which were supported by extensive numerical simulations.

8.2.1 Perspectives and future research

Further research could include extending the coastal-point calculations to the modified random deposition models of subsections 7.2.4 and 7.2.5 or for the hierarchical ballistic deposition of section 7.3 or a magnetic version of the model that has previously been studied in [110]. For these applications, it could be worthwhile to investigate the properties of the hierarchical random deposition model in different geometries, e.g., triangular, spherical, hexagonal etc., and with different boundary conditions.

In a more applied arena, optical and electromagnetic properties of the surface can be studied and tested in real-world applications such as the design of antennae [111] or acoustic metamaterials [112]. Possible physical quantities that are of practical use include e.g., thermal and electrical conductivity or optimal sound scattering angles. In the case where $\lambda = 2$, it can be checked whether the relation between the porosity and electrical conductivity obeys Archie's law [113, 101]. When a voltage is applied to a substrate grown by either the HRDM or the HBDM, one can calculate the distribution of the electrical potential in the material [114, 115], from which the effective conductivity σ can

be calculated. Initial numerical simulations show the potential distribution for a direct current for one possible realisation of the HBDM, see Fig. 8.1.

Figure 8.1: Potential distribution in a film grown by the HBDM with $P = 0.5$, $Q = 0$, $\Gamma = 0.75$, $\lambda = 3$ and $n = 4$. Red indicates regions where the potential is high while purple indicates regions where the potential is zero.

For a two-dimensional structure, a possible avenue for future research could be to calculate fractal properties of contour loops that form in the flooded landscape of e.g. Fig. 7.8. It is known [116] that there exist scaling relations between the roughness exponent α of a self-affine surface, the fractal dimension D_f, the loop correlation exponent x_l and the length distribution exponent τ. It would be interesting to calculate these exponents for both the HRDM and HBDM. One can also wonder whether the "cityscape" or "skyline" created by hierarchical deposition can be used to calculate e.g. the optimal building strategy to maximise solar energy yield in urban environments [117].

Of course one could try to extend all of the previously mentioned calculations for physical quantities to the HBDM. We expect this is not always feasible by virtue of the lateral correlations induced by the sticking of new particles. Another course of action would be including a different scaling law for the particle size that e.g. allows for larger particles to be deposited on top of smaller particles or by allowing new particles to "smash" into the material, partly erasing the history of the affected columns.

Aside from possible nanotechnological applications [5] or the calculation of different physical quantities, the rules of hierarchical deposition model can be further extended to include e.g. lateral diffusion, relaxation of incoming particles to "stick" to lower adjacent sides [99] or desorption of particles that are at the corners of the material [118].

Appendix A

BLUES function method

We provide additional calculations for the chapters on the BLUES function method for ODEs and PDEs. This appendix is mainly based on the appendices from the articles *"BLUES iteration applied to nonlinear ordinary differential equations for wave propagation and heat transfer"* [33] and *"The BLUES function method applied to partial differential equations and analytic approximants for interface growth under shear"* [45].

A.1 First approximants for the Burgers equation

To calculate the first approximant for the solution of the Burgers equation (3.22), the residual operator (3.23) is applied to the zeroth approximant (3.25) in accordance with the iteration equation (6.53)

$$\mathcal{R}_z U_\psi^{(0)}(z) = \begin{cases} \frac{k}{4\alpha^2}\left(2\alpha - K\mathrm{e}^{z/K}\right)\mathrm{e}^{z/K} & z < 0 \\ \frac{1}{4\alpha^2\beta^2}\left(4k^4\mathrm{e}^{\frac{2z}{K}} - k\alpha^2\left(2k\mathrm{e}^{\frac{\alpha z}{kK}} - K\mathrm{e}^{\frac{2z}{k}}\right)\right)\mathrm{e}^{-\frac{2z\alpha}{kK}} & z \geq 0, \end{cases} \tag{A.1}$$

where $\alpha = k + K$ and $\beta = k - K$. When $K = k$, the residual operator applied to equation (3.26) results in the following simple expression for the residual function

$$\mathcal{R}_z U_\psi^{(0)}(z) = \frac{1}{16k^2}\begin{cases} -k^2(\mathrm{e}^{2z/k} - 4\mathrm{e}^{z/k}) & z < 0 \\ (k+2z)(3k+2z)\mathrm{e}^{-2z/k} & z \geq 0. \end{cases} \tag{A.2}$$

Note that the residual function decays to zero when $|z| \to \infty$. Now a convolution product of the BLUES function (3.20) with the residual (A.1) is calculated. For

the sake of brevity, the difference between the zeroth and first approximants $\Delta U_\psi^{(1,0)} = U_\psi^{(1)} - U_\psi^{(0)}$ is shown, which is exactly the convolution product $\Delta U_\psi^{(1,0)}(z) = (B * \mathcal{R}_z U_\psi^{(0)})(z)$

$$\begin{aligned}\Delta U_\psi^{(1,0)}(z) = &\left(\frac{kK^2}{8\alpha^2(2k+K)}\left(K\left(\mathrm{e}^{z/K}-4\right)-8k\right)\mathrm{e}^{z/K}+\frac{k}{2}\right)(1-\Theta(z))\\ &-\left(\frac{k^5\mathrm{e}^{-\frac{2z}{k}}}{2\alpha^2\beta^2}+\frac{k^2\left(8k^3+16k^2K+6kK^2+K^3\right)\mathrm{e}^{-\frac{z}{k}}}{2\gamma\alpha^2}\right)\Theta(z)\\ &+\left(\frac{kK^3\mathrm{e}^{-\frac{2z}{K}}}{8\beta^2(K-2k)}+\frac{k^2K^2\mathrm{e}^{\frac{-\alpha z}{kK}}}{2\beta^2\alpha}\right)\Theta(z)\,,\end{aligned} \tag{A.3}$$

where $\gamma = K^2 - 4k^2$ and $\Theta(z)$ is the Heaviside step function. The case for which $K = 2k$ can be treated separately and results in the following simple expression

$$\Delta U_\psi^{(1,0)}(z) = \frac{1}{36}\begin{cases} k(18-8\mathrm{e}^{z/2k}+\mathrm{e}^{z/k}) & z<0\\ (-2k+24k\mathrm{e}^{z/2k}+\mathrm{e}^{z/k}(18z-11k))\mathrm{e}^{-2z/k} & z\geq 0\end{cases} \tag{A.4}$$

Note that the constant value at $z \to -\infty$ for the first approximants $U_\psi^{(1)}(z)$ in both cases (A.3) and (A.4) is now $1+k/2$, which for $k = 1/3$ equals $7/6 \approx 1.167..$ whereas the value for the exact solution is 1.268... This first iteration is already a good approximation to the exact result.

A.2 First approximant for the Fisher equation

To calculate the first approximant to the solution of the Fisher equation (3.39), the residual operator (3.40) is applied to the zeroth approximant (3.25) in accordance with the iteration equation (6.53)

$$\mathcal{R}_z U_\psi^{(0)}(z) = \frac{k}{4}\begin{cases}\frac{Ke^{z/K}\left(2\alpha-Ke^{z/K}\right)}{\alpha^2} & z<0\\ \frac{e^{-2z\left(\frac{1}{k}+\frac{1}{K}\right)}\left(K\alpha e^{z/k}-2k^2e^{z/K}\right)\left(2k^2e^{z/K}-\alpha e^{z/k}\left(K+2\beta e^{z/K}\right)\right)}{(k^2-K^2)^2} & z\geq 0\end{cases}, \tag{A.5}$$

where $\alpha = k + K$ and $\beta = k - K$. Now a convolution product of the BLUES function (3.20) with the residual (A.5) is calculated. The difference between

the zeroth and first approximants $\Delta U_\psi^{(1,0)} = U_\psi^{(1)} - U_\psi^{(0)}$ is shown, i.e.,

$$\begin{aligned}\Delta U_\psi^{(1,0)}(z) = {}& \frac{k}{8\alpha^2}\left(\frac{K^4}{2\alpha}\mathrm{e}^{-2z/K} - 4K^3\mathrm{e}^{-z/K}\right)(1-\Theta(z)) \\ & + \frac{k}{4\alpha^2}\left((2k^3+4k^2K+6kK^2+3K^3)\right)(1-\Theta(z)) \\ & + \frac{k}{8\alpha^2\beta^2}\left(4k^5\mathrm{e}^{-2z/k} + \frac{8k^2K^3(5k^2+K^2)}{\gamma}\mathrm{e}^{-z/k} + 4K^3\alpha^2\mathrm{e}^{-z/K}\right)\Theta(z) \\ & - \left(8k^2K^3\mathrm{e}^{-\alpha z/kK} + \frac{K^4\alpha^2}{2k-K}\mathrm{e}^{-2z/K}\right)\Theta(z)\,,\end{aligned} \tag{A.6}$$

where $\alpha = k+K$, $\beta = k-K$ and $\gamma = K^2-4k^2$. The cases for which $K = k$ and $K = 2k$ must be treated separately but these calculations will not be performed here. Note that in the first iteration the solution $U_\psi^{(1)}(z)$ approaches a constant value U_c for $z \to -\infty$. This constant was calculated in equation (3.43).

A.3 First approximant for the interface model with shear

The nonlinearity in equation (5.76) can be split up into two parts with different values for m, n. We first calculate the first correction to the zeroth iteration solution (5.62) for the nonlinearity $\mathcal{R}_x\, u = -\alpha u u_x$, which corresponds to $m = n = 1$. Starting from equation (5.65) and using the property (5.67) or (5.69), the function $\Xi(x,t,s)$ reduces to

$$\Xi(x,t,s) = \frac{\sqrt{\pi}\sqrt{2D(t-s)}}{2}\frac{\Sigma^3(s)}{S^3(t,s)}x\,. \tag{A.7}$$

Inserting this into (5.71) and keeping track of the signs results in the correction $\Delta u^{(1,0)} = u^{(1)} - u^{(0)}$, i.e.,

$$\begin{aligned}\Delta u^{(1,0)} &= \frac{\alpha}{(2\pi)^{\frac{3}{2}}}\int_0^t \mathrm{d}s \frac{\mathrm{e}^{-x^2/2S^2(t,s)}}{\sqrt{2D(t-s)}\Sigma(s)^4}\Xi(x,t,s) \\ &= \frac{\alpha x}{4\sqrt{2}\pi}\int_0^t \mathrm{d}s \frac{\mathrm{e}^{-x^2/2S^2(t,s)}}{\Sigma(s)S^3(t,s)}\,.\end{aligned} \tag{A.8}$$

By making the substitutions $\xi = S^{-1}(t,s)$, $2D(t-s) = 2\xi^{-2} - \Sigma^2(t)$ and $\Sigma(s) = \sqrt{2}\xi^{-1}\sqrt{\xi^2\Sigma^2(t)-1}$, the integral can be transformed into

$$\Delta u^{(1,0)} = \frac{\alpha x}{4\pi D}\int_{\xi_L}^{\xi_H} \mathrm{d}\xi \frac{\xi \mathrm{e}^{-x^2\xi^2/2}}{\sqrt{\Sigma^2(t)\xi^2-1}}, \tag{A.9}$$

with integration limits $\xi_L = S^{-1}(t,0) = \sqrt{2}/\Sigma(2t)$ and $\xi_H = S^{-1}(t,t) = \sqrt{2}/\Sigma(t)$. Before solving, we first proceed to calculate the first correction to the zeroth approximant (5.62) for the nonlinearity $\mathcal{R}_x\, u = -\beta u_x^2$, which corresponds to $m=0$, $n=2$. Starting from equation (5.65) and using the property (5.68) or (5.70), the function $\Xi(x,t,s)$ reduces to

$$\Xi(x,t,s) = \sqrt{2D(t-s)}\,\frac{\sqrt{\pi}}{2}\frac{\Sigma^3(s)}{S^3(t,s)}\left(2D(t-s) + \frac{x^2}{2}\frac{\Sigma^2(s)}{S^2(t,s)}\right). \tag{A.10}$$

Once again inserting this into (5.71) and keeping track of the signs results in the correction

$$\Delta u^{(1,0)} = -\frac{\beta}{4\pi\sqrt{2}}\int_0^t \mathrm{d}s \frac{\mathrm{e}^{-x^2/2S^2(t,s)}}{\Sigma^3(s)S^3(t,s)}\left(2D(t-s) + \frac{\Sigma^2(s)x^2}{2S^2(t,s)}\right). \tag{A.11}$$

By making the same substitutions as before the integral can be transformed into

$$\Delta u^{(1,0)} = \frac{-\beta}{8\pi D}\int_{\xi_L}^{\xi_H} \mathrm{d}\xi \frac{\xi \mathrm{e}^{-x^2\xi^2/2}}{\sqrt{\Sigma^2(t)\xi^2-1}}\left(x^2\xi^2 - 1 + \frac{1}{\Sigma^2(t)\xi^2-1}\right). \tag{A.12}$$

Finally, combining equations (A.9) and (A.12), the correction to the zeroth approximant becomes

$$\Delta u^{(1,0)} = \frac{1}{4\pi D}\int_{\xi_L}^{\xi_H} \mathrm{d}\xi \frac{\xi \mathrm{e}^{-x^2\xi^2/2}}{\sqrt{\Sigma^2(t)\xi^2-1}}\left(\frac{\beta}{2} + \alpha x - \frac{\beta x^2\xi^2}{2} - \frac{\beta}{2\left(\Sigma^2(t)\xi^2-1\right)}\right), \tag{A.13}$$

which can easily be solved and subsequently simplified by noticing that $2\Sigma^2(t) - \Sigma^2(2t) = \sigma^2$ to give the following expression for the correction in first iteration to the zeroth approximant of (5.76)

$$\begin{aligned}\Delta u^{(1,0)} = {} & \frac{\beta}{4\pi D}\left[\frac{\mathrm{e}^{-x^2/\Sigma^2(t)}}{\Sigma^2(t)} - \frac{\mathrm{e}^{-x^2/\Sigma^2(2t)}}{\Sigma(2t)\sigma}\right] \\ & + \frac{\alpha}{4D\sqrt{2\pi}}\left[\frac{\mathrm{e}^{-x^2/2\Sigma^2(t)}}{\Sigma(t)}\left(\operatorname{erf}\left(\frac{x}{\sqrt{2}\Sigma(t)}\right) - \operatorname{erf}\left(\frac{\sigma x}{\sqrt{2}\Sigma(t)\Sigma(2t)}\right)\right)\right].\end{aligned} \tag{A.14}$$

This can now be rearranged to yield equation (5.78).

A.4 Fourier coefficients for the space-periodic interface height profile

In this Appendix we discuss in detail the Fourier coefficients of various harmonics that are generated by the BLUES iteration at the level of the second approximant ($n = 2$) for the problem of the time evolution of the periodic interface height profile and compare them with their counterparts in 2nd-order PT. We first present, for $p \in \{0, 1, 2, 3\}$, the real pth coefficients calculated by both methods and then discuss them with the aid of two figures, A.1 and A.2.

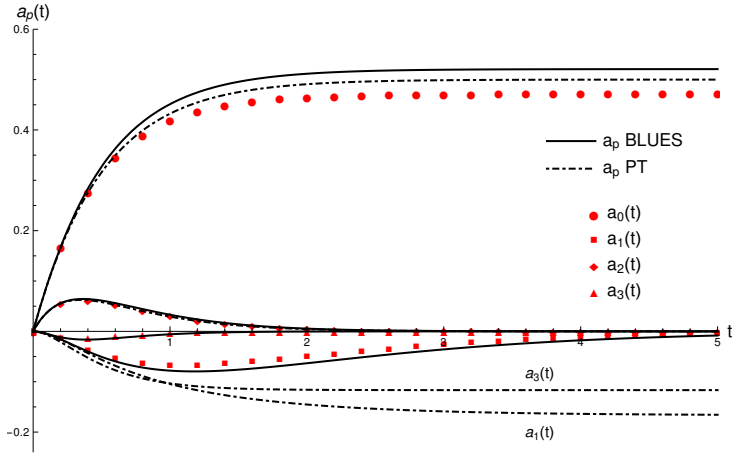

Figure A.1: Time evolution of the coefficients $a_p(t)$ of the cosine harmonics in the Fourier series expansion of the solution of (5.76). The numerical solutions (red symbols) for $a_p(t)$ are compared with the second approximants of the BLUES function method (full lines) and 2nd-order PT. Parameter values are $D = \alpha = 1$ and $\beta = -1$.

For the a_n coefficients we obtain:

- a_0 BLUES:

$$a_0(t) = -\frac{\beta(1 - e^{-2Dt})}{2D} - \frac{\beta\left(\alpha^2 + \beta^2\right)\left(1 - e^{-2Dt}\right)^3\left(3 + e^{-2Dt}\right)}{96D^3} \quad \text{(A.15)}$$

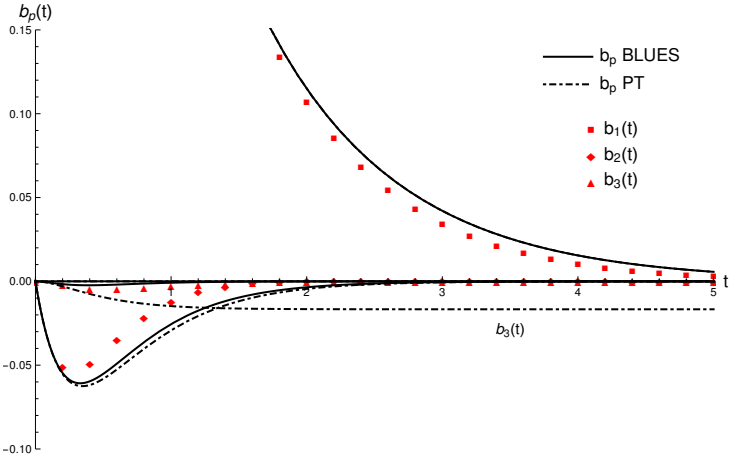

Figure A.2: Time evolution of the coefficients $b_p(t)$ of the sine harmonics in the Fourier series expansion of the solution of (5.76). The numerical solutions (red symbols) for $b_p(t)$ are compared with the second approximants of the BLUES function method (full lines) and 2nd-order PT. Parameter values are $D = \alpha = 1$ and $\beta = -1$.

- a_0 PT:

$$a_0(t) = -\frac{\beta(1 - e^{-2Dt})}{2D} \tag{A.16}$$

- a_1 BLUES:

$$a_1(t) = -\frac{\alpha\beta\left(e^{-Dt} + 2e^{-3Dt} - 3e^{-5Dt}\right)}{32D^2} + \frac{\alpha\beta e^{-Dt}\, t}{4D} \tag{A.17}$$

- a_1 PT:

$$a_1(t) = \frac{\alpha\beta(16 - 15e^{-Dt} - 10e^{-3Dt} + 9e^{-5Dt})}{96D^2} \tag{A.18}$$

- a_2 BLUES

$$a_2(t) = -\frac{\beta(e^{-2Dt} - e^{-4Dt})}{4D} - \frac{\alpha^2\beta(e^{-2Dt} - e^{-6Dt})}{16D^3} + \frac{\alpha^2\beta e^{-4Dt}t}{4D^2} \tag{A.19}$$

- a_2 PT:

$$a_2(t) = -\frac{\beta(e^{-2Dt} - e^{-4Dt})}{4D} \tag{A.20}$$

- a_3 BLUES:

$$a_3(t) = \frac{7\alpha\beta(1-e^{-2Dt})^2(2e^{-3Dt}+e^{-5Dt})}{96D^2} \tag{A.21}$$

- a_3 PT:

$$a_3(t) = \frac{7\alpha\beta(2-5e^{-3Dt}+3e^{-5Dt})}{120D^2} \tag{A.22}$$

- a_4 BLUES:

$$a_4(t) = \frac{\beta(\beta^2-2\alpha^2)(1-e^{-2Dt})^3(10e^{-4Dt}+6e^{-6Dt}+3e^{-8Dt}+e^{-10Dt})}{960D^3} \tag{A.23}$$

For the b_n coefficients we obtain:

- $b_0 = 0$ BLUES and PT.
- b_1 BLUES:

$$b_1(t) = e^{-Dt} - \frac{(\alpha^2+4\beta^2)(e^{-Dt}-2e^{-3Dt}+e^{-5Dt})}{32D^2} \tag{A.24}$$

- b_1 PT:

$$b_1(t) = e^{-Dt} - \frac{(\alpha^2+4\beta^2)(e^{-Dt}-2e^{-3Dt}+e^{-5Dt})}{32D^2} \tag{A.25}$$

- b_2 BLUES:

$$b_2(t) = -\frac{\alpha(e^{-2Dt}-e^{-4Dt})}{4D} + \frac{\alpha\beta^2(e^{-2Dt}-e^{-6Dt})}{16D^3} - \frac{\alpha\beta^2 e^{-4Dt}\,t}{4D^2} \tag{A.26}$$

- b_2 PT:

$$b_2(t) = -\frac{\alpha(e^{-2Dt}-e^{-4Dt})}{4D} \tag{A.27}$$

- b_3 BLUES:

$$b_3(t) = \frac{(3\alpha^2-4\beta^2)(1-e^{-2Dt})^2(2e^{-3Dt}+e^{-5Dt})}{96D^2} \tag{A.28}$$

- b_3 PT:

$$b_3(t) = \frac{(3\alpha^2-4\beta^2)(2-5e^{-3Dt}+3e^{-5Dt})}{120D^2} \tag{A.29}$$

- b_4 BLUES:

$$b_4(t) = -\frac{\alpha(\alpha^2 - 5\beta^2)(1 - e^{-2Dt})^3(10e^{-4Dt} + 6e^{-6Dt} + 3e^{-8Dt} + e^{-10Dt})}{1920D^3} \tag{A.30}$$

Note that in the second approximant for $a_0(t)$ terms of order $\alpha^2\beta$ and β^3 are generated, which are absent in 2nd-order PT. Als note that $a_1(t)$ (first harmonic) and $a_3(t)$ (third harmonic) are both proportional to $\alpha\beta$, as in PT. Importantly, in the BLUES function method $a_1(t)$ and $a_3(t)$ tend to zero for long times, in agreement with the numerical solution, whereas the 2nd-order PT expressions tend to non-zero constants (see also Fig. A.1). In this respect the BLUES iteration is qualitatively superior. The coefficient $a_2(t)$ (second harmonic) has a first order in β contribution which is the same in both methods, and an additional $\alpha^2\beta$ contribution in the second BLUES approximant. In both methods the result is very close to the numerical solution (see Fig. A.1). Note that $a_4(t)$ (fourth harmonic) is generated in 2nd-iteration BLUES but is absent in 2nd-order PT. This is a consequence of the fact that the BLUES function method is non-perturbative and already generates higher harmonics in a lower iteration than the perturbation series.

As for the $b_n(t)$, the coefficient $b_1(t)$ (first harmonic reflecting the initial condition) contains the zeroth approximant, which is (of course) the same in both methods. Moreover, the entire expressions for $b_1(t)$ coincide in 2nd-iteration BLUES and 2nd-order PT (see also Fig. A.2). The coefficient $b_2(t)$ (second harmonic) has a first order in α contribution which is the same in both methods, and an additional $\alpha\beta^2$ contribution in the 2nd BLUES approximant. In both methods the result is nearly the same but both are somewhat off of the numerical solution (see Fig. A.2). Importantly, in the BLUES function method $b_3(t)$ (third harmonic) tends to zero for long times, in agreement with the numerical solution, whereas the 2nd-order PT expression tends to a non-zero constants (see also Fig. A.2). In this respect the BLUES iteration is again qualitatively superior. Finally, $b_4(t)$ (fourth harmonic) is present in BLUES but is obviously absent in 2nd-order PT because it is of third order.

Appendix B

Epidemiological models

We provide additional calculations for the chapter on the BLUES function method for CDEs and a complete global stability analysis for the SIRS model. This appendix is based on the appendix from the preprint *"Epidemic processes with constant vaccination and immunity loss studied with the BLUES function method"* [61]. It is supplemented with calculations on the SEIRS model.

B.1 Stability analysis for the SIRS model

The system (6.15) has two fixed points that can be found by a fixed-point analysis which reveals both the disease-free equilibrium ε_0 in which the disease has died out, and an endemic equilibrium ε_e in which the infected population density reaches a nonzero asymptotic value, i.e.,

$$\varepsilon_0 = (s_0^*, i_0^*) = \left(1 - \frac{\pi p}{\pi + \xi}, 0\right) \tag{B.1a}$$

$$\varepsilon_e = (s_e^*, i_e^*) = \left(\frac{\pi + \gamma}{\beta}, \frac{\beta((1-p)\pi + \xi) - (\gamma + \pi)(\xi + \pi)}{\beta(\gamma + \pi + \xi)}\right). \tag{B.1b}$$

Note that the disease-free equilibrium ε_0 is independent of the average contact rate β. The endemic equilibrium (B.1b) can be simplified to

$$\varepsilon_e = (s_e^*, i_e^*) = \left(\left(1 - \frac{\pi p}{\pi + \xi}\right)\frac{1}{R_V}, \frac{(1-p)\pi + \xi}{\gamma + \pi + \xi}\left(1 - \frac{1}{R_V}\right)\right). \tag{B.2}$$

The global asymptotic stability for the endemic equilibrium can be proven as follows. First note that the positive quadrant $\mathbb{R}^2_+$ of the SI-plane is not an invariant set of the system (6.15), i.e., when $s(t) = 0$ then $s'(t) < 0$ for all values $i(t) > (\pi(1-p)+\xi)/\xi$. This can be resolved by shifting (s, i) to (Σ, i), where

$$\Sigma(t) = s(t) + \frac{\xi}{\beta}\,. \tag{B.3}$$

Hence, the shifted system becomes

$$\Sigma'(t) = \pi(1-p) - \beta\Sigma(t)i(t) - (\pi+\xi)\Sigma(t) + \frac{\xi}{\beta}(\xi+\pi) + \xi \tag{B.4a}$$

$$i'(t) = \beta\Sigma(t)i(t) - (\gamma+\pi+\xi)i(t)\,. \tag{B.4b}$$

It is now easy to see for $\Sigma(t) = 0$, now $\Sigma'(t) \geq 0$ for all values of $i(t)$. By shifting the system, the endemic equilibrium coordinates change as follows

$$(\Sigma_e^*, i_e^*) = \left(\frac{\pi+\gamma+\xi}{\beta}, \frac{\pi((1-p)\beta-\gamma-\pi)+\xi(\beta-\gamma-\pi)}{\beta(\pi+\gamma+\xi)}\right). \tag{B.5}$$

All global properties of the system remain invariant under the shifting of the coordinates, so we can now try to find a Lyapunov function $V(\Sigma, i)$ to prove global asymptotic stability of the endemic fixed point (B.5) of the shifted system (B.4) and hence also of the original system (6.15). We can choose the following Lyapunov function [119]

$$V(\Sigma, i) = \Sigma_e^*\left(\frac{\Sigma}{\Sigma_e^*} - \ln\frac{\Sigma}{\Sigma_e^*}\right) + i_e^*\left(\frac{i}{i_e^*} - \ln\frac{i}{i_e^*}\right) \tag{B.6}$$

with time derivative

$$\begin{aligned} V'(\Sigma, i) &= \frac{\partial V}{\partial \Sigma}\Sigma'(t) + \frac{\partial V}{\partial i}i'(t) \\ &= \left(1 - \frac{\Sigma_e^*}{\Sigma(t)}\right)\Sigma'(t) + \left(1 - \frac{i_e^*}{i(t)}\right)i'(t)\,. \end{aligned} \tag{B.7}$$

Now, from (B.4a) and (B.4b) it is clear that for the endemic equilibrium the following holds

$$\begin{aligned} \beta\Sigma_e^* i_e^* &= \pi(1-p) - (\pi+\xi)\Sigma_e^* + \frac{\xi}{\beta}(\xi+\pi) + \xi \\ &= (\gamma+\pi+\xi)i_e^*\,. \end{aligned} \tag{B.8}$$

Substituting this property into (B.7) and simplifying gives after some algebra

$$\begin{aligned} V'(\Sigma, i) &= \left(1 - \frac{\Sigma_e^*}{\Sigma(t)}\right) \Sigma'(t) + \left(1 - \frac{i_e^*}{i(t)}\right) i'(t) \\ &= -\left(\pi(1-p) + \frac{\xi}{\beta}(\xi + \pi) + \xi\right) \left(\frac{\Sigma(t)}{\Sigma_e^*}\right) \left(1 - \frac{\Sigma_e^*}{\Sigma(t)}\right)^2 \qquad \text{(B.9)} \\ &\leq 0\,, \end{aligned}$$

for all values of $\Sigma, i \geq 0$. This concludes the proof that the endemic equilibrium is globally asymptotically stable. Proving the global stability of the disease-free fixed point is now trivial. One can repeat the previous calculations with the Lyapunov function

$$V(\Sigma, i) = \Sigma_0^* \left(\frac{\Sigma}{\Sigma_0^*} - \ln \frac{\Sigma}{\Sigma_0^*}\right) + i\,, \qquad \text{(B.10)}$$

which is the same as (B.6) with now Σ_0^* instead of Σ_e^* and $i_e^* \to 0$.

B.2 First SIRS approximants

We list here the first analytical approximants $s^{(1)}(t)$ and $i^{(1)}(t)$ for the disease-free equilibrium in the SIRS model:

$$
\begin{aligned}
s^{(1)}(t) = 1 &- \frac{p\pi}{\pi+\xi} + \frac{\beta i_0^2 \xi(\gamma+\pi-\xi)}{(\gamma+\pi)(\gamma-\xi)(2\gamma+\pi-\xi)} e^{-2(\gamma+\pi)t} \\
&+ \left(\frac{\beta\gamma i_0^2 \xi}{(\gamma+\pi)(\gamma-\xi)(2\gamma+\pi-\xi)} + \frac{\pi p}{\pi+\xi} + s_0 - 1 \right) e^{-(\pi+\xi)t} \\
&+ \frac{i_0}{(\gamma-\xi)^2} \left(\xi^2 \left(\frac{\beta i_0}{\gamma+\pi} - \beta t - 1 \right) - \frac{\beta\pi^2 p(\gamma+\pi)}{(\pi+\xi)^2} \right) e^{-(\gamma+\pi)t} \\
&- \left(\frac{i_0(\xi(\gamma+\pi)(\gamma-\xi) + \beta\gamma(\pi+\xi+\pi(-p)) + \beta\gamma s_0(\gamma-\xi))}{(\gamma+\pi)(\gamma-\xi)^2} \right) e^{-(\pi+\xi)t} \\
&+ \frac{i_0}{(\gamma-\xi)^2} \left(\frac{\beta\pi(\gamma+\pi(\pi pt+2p+1-i_0)+\gamma\pi pt)}{\pi+\xi} + \frac{\beta\xi s_0(\gamma-\xi)}{\pi+\xi} \right) e^{-(\gamma+\pi)t} \\
&+ \frac{i_0}{(\gamma-\xi)^2} \left(\xi(\gamma+\beta(\pi pt+\gamma t+1-i_0)) - \beta\pi(pt(\gamma+\pi)+p+1-i_0) \right) e^{-(\gamma+\pi)t} \\
&+ \frac{\beta i_0 \pi\xi(\pi(1-p-i_0-s_0)+(1-i_0-s_0))}{(\gamma+\pi)(\gamma-\xi)(\pi+\xi)^2} e^{-(\gamma+2\pi+\xi)t} \\
&+ \frac{\beta i_0 \pi\gamma(\pi(p+s_0-1)+\xi(s_0-1))}{(\gamma+\pi)(\gamma-\xi)(\pi+\xi)^2} e^{-(\gamma+2\pi+\xi)t} \qquad \text{(B.11)}
\end{aligned}
$$

$$
\begin{aligned}
i^{(1)}(t) = &\frac{i_0\beta(\pi(1-p-s_0)+\xi(1-s_0))}{(\pi+\xi)^2} e^{-(2\pi+\gamma+\xi)t} \\
&+ i_0 \left(1 + \beta(t + \frac{\pi p}{(\pi+\xi)^2} - \frac{1+\pi pt-s_0}{\pi+\xi}) \right) e^{-(\pi+\gamma)t} \\
&+ i_0^2\beta\xi \left[\frac{e^{-(2\pi+\gamma+\xi)t}}{(\pi+\xi)(\gamma-\xi)} - \frac{e^{-2(\pi+\gamma)t}}{(\pi+\gamma)(\gamma-\xi)} - \frac{e^{-(\pi+\gamma)t}}{(\pi+\gamma)(\pi+\xi)} \right] . \qquad \text{(B.12)}
\end{aligned}
$$

B.3 The SEIRS model

The equilibria of the SEIRS model can be found by first substituting $r = 1 - s - e - i$ into the system (6.39) and solving the resulting reduced "three-dimensional" subsystem with $s' = e' = i' = 0$. The disease-free ε_0 and endemic ε_e equilibria are respectively

$$\varepsilon_0 = (s_0^*, e_0^*, i_0^*) = \left(1 - \frac{\pi p}{\pi + \xi}, 0, 0\right) \tag{B.13a}$$

$$\varepsilon_e = (s_e^*, e_e^*, i_e^*) \tag{B.13b}$$

with

$$s_e^* = \frac{(\pi + \gamma)(\pi + \sigma)}{\beta\sigma} \tag{B.14a}$$

$$e_e^* = \frac{\beta\sigma(\pi(1-p) + \xi) - (\pi + \sigma)(\pi + \gamma)(\pi + \xi)}{\beta\sigma(\gamma(\pi + \xi + \sigma) + (\pi + \xi)(\pi + \sigma))}(\pi + \gamma) \tag{B.14b}$$

$$i_e^* = \frac{\beta\sigma(\pi(1-p) + \xi) - (\pi + \sigma)(\pi + \gamma)(\pi + \xi)}{\beta(\gamma(\pi + \xi + \sigma) + (\pi + \xi)(\pi + \sigma))}\,. \tag{B.14c}$$

Note that when $\sigma \to \infty$, the equilibria reduce to those of the SIRS model, i.e., equations (B.1a) and (B.2), with $e_e^* = 0$. We now write the system as a vector equation as in (6.18), where the vector of initial conditions $\boldsymbol{C}$ can be included by multiplying it with a point source at $t = 0$. We have $\boldsymbol{X}$ the vector of solutions, $\boldsymbol{C}$ the vector of initial conditions, $\boldsymbol{\chi}$ the vector of external sources, i.e.,

$$\boldsymbol{X}(t) = \begin{pmatrix} s(t) \\ e(t) \\ i(t) \end{pmatrix} \qquad \boldsymbol{C} = \begin{pmatrix} s_0 \\ e_0 \\ i_0 \end{pmatrix} \qquad \boldsymbol{\chi} = \begin{pmatrix} \pi(1-p) + \xi + \beta s^* i^* \\ -\beta s^* i^* \\ 0 \end{pmatrix} \tag{B.15}$$

and A the matrix of coefficients for the linear part of the reduced subsystem,

$$A = \begin{pmatrix} -(\pi + \xi + \beta i^*) & -\xi & -(\xi + \beta s^*) \\ \beta i^* & -(\sigma + \pi) & \beta s^* \\ 0 & \sigma & -(\gamma + \pi) \end{pmatrix}. \tag{B.16}$$

Finally, the nonlinear part of the system (6.39) is given by

$$\mathcal{R}\boldsymbol{X} = \begin{pmatrix} -\beta(s - s^*)(i - i^*) \\ \beta(s - s^*)(i - i^*) \\ 0 \end{pmatrix}. \tag{B.17}$$

The BLUES iteration can now be set up in the same manner as (6.26) and (5.62).

Appendix C

Hierarchical deposition

This appendix is based on the appendix in the article *"Coastlines and percolation in a model for hierarchical random deposition"* that appeared in *Physica A: Statistical Mechanics and its Applications* [74]. It is supplemented with additional numerical simulations on the roughness exponent and the percolation probability for the HBDM.

C.1 Number of coastal points

Starting from equation (7.10) and working out the sums explicitly results in the following expression for the number of coastal points in generation n:

$$\mathcal{N}_n(P,Q) = 2\lambda P(1-P)\frac{1-(1-S)^{2n}}{1-(1-S)} \tag{C.1}$$

$$+ 2\lambda(\lambda-1)P(1-P)(1-S)\left[\frac{1-(\lambda(1-S))^{n-1}}{1-\lambda(1-S)}\right]$$

$$+ 2\lambda P(Q-P)(1-S)\left[\frac{1-\lambda^{n-1}(1-S)^{n-1}}{1-\lambda(1-S)}\right]\left[\frac{1-\lambda^{-(n-1)}(1-S)^{n-1}}{1-\lambda^{-1}(1-S)}\right]$$

$$+ 2\lambda(\lambda-1)P(1-P)(1-S)^3\left[\frac{1-\lambda^{n-2}(1-S)^{n-2}}{1-\lambda(1-S)}\right]\left[\frac{1-\lambda^{-(n-2)}(1-S)^{n-2}}{1-\lambda^{-1}(1-S)}\right].$$

It can be seen now that if $\lambda(1-S)<1$, the above expression converges to a constant γ for very large values of n. This constant can be calculated to be

$$\begin{aligned}\gamma = &\frac{2\lambda P(1-P)}{1-(1-S)} + \frac{2\lambda(\lambda-1)P(1-P)(1-S)}{1-\lambda(1-S)} \\ &+ \frac{2\lambda P(Q-P)(1-S)}{1-(1-S)(\lambda+\lambda^{-1})+(1-S)^2} \\ &+ \frac{2\lambda(\lambda-1)P(1-P)(1-S)^3}{1-(1-S)(\lambda+\lambda^{-1})+(1-S)^2}\,.\end{aligned} \tag{C.2}$$

For $\lambda(1-S)>1$, the number of coastal points increases exponentially. The limiting case $\lambda(1-S)=1$ results in a linear increase in coastal points. This can be seen by formally calculating the limit of the number of coastal points (C.1) for $\lambda(1-S)\to 1$, which results in

$$\begin{aligned}\mathcal{N}_n(P,Q) = &\,2\lambda(\lambda-1)P(1-P)(1-S)(n-1) \\ &+ 2\lambda P(Q-P)(1-S)(n-1) \\ &+ 2\lambda(\lambda-1)P(1-P)(1-S)^3(n-2)\,.\end{aligned} \tag{C.3}$$

C.2 Percolation in third generation

In generation $n=3$ with $\lambda=3$ there are 721 different possibilities to obtain percolation. We will not list them all but will show some possibilities and comment on the degeneracy within one combination.

First, consider combinations that experienced the deposition of two hills of length $1/\lambda$ and one empty space in the first generation. There are only three ways to do this. In the second generation, consider hills of length $1/\lambda^2$ or empty spaces being deposited in the empty space created in the first generation. Once again, only zero, one or two hills can be deposited, with the possible number of configurations being respectively 1, 3 and 3. In the third generation, percolation can only occur when all remaining empty spaces at sea level are filled with conducting hills. These possibilities are shown in Fig. C.1. It is now straightforward to see that this results in 21 different possible configurations. Added together, these probabilities result in

$$3P^2(1-S)\sum_{k=0}^{2}\binom{2}{k}P^k(1-S)^{3-k}P^{3(3-k)}\,. \tag{C.4}$$

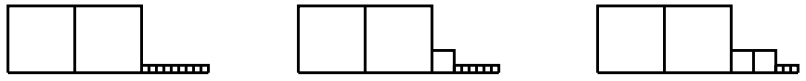

(a) (b) (c)

Figure C.1: Possible configurations in which percolation is achieved when two blocks were deposited in $n = 1$ and (a) no block was deposited, (b) one block was deposited or (c) two blocks were deposited in $n = 2$.

Next, we consider possibilities in which a single hill was deposited in the first generation. Once again there are only three possibilities. In the second generation, 0 to 5 hills can be deposited with the number of configurations being, respectively, 1, 6, 15, 20, 15 and 6. In the third generation, empty spaces at sea level need to be filled with conducting hills to obtain percolation. Some combinations are shown in Fig.C.2 for 1, 2 or 3 hills being deposited in the second generation.

(a) (b) (c)

Figure C.2: Possible configurations in which percolation is achieved when one block was deposited in $n = 1$ and (a) one block was deposited, (b) two blocks were deposited or (c) three blocks were deposited in $n = 2$. The possibilities where 0, 4 or 5 blocks were deposited are not shown.

This results in a total of 189 different microscopic configurations. Once again adding these probabilities together, the following expression is obtained

$$3P(1-S)^2 \sum_{k=0}^{5} \binom{5}{k} P^k (1-S)^{6-k} P^{18-3k} \,. \tag{C.5}$$

Lastly, consider the possibilities in which in the first generation nothing has been deposited. We will not show this here but after some calculations it is straightforward to see that this results in 511 unique combinations for percolation. In this case the probability becomes

$$(1-S)^3 \sum_{k=0}^{8} \binom{8}{k} P^k (1-S)^{9-k} P^{27-3k} \,. \tag{C.6}$$

In total, for $n = 3$, there are 721 different microscopic combinations possible to obtain percolation, with an associated probability

$$\begin{aligned} &3P^2(1-S)\sum_{k=0}^{2}\binom{2}{k}P^k(1-S)^{3-k}P^{9-3k} \\ &+3P(1-S)^2\sum_{k=0}^{5}\binom{5}{k}P^k(1-S)^{6-k}P^{18-3k} \\ &+(1-S)^3\sum_{k=0}^{8}\binom{8}{k}P^k(1-S)^{9-k}P^{27-3k}\,. \end{aligned} \tag{C.7}$$

Adding the different contributions results in an expression for the percolation probability for $\lambda = 3$ and $n = 3$.

C.3 The roughness exponent of the resulting surface revisited

We calculate the roughness exponent α_λ for the surface created by the HBDM and compare with the value of $\alpha = 1/2$ previously predicted in subsection 7.2.2 for the HRDM. We denote by the index λ the scale factor for which the roughness exponent was calculated. In Table C.1, the exponents α_3 and α_2 are shown for different values of Γ; first for $\lambda = 3$, $n = 6$ and subsequently for $\lambda = 2$, $n = 8$, with $P = 0.7$ and $Q = 0$. The results are averaged over 2000 realisations for each data point.

Table C.1: Roughness exponents α_3 and α_2 for the surface resulting from the HBDM for different values of Γ, with $P = 0.7$ and $Q = 0$.

Γ	0	1/3	2/3	1
α_3	0.4935	0.4792	0.4758	0.4636
α_2	0.4883	0.4463	0.4373	0.4562

From Figures C.3 and C.4 it can be seen that by increasing the value of the stickiness parameter Γ the distinct fine structure that is present in the case where $\Gamma = 0$ now vanishes, slowly being smoothed out by lateral correlation between the columns.

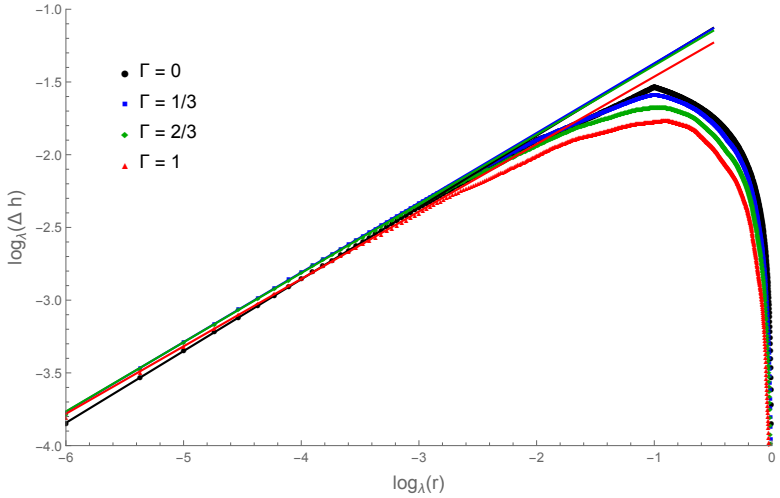

Figure C.3: Log-log plot of the height–height correlation function for $\lambda = 3$, $P = 0.7$, $Q = 0$ and $n = 6$ drawn for different values of Γ.

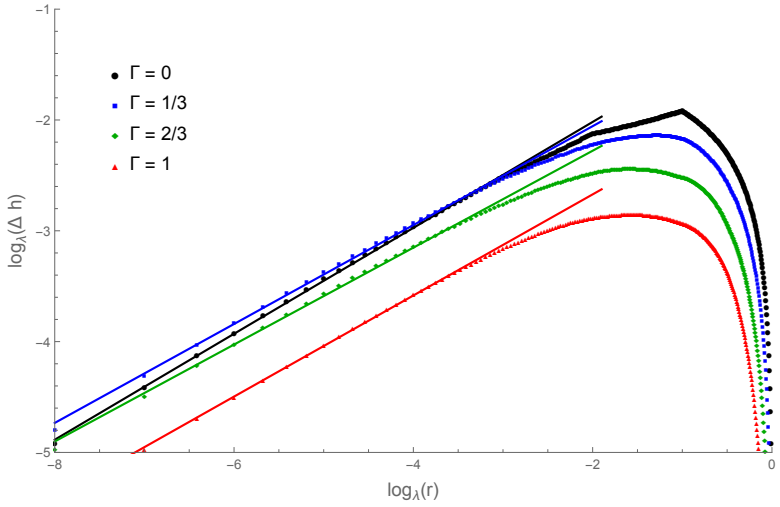

Figure C.4: Log-log plot of the height–height correlation function for $\lambda = 2$, $P = 0.7$, $Q = 0$ and $n = 8$ drawn for different values of Γ.

C.4 Percolation for the HBDM: numerical results

We provide numerical results for the percolation probability in the HBDM for $\lambda = 3$. The presence of overhangs can shield the underlying substrate and prevent future percolation from occurring in all subsequent generations. We expect that when $\Gamma > 0$, a percolating cluster can only form in the first generation due to the absence of overhangs. Hence, for $\lambda \geq 3$, the percolation threshold is located at the trivial value of $P_c = 1$. This can easily be seen in Fig. C.5, where the percolation probability is shown for different values of Γ, with $Q = 0$ and $n = 6$. For each data point, the results are averaged over 5000 realisations.

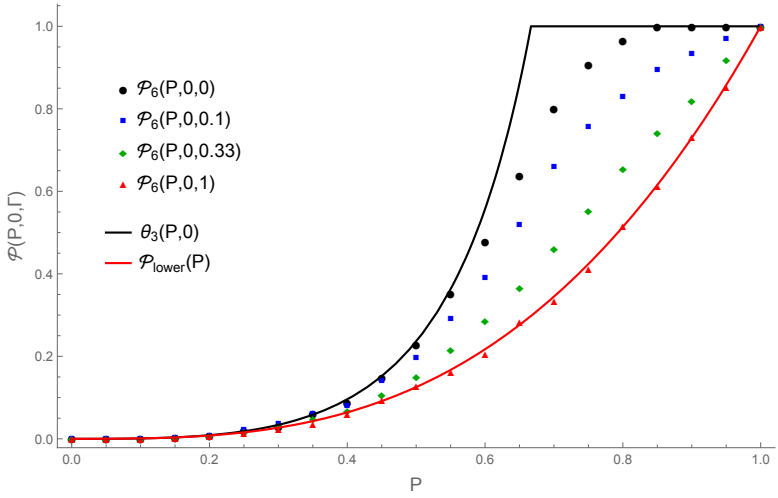

Figure C.5: Percolation probability $\mathcal{P}_6(P, Q, \Gamma)$ for $\lambda = 3$ and $Q = 0$ shown for different values of Γ. The fixed-point solution $\theta_3(P)$ for $\Gamma = 0$ is shown (black, full line) together with the lower bound $\mathcal{P}_{lower}(P)$ (red, full line) given by equation (C.9), and the numerical results for generation $n = 6$ (symbols).

While we do not attempt to derive an exact expression for the fixed-point solution here, we can however note that for $\lambda \geq 3$ the percolation probability

must be bounded from below by the function

$$\begin{aligned}\mathcal{P}_{lower}(P) &= P^{\lambda} + (1-P)^{\lambda}P^{\lambda^2} + (1-P)^{\lambda}(1-P)^{\lambda^2}P^{\lambda^3} + ... \\ &= P^{\lambda} + \sum_{i=1}^{\infty}\prod_{j=1}^{i}(1-P)^{\lambda^j}P^{\lambda^{i+1}} \\ &= P^{\lambda} + \sum_{i=1}^{\infty}(1-P)^{\frac{\lambda(\lambda^i-1)}{\lambda-1}}P^{\lambda^{i+1}}\end{aligned} \tag{C.8}$$

for the case where $\Gamma = 1$, and from above by $\theta_{\lambda}(P)$, i.e., the fixed-point solution of equation (7.27) for the HRDM with $\Gamma = 0$. The summation on the last line of (C.8) can be performed exactly and a closed form solution is found when the substitution $j = \lambda^{i+1}$ is introduced, i.e.,

$$\mathcal{P}_{lower}(P) = P^{\lambda} + \frac{(1-P)^{\lambda}P^{\lambda^2}}{1-P(1-P)^{\frac{1}{\lambda-1}}}\,. \tag{C.9}$$

Note that for $\lambda = 2$, overhanging particles can connect horizontally to bridge underlying gaps, achieving percolation by connecting disjoint parts of the material on an elevated level, i.e. above sea level. We defer a more thorough investigation of this phenomenon for future research.

C.5 Saturated void volume

Suppose that in the ith generation a single wall was created with height λ^{-i}. A void with volume (or area) $\lambda^{-(i+1)}$ is created by depositing a sticking and a non-sticking particle next to each other. A hierarchy of consecutive voids can be created at the vertical wall created by the previous deposition, as shown in Fig. C.6 for the first three consecutive generations. This can be continued *at infinitum*. The result is summed for generations i from 2 to infinity, i.e.,

$$2P(1-\Gamma)(1-P)\sum_{i=2}^{\infty}\sum_{j=1}^{\infty}\sum_{k=1}^{j}\lambda^{-2(i+k)}\left(P^2\Gamma(1-\Gamma)\right)^j\,, \tag{C.10}$$

for all generations $i \geq 2$. Obviously, closed-off voids can only be created for $\lambda = 2$ but we will continue to use λ in the following calculations to avoid confusion with notation.

We can now repeat the same procedure for the case where two consecutive walls of height λ^{-i} are present in generation i. We then consider the next generation

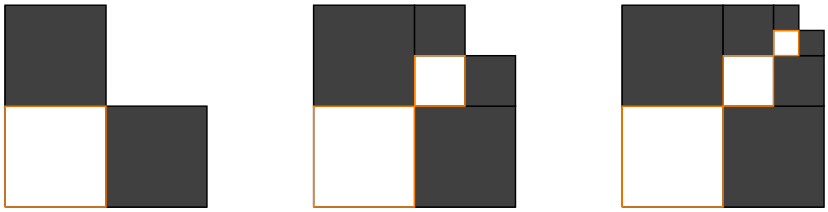

Figure C.6: First three consecutive configurations for generations $i+1$ (left), $i+2$ (middle) and $i+3$ (right) for voids to be created when one vertical wall (on the left edge) is present in generation i. The voids are indicated by an orange edge.

$i+1$. There are two possibilities at this stage, which are shown in Fig. C.7. The total void volume is

$$(2\,\lambda^{-2(i+1)})P^2\Gamma^2 + (\lambda^{-2(i+1)})2P^2\Gamma(1-\Gamma)\,. \tag{C.11}$$

Figure C.7: Possibilities for voids (indicated with an orange edge) to be created in generation $i+1$ for a wall–wall combination.

For generation $i+2$, the three possibilities are shown in Fig. C.8 and the total void volume is given by

$$\begin{aligned}
&\left(2\lambda^{-2(i+1)} + 2\lambda^{-2(i+2)}\right)\left(2P\Gamma(1-P)\right)P^2\Gamma^2 \\
&+ \left(\lambda^{-2(i+1)} + 2\lambda^{-2(i+2)}\right)\left(2P^2\Gamma(1-\Gamma)\right)P^2\Gamma^2 \\
&+ \left(\lambda^{-2(i+1)} + \lambda^{-2(i+2)}\right)\left(2P^2\Gamma(1-\Gamma)\right)^2\,.
\end{aligned} \tag{C.12}$$

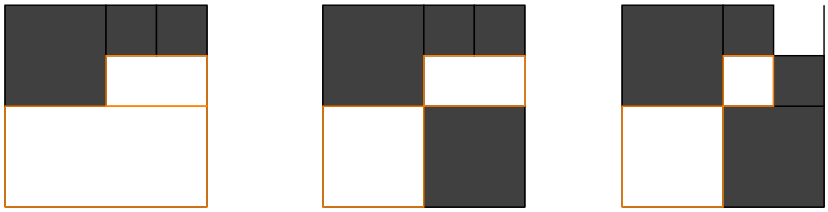

Figure C.8: Possibilities for voids (indicated with an orange edge) to be created in generation $i+2$ for a wall–wall combination.

For generation $i+3$, the four possibilities are shown in Fig. C.9 and the total void volume is now given by

$$\begin{aligned}
&\left(2\lambda^{-2(i+1)} + 2\lambda^{-2(i+2)} + 2\lambda^{-2(i+3)}\right) \left(2P\Gamma(1-P)\right)^2 P^2\Gamma^2 \\
&+ \left(\lambda^{-2(i+1)} + 2\lambda^{-2(i+2)} + 2\lambda^{-2(i+3)}\right) \left(2P^2\Gamma(1-\Gamma)\right) \left(2P\Gamma(1-P)\right) P^2\Gamma^2 \\
&+ \left(\lambda^{-2(i+1)} + \lambda^{-2(i+2)} + 2\lambda^{-2(i+3)}\right) \left(2P^2\Gamma(1-\Gamma)\right)^2 P^2\Gamma^2 \\
&+ \left(\lambda^{-2(i+1)} + \lambda^{-2(i+2)} + \lambda^{-2(i+3)}\right) \left(2P^2\Gamma(1-\Gamma)\right)^3 .
\end{aligned} \tag{C.13}$$

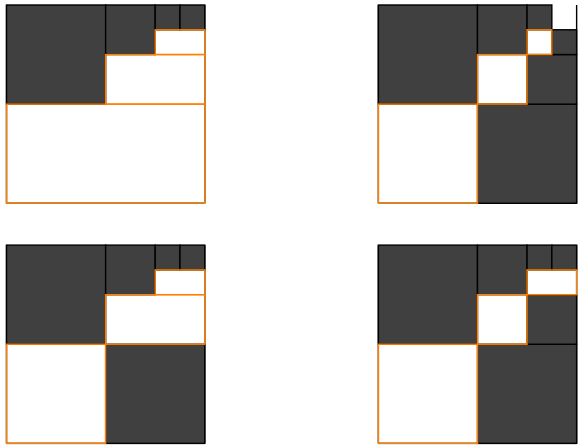

Figure C.9: Possibilities for voids (indicated with an orange edge) to be created in generation $i+3$ for a wall–wall combination.

Equations (C.11), (C.12) and (C.13) can be generalised to higher generations $(i+j)$. This results in the following equation,

$$\sum_{k=1}^{j-1}\left[\sum_{l=1}^{j-k-1}\lambda^{-2(i+l)}+2\sum_{l=j-k}^{j}\lambda^{-2(i+l)}\right] \cdot (2P\Gamma(1-P))^k\left(2P^2\Gamma(1-\Gamma)\right)^{j-k-1}P^2\Gamma^2\,. \tag{C.14}$$

Carrying out the innermost sums and simplifying the result gives the following,

$$\frac{P^2\Gamma^2}{\lambda^2-1}\sum_{k=1}^{j-1}\left[\lambda^{-2i}-2\lambda^{-2(i+j)}+\lambda^{-2(i+j-k-1)}\right] \cdot (2P\Gamma(1-P))^k\left(2P^2\Gamma(1-\Gamma)\right)^{j-k-1}\,. \tag{C.15}$$

Once again continuing this *ad infinitum* and summing generations j results in the following expression

$$\frac{P^2\Gamma^2}{\lambda^2-1}\sum_{j=1}^{\infty}\sum_{k=1}^{j-1}\left[\lambda^{-2i}-2\lambda^{-2(i+j)}+\lambda^{-2(i+j-k-1)}\right] \cdot (2P\Gamma(1-P))^k\left(2P^2\Gamma(1-\Gamma)\right)^{j-k-1}\,, \tag{C.16}$$

which, after multiplication with $P^2(1-\Gamma)^2(1-P)$ gives the average saturated void volume that results from wall–wall combinations. Finally, adding equation (C.10), the void volume from the first two generations, i.e., $2P^3(1-P)\Gamma\lambda^{-2}$ and equation (C.16), the final equation for the void volume with $\lambda = 2$ is

$$\begin{aligned} V_v(P,\Gamma) = \frac{P^4\Gamma^2(1-\Gamma)^2(1-P)}{3}\sum_{i=2}^{\infty}\sum_{j=1}^{\infty}\sum_{k=1}^{j-1}\Big\{2^{-2(i+j)}\left(4^j+4^{k+1}-2\right) \\ \cdot\left[2P\Gamma(1-P)\right]^k\left[2P^2\Gamma(1-\Gamma)\right]^{j-k-1}\Big\}+\frac{P^3\Gamma(1-P)}{2} \\ +2P(1-\Gamma)(1-P)\sum_{i=2}^{\infty}\sum_{j=1}^{\infty}\sum_{k=1}^{j-1}2^{-2(i+k)}\left(P^2\Gamma(1-\Gamma)\right)^j\,, \end{aligned} \tag{C.17}$$

where we have summed the two contributions originating from equations (C.10) and (C.16) over all generations $i \geq 2$. Expanding the sums and simplifying, the

void volume can finally be determined to be

$$V_v(P,\Gamma) = \frac{P^5\Gamma^3(1-P)^2(1-\Gamma)^2\left(5-2P\Gamma+2P^3\Gamma^2(1-\Gamma)\right)}{3(2-P\Gamma(1-P))(1-2P\Gamma(1-P))(2-P^2\Gamma(1-\Gamma))(1-2P^2\Gamma(1-\Gamma))}$$
$$- \frac{P^5\Gamma^3(1-P)^2(1-\Gamma)^2\left(2P^4\Gamma^2(1-\Gamma)+2P^2\Gamma(2-3\Gamma)\right)}{3(2-P\Gamma(1-P))(1-2P\Gamma(1-P))(2-P^2\Gamma(1-\Gamma))(1-2P^2\Gamma(1-\Gamma))}$$
$$+ \frac{P^3\Gamma(1-P)(1-\Gamma)^2}{6(1-P^2\Gamma(1-\Gamma))(4-P^2\Gamma(1-\Gamma))} + \frac{P^3\Gamma(1-P)}{2}\,. \tag{C.18}$$

Bibliography

[1] D. E. Panayotounakos and T. I. Zarmpoutis, Int. J. Math. Math. Sci. **2011**, 387429 (2011).

[2] S. F. Edwards and D. R. Wilkinson, Proc. R. Soc. A **381**, 17 (1982).

[3] M. Kardar, G. Parisi, and Y.-C. Zhang, Phys. Rev. Lett. **56**, 889 (1986).

[4] J. Krug and P. Meakin, Phys. Rev. A **43**, 900 (1991).

[5] D. W. Flaherty, Z. Dohnálek, A. Dohnálková, B. W. Arey, D. E. McCready, N. Ponnusamy, C. B. Mullins, and B. D. Kay, J. Phys. Chem. C. **111**, 4765 (2007).

[6] A. Barranco, A. Borras, A. R. Gonzalez-Elipe, and A. Palmero, Prog. Mater. Sci. **76**, 59 (2016).

[7] J. O. Indekeu and K. K. Müller-Nedebock, J. Phys. A: Math. Theor. **51**, 165201 (2018).

[8] J. O. Indekeu and R. Smets, J. Phys. A: Math. Theor. **50**, 315601 (2017).

[9] J. Berx and J. O. Indekeu, J. Phys. A: Math. Theor. **52**, 38LT01 (2019).

[10] G. Adomian, *Solving Frontier Problems of Physics: The Decomposition Method*, 1st ed. (Springer Netherlands, 1994).

[11] G. Adomian, Math. Comput. Model. **13**, 17 (1990).

[12] G. Adomian, *Nonlinear Stochastic Operator Equations*, 1st ed. (Academic Press, 1986).

[13] G. Adomian and R. Rach, J. Math. Anal. Appl. **91**, 39 (1983).

[14] F. Faà di Bruno, Quarterly Journal of Pure and Applied Mathematics **1**, 359 (1857).

[15] P. Nelson, J. Comput. Appl. Math. **23**, 389 (1988).

[16] C. Rach, Kybernetes **37**, 910 (2008).

[17] T. A. Abassy, Comput. Math. with Appl. **59**, 42 (2010).

[18] J.-H. He, Int. J. Non-Linear Mech. **34**, 699 (1999).

[19] J.-H. He, J. Comput. Appl. Math. **207**, 3 (2007).

[20] T. A. Abassy, M. A. El-Tawil, and H. El Zoheiry, J. Comput. Appl. Math. **207**, 137 (2007).

[21] M. Turkyilmazoglu, Appl. Math. Lett. **24**, 762 (2011).

[22] S. Khuri and A. Sayfy, Appl. Math. Lett. **32**, 28 (2014).

[23] J.-H. He, Comput. Methods Appl. Mech. Eng. **178**, 257 (1999).

[24] W. R. Mann, Proc. Amer. Math. Soc. **4**, 506 (1953).

[25] H. Ahmad, T. A. Khan, P. S. Stanimirović, Y.-M. Chu, and I. Ahmad, Complexity **2020**, 8841718 (2020).

[26] M. Hosseini, S. Mohyud-Din, H. Ghaneai, and M. Usman, Int. J. Nonlinear Sci. Numer. Simul. **11**, 495 (2010).

[27] S. Ishikawa, Proc. Am. Math. Soc. **44**, 147 (1974).

[28] Wolfram Research, Inc., "Mathematica, Version 12.0," (2021), Champaign, IL.

[29] W. Schiesser, *The Numerical Method of Lines: Integration of Partial Differential Equations* (Elsevier Science, 2012).

[30] MathWorks, "Matlab, Version R2020b," (2021), Natick, MA.

[31] R. Garrappa, "Predictor-corrector PECE method for fractional differential equations," (2021), MATLAB Central File Exchange.

[32] K. Diethelm and A. Freed, in *Forschung und Wissenschaftliches Rechnen*, edited by S. Heinzel and T. Plesser (Göttingen, 1999) pp. 57–71.

[33] J. Berx and J. O. Indekeu, J. Phys. A: Math. Theor. **54**, 025702 (2020).

[34] R. Camassa and D. D. Holm, Phys. Rev. Lett. **71**, 1661 (1993).

[35] M. P. Bonkile, A. Awasthi, C. Lakshmi, V. Mukundan, and V. S. Aswin, Pramana **90**, 69 (2018).

[36] K. Maeda and T. Colonius, Wave Motion **75**, 36 (2017).

[37] E. G. Ekomasov, A. M. Gumerov, R. V. Kudryavtsev, S. V. Dmitriev, and V. N. Nazarov, Braz. J. Phys. **48**, 576 (2018).

[38] Z. Gul, A. Ali, and A. Ullah, J. Phys. A: Math. Theor. **52**, 015203 (2018).

[39] I. O. Starodub and Y. Zolotaryuk, Phys. Lett. A **383**, 1419 (2019).

[40] R. Fisher, Ann. Eugen. **7**, 355 (1937).

[41] J.-S. Duan, R. Rach, D. Baleanu, and A. Wazwaz, Comm. Frac. Calc **3**, 73 (2012).

[42] A. Wazwaz and S. Khuri, Appl. Math. Comput. **80**, 287 (1996).

[43] K. Padmavally, J. Math. Mech. **7**, 533 (1958).

[44] J. Keller and W. Olmstead, Q. Appl. Math. **29**, 559 (1972).

[45] J. Berx and J. O. Indekeu, Phys. Rev. Res. (2021).

[46] J. Ramos, Appl. Math. Comput. **215**, 1526 (2009).

[47] J. E. Esekon, Int. J. Pure Appl. Math. **82**, 547 (2013).

[48] E. Platen and M. Schweizer, Math. Financ. **8**, 67 (1998).

[49] R. Frey and P. Patie, "Risk management for derivatives in illiquid markets: A simulation study," in *Advances in Finance and Stochastics* (Springer Berlin Heidelberg, 2002) p. 13.

[50] O. González-Gaxiola, J. R. de Chávez, and J. A. Santiago, Int. J. Appl. Comput. Math. **2**, 453 (2016).

[51] J. L. Vazquez, *The Porous Medium Equation: Mathematical Theory* (Oxford University Press, 2006).

[52] M. Abramowitz and I. A. Stegun, *Handbook of Mathematical Functions with Formulas, Graphs, and Mathematical Tables*, 9th ed. (Dover, New York, 1964).

[53] P. Devillard and H. Spohn, EPL **17**, 113 (1992).

[54] A.-L. Barabási and H. E. Stanley, *Fractal Concepts in Surface Growth* (Cambridge University Press, 1995).

[55] J. Burgers (Elsevier, 1948) pp. 171–199.

[56] A. J. Bray, A. Cavagna, and R. D. M. Travasso, Phys. Rev. E **64**, 012102 (2001).

[57] A. J. Bray, A. Cavagna, and R. D. M. Travasso, Phys. Rev. E **65**, 016104 (2001).

[58] T. H. R. Smith, O. Vasilyev, D. B. Abraham, A. Maciołek, and M. Schmidt, Phys. Rev. Lett. **101**, 067203 (2008).

[59] T. H. R. Smith, O. Vasilyev, D. B. Abraham, A. Maciołek, and M. Schmidt, J. Phys. Condens. Matter **20**, 494237 (2008).

[60] N. V. Antonov, N. M. Gulitskiy, P. I. Kakin, and M. M. Kostenko, Phys. Scr. **95**, 084009 (2020).

[61] J. Berx and J. O. Indekeu, (2021), arXiv:2107.00474 [q-bio.PE] .

[62] V. V. Zozulya, Arch. Appl. Mech. **87**, 1605 (2017).

[63] S. K. Godunov, *Ordinary Differential Equations with Constant Coefficients*, Translations of mathematical monographs, Vol. 169 (American Mathematical Society, 1997).

[64] P. van den Driessche, Infect. Dis. Model. **2**, 288 (2017).

[65] O. Makinde, Appl. Math. Comput. **184**, 842 (2007).

[66] A. R. Ghotbi, A. Barari, M. Omidvar, and G. Domairry, J. Mech. Med. Biol **11**, 149 (2011).

[67] M. Y. Li and J. S. Muldowney, Math. Biosci **125**, 155 (1995).

[68] M. B. Trawicki, Mathematics **5**, 7 (2017).

[69] T. Demaerel and C. Maes, Phys. Rev. E **97**, 032604 (2018).

[70] G. H. Weiss, Physica A **311**, 381 (2002).

[71] W. Alharbi and S. Petrovskii, Mathematics **6**, 59 (2018).

[72] E. E. Holmes, Am. Nat. **142**, 779 (1993).

[73] L. C. Evans, *Partial differential equations*, 2nd ed. (American Mathematical Society, 2010).

[74] J. Berx, E. Bervoets, C. V. Giuraniuc, and J. O. Indekeu, Physica A **574**, 125998 (2021).

[75] B. B. Mandelbrot, *The fractal geometry of nature*, 6th ed. (Freeman, 1982).

[76] J. O. Indekeu and G. Fleerackers, Physica A **261**, 294 (1998).

[77] J. O. Indekeu, G. Fleerackers, A. Posazhennikova, and E. Bervoets, Physica A **285**, 135 (2000).

[78] B. Bowen, C. Strong, and K. Golden, J. Fractal Geom. **5**, 121 (2018).

[79] H. Aminirastabi, H. Xue, V. V. Mitić, G. Lazović, G. Ji, and D. Peng, Mater. Chem. Phys. **239**, 122261 (2020).

[80] J. O. Indekeu and K. Sznajd-Weron, Phys. Rev. E **68**, 061904 (2003).

[81] J. O. Indekeu and C. V. Giuraniuc, Physica A **336**, 14 (2004).

[82] D. Stauffer and A. Aharony, *Introduction To Percolation Theory*, 2nd ed. (Taylor & Francis, 1992).

[83] D. Stauffer, Phys. Rep. **54**, 1 (1979).

[84] S. Najem, A. Krayem, T. Ala-Nissila, and M. Grant, Phys. Rev. E **101**, 050301 (2020).

[85] E. Bervoets, *Fraktale kustlijnen en uitsteeksels in het hiërarchisch depositiemodel*, Master's thesis, KU Leuven (2000).

[86] C. V. Giuraniuc, *Deposition and network models in statistical and condensed matter physics with interdisciplinary applications*, Ph.D. thesis, KU Leuven (2006).

[87] J. Krim and J. O. Indekeu, Phys. Rev. E **48**, 1576 (1993).

[88] J. Yu and J. G. Amar, Phys. Rev. E **65**, 060601 (2002).

[89] A. Aharony and D. Stauffer, Int. J. Mod. Phys. C **13**, 603 (2002).

[90] F. Aarão Reis, Physica A **364**, 190 (2006).

[91] F. L. Forgerini and W. Figueiredo, Phys. Rev. E **79**, 041602 (2009).

[92] M. Perreau, J. Peiro, and S. Berthier, Phys. Rev. E **54**, 4590 (1996).

[93] H. M. and V. D. H. R., *Progress in High-Dimensional Percolation and Random Graphs*, 1st ed., CRM Short Courses (Springer International Publishing, 2017).

[94] K. J. Falconer and G. R. Grimmett, J. Theor. Probab. **5**, 465 (1992).

[95] M. E. Orzechowski, Fractals **05**, 101 (1997).

[96] A. Posazhennikova and J. O. Indekeu, Mod. Phys. Lett. B **14**, 119 (2000).

[97] A. Posazhennikova and J. O. Indekeu, Int. J. Thermophys **22**, 1123 (2001).

[98] K. Banerjee, J. Shamanna, and S. Ray, Phys. Rev. E **90**, 022111 (2014).

[99] B. Mal, S. Ray, and J. Shamanna, Phys. Rev. E **93**, 022121 (2016).

[100] T. Dutta and S. Tarafdar, J. Geophys. Res. Solid Earth **108**, 2062 (2003).

[101] R. Dasgupta, S. Roy, and S. Tarafdar, Physica A **275**, 22 (2000).

[102] T. Rondagh, *Application of the BLUES function method on semiconductor junctions*, Master's thesis, KU Leuven (2019).

[103] Y. Yang, Z. Yan, and D. Mihalache, J. Math. Phys. **56**, 053508 (2015).

[104] Z. Yan, X.-F. Zhang, and W. M. Liu, Phys. Rev. A **84**, 023627 (2011).

[105] T. J. Kippenberg, A. L. Gaeta, M. Lipson, and M. L. Gorodetsky, Science **361** (2018).

[106] X. Ma, O. A. Egorov, and S. Schumacher, Phys. Rev. Lett. **118**, 157401 (2017).

[107] D. Lima, W. van Saarloos, and A. De Wit, Physica D **218**, 158 (2006).

[108] M. V. Berry, New J. Phys. **20**, 053066 (2018).

[109] M. V. Berry, New J. Phys. **21**, 073021 (2019).

[110] A. Posazhennikova and J. O. Indekeu, Physica A **414**, 240 (2014).

[111] S. Kakkar, T. S. Kamal, and A. P. Singh, IETE J. Res. **65**, 104 (2019).

[112] X. Man, Z. Luo, J. Liu, and B. Xia, Mater. Des. **180**, 107911 (2019).

[113] G. Archie, Trans. **146**, 54 (1942).

[114] E. Sharafedini, H. Hamzehpour, S. F. Masoudi, and M. Sahimi, J. Appl. Phys. **118**, 215302 (2015).

[115] Z. Ebrahiminejad, H. Hamzehpour, and S. F. Masoudi, J. Mater. Sci.: Mater. Electron. **31**, 18297 (2020).

[116] J. Kondev, C. L. Henley, and D. G. Salinas, Phys. Rev. E **61**, 104 (2000).

[117] A. Calcabrini, H. Ziar, O. Isabella, and M. Zeman, Nat. Energy **4**, 206 (2019).

[118] U. Alon, M. R. Evans, H. Hinrichsen, and D. Mukamel, Phys. Rev. E **57**, 4997 (1998).

[119] A. Korobeinikov and G. Wake, Appl. Math. Lett. **15**, 955 (2002).

[120] N. V. Thu and J. Berx, (2021), arXiv:2002.01624 [cond-mat.quant-gas] .

[121] S. Put, J. Berx, and C. Vanderzande, J. Stat. Mech.: Theory Exp. **2019**, 123205 (2019).

Publications

J. Berx and J. O. Indekeu, *"The BLUES function method for second-order partial differential equations: application to a nonlinear telegrapher equation"*, (in preparation), (2021)

[61] J. Berx and J. O. Indekeu, *"Epidemic processes with constant vaccination and immunity loss studied with the BLUES function method"*, (under peer-review), (2021)

[45] J. Berx and J. O. Indekeu, *"Analytic approximants for interface growth under shear from the BLUES function method applied to nonlinear partial differential equations"*, Accepted in Phys. Rev. Res. (2021)

[120] N. V. Thu and J. Berx, *"The condensed fraction of a homogeneous dilute Bose gas within the improved Hartree-Fock approximation"*, (under peer-review) (2021)

[74] J. Berx, E. Bervoets, C. V. Giuraniuc and J. O. Indekeu, *"Coastlines and percolation in a model for hierarchical random deposition"*, Physica A **574**, 125998 (2021)

[33] J. Berx and J. O. Indekeu, *"BLUES iteration applied to nonlinear ordinary differential equations for wave propagation and heat transfer"*, J. Phys. A: Math. Theor. **54**, 025702 (2020)

[121] S. Put, J. Berx and C. Vanderzande, *"Non-Gaussian anomalous dynamics in systems of interacting run-and-tumble particles"*, J. Stat. Mech.: Theory Exp. **2019**, 123205 (2019)

[9] J. Berx and J. O. Indekeu, *"Analytic iteration procedure for solitons and traveling wavefronts with sources"*, J. Phys. A: Math. Theor. **52**, 38LT01 (2019)

FACULTY OF SCIENCE
DEPARTMENT OF PHYSICS AND ASTRONOMY
INSTITUTE FOR THEORETICAL PHYSICS
Celestijnenlaan 200D box 2415
B-3001 Leuven
jonas.berx@kuleuven.be
https://fys.kuleuven.be/itf